

*A Study of Segregation in Granular Gravity  
Driven Free Surface Flows.*

Thornton, Anthony

2005

MIMS EPrint: **2007.100**

Manchester Institute for Mathematical Sciences  
School of Mathematics

The University of Manchester

Reports available from: <http://eprints.maths.manchester.ac.uk/>

And by contacting: The MIMS Secretary  
School of Mathematics  
The University of Manchester  
Manchester, M13 9PL, UK

ISSN 1749-9097

A STUDY OF SEGREGATION IN  
GRANULAR GRAVITY DRIVEN FREE  
SURFACE FLOWS

A THESIS SUBMITTED TO THE UNIVERSITY OF MANCHESTER  
FOR THE DEGREE OF DOCTOR OF PHILOSOPHY  
IN THE FACULTY OF ENGINEERING AND PHYSICAL SCIENCES

2005

**Anthony Richard Thornton**  
School of Mathematics

# Contents

<b>Abstract</b>	<b>20</b>
<b>Declaration</b>	<b>21</b>
<b>Copyright</b>	<b>22</b>
<b>Acknowledgements</b>	<b>23</b>
<b>Dedication</b>	<b>24</b>
<b>1 Introduction</b>	<b>25</b>
1.1 Particle size segregation mechanisms . . . . .	25
1.2 Avalanche models . . . . .	31
1.2.1 Vertical structure of avalanche models . . . . .	32
1.3 Summary of the Savage-Lun Theory . . . . .	36
1.3.1 Statistical mechanical description of the random fluctuating sieve	37
1.3.2 Continuum quantities . . . . .	38
1.3.3 Solution of the Savage-Lun equations . . . . .	40
1.3.4 Laboratory experiments . . . . .	41
1.4 Aim of the thesis . . . . .	43
1.5 Mixture theory . . . . .	45
1.5.1 Slow flow of a viscous fluid flow through a porous matrix . . . .	48
<b>2 Two Phase Granular Model</b>	<b>51</b>
2.1 Mixture framework and conservation laws . . . . .	51

2.2	The particle size segregation model . . . . .	53
2.2.1	Determining the drag law . . . . .	55
2.2.2	Individual constituent velocities . . . . .	56
2.2.3	The load sharing factors . . . . .	57
2.2.4	The segregation equation . . . . .	58
2.3	Comparison with the Savage & Lun theory . . . . .	59
2.4	Non-dimensional segregation equation . . . . .	61
<b>3</b>	<b>Analytical solutions</b>	<b>63</b>
3.1	Steady-state segregation in steady uniform flows with homogeneous inflow conditions . . . . .	63
3.1.1	Characteristics . . . . .	64
3.1.2	Segregation jump condition . . . . .	66
3.1.3	Shock solutions in mapped coordinates . . . . .	69
3.1.4	Physical solutions . . . . .	71
3.1.5	Comparison to Savage-Lun . . . . .	73
3.1.6	A velocity field that scales with the thickness to the power 3/2 . . . . .	75
3.1.7	Particle paths . . . . .	76
3.2	Steady-state segregation in steady uniform flow with normally graded inflow conditions . . . . .	78
3.2.1	General solution for arbitrary positive velocity fields . . . . .	78
3.2.2	Physical solutions . . . . .	83
3.2.3	Particle paths . . . . .	87
3.3	Time-dependent segregation in steady uniform plug-flows with homo- geneous inflow conditions . . . . .	89
3.3.1	Segregation in independent columns . . . . .	89
3.3.2	General time-dependent solutions for plug-flow . . . . .	90
3.3.3	Solution for $\varphi = 0.5$ . . . . .	92
3.3.4	Sinusoidally Oscillating Inflow Conditions . . . . .	94
3.3.5	Piece-wise Continuous Solution . . . . .	96

3.4	Time-dependent segregation in steady uniform plug flows from initially normally graded inflow conditions . . . . .	99
3.4.1	Solution $\mathcal{Z} = 0.5$ . . . . .	101
3.4.2	Piece-wise continuous solution . . . . .	103
3.4.3	Solution for $\mathcal{Z} = 0.5 + 0.1 \sin(10t)$ . . . . .	105
<b>4</b>	<b>Numerical solutions</b>	<b>108</b>
4.1	Shock-capturing numerical methods for first order hyperbolic equations	108
4.1.1	Total variation diminishing (TVD) schemes . . . . .	111
4.1.2	The <i>CFL</i> Condition . . . . .	112
4.1.3	The Lax-Friedrichs (LF) Method . . . . .	113
4.1.4	Slope Limiters . . . . .	115
4.1.5	Lax-Wendroff (LW) Method and TVD Limiters . . . . .	115
4.1.6	TVD Lax-Friedrichs (TVDLF) . . . . .	119
4.1.7	Modified TVDLF (MTVDLF) . . . . .	119
4.2	Dimensional splitting . . . . .	120
4.3	Boundary conditions . . . . .	121
4.3.1	Inflow conditions . . . . .	122
4.3.2	Outflow conditions . . . . .	122
4.3.3	Solid boundaries . . . . .	123
4.4	Testing of the numerical method . . . . .	123
4.4.1	Test case 1 : Steady-state homogeneous inflow . . . . .	125
4.4.2	Test case 2 : Time-dependent numerical test . . . . .	127
4.4.3	Test case 3 : Shear and time-dependence . . . . .	129
4.5	Effect of weak shear . . . . .	132
4.6	Shear and normally graded inflow . . . . .	135
4.6.1	A chute initially filled with normally graded material . . . . .	135
4.6.2	A chute initially filled with large particles . . . . .	137
4.7	Strong shear and wave breaking . . . . .	140

<b>5</b>	<b>Breaking zones and recirculation</b>	<b>141</b>
5.1	Analytical solution . . . . .	143
5.2	Particle paths . . . . .	146
5.3	Temporal development . . . . .	149
<b>6</b>	<b>Three Phase Model</b>	<b>152</b>
6.1	Three constituent segregation model . . . . .	152
6.1.1	Mixture framework . . . . .	152
6.1.2	The particle-size segregation model . . . . .	153
6.1.3	The non-dimensional segregation equation . . . . .	158
6.2	Comparison with experiments . . . . .	158
<b>7</b>	<b>Experimental Work</b>	<b>161</b>
7.1	Measuring the Densities of Granular Material . . . . .	161
7.2	Measuring the Particle Size Distribution . . . . .	162
7.3	Segregation in Chute Flows . . . . .	164
7.4	Fingering Instability . . . . .	167
<b>8</b>	<b>Conclusions</b>	<b>169</b>
	<b>Bibliography</b>	<b>172</b>
<b>A</b>	<b>Mohr-Coulomb Avalanche Models</b>	<b>181</b>
A.1	Mohr-Coulomb yield criterion . . . . .	181
A.2	The two dimensional Savage-Hutter theory . . . . .	183
<b>B</b>	<b>Exact Form of the function <math>K_s(\eta)</math></b>	<b>187</b>
B.1	Limit as $\eta \rightarrow 0$ . . . . .	188
<b>C</b>	<b>An analytic solution with shear</b>	<b>189</b>
C.1	Review of the non-time-dependent case . . . . .	189
C.1.1	Top Shock Propagation . . . . .	190
C.1.2	Bottom Shock Propagation . . . . .	190

C.1.3	Full Segregation Point . . . . .	190
C.2	Time Dependent Case . . . . .	191
C.2.1	Deriving the Shock Relation . . . . .	191
C.2.2	Top Boundary . . . . .	192
C.2.3	Bottom Boundary . . . . .	192
C.2.4	Triple Point . . . . .	195
C.2.5	The Final Shock . . . . .	196

# List of Tables

1.1	Values of various physical quantities for packing of equal sized spheres around a void, for the Savage-Lun Theory. Taken from p321 of [72]	44
1.2	Summary of the variables used in full mixture theory in their most general form	46
6.1	Summary of the properties of the different interstitial fluids used in the liquid-particle segregation experiments of [85].	159
7.1	Table showing the measured densities and sizes of the materials used in laboratory experiments	162

# List of Figures

- 1.1 An experimental debris-flow descends the USGS Flume in Oregon, U.S.A. (left) and flows out onto a horizontal runout pad (centre) 82.5m from the release point (Images courtesy of USGS/Cascades Volcano Observatory). The large particles gather at the head of the flow, but encounter greater resistance in the run-out zone and are pushed to the side to form lateral coarse grained levees (dark regions) that channelize the finer grained (light) material in the interior. The same effect can be generated in the laboratory (right) with a 14% mixture of (orange) sand and (white) glass ballotini. The flow becomes unstable and multiple fingers are formed each of which is bounded by a lateral levee. 28
- 1.2 Diagram showing the experimental configuration of the experiments of Savage and Lun. The left panel shows a diagrammatic version of the equipment setup (taken from [72]). The right panel shows a still extracted from an animation of the experiments. In this the large particles are white and the small particles black, the shape segregation is apparent in this image . . . . . 42

- 2.1 A diagram showing the coordinate system  $Oxz$  with the  $x$ -axis pointing down a chute, which is inclined at an angle  $\zeta$  to the horizontal. The  $y$ -axis is into the plane of the paper and the  $z$ -axis is normal to the slope. Particle-size segregation takes place within the avalanche creating inversely-graded layers. In the centre of mass frame the velocity field is such that the material is circulated round, as indicated by the solid line. When shear is present, the large particles have a tendency to move towards the front of the flow and the fines towards the rear. . . . . 54
- 3.1 A plot of the steady-state solution in depth-integrated velocity coordinates  $(x, \psi)$  for an inflow concentration  $\phi_0 = 0.6$  and  $Sr = 1$ . The bulk flow is from left to right. The shocks (straight thick lines) meet at the triple-point (grey circle) and divide the domain into three regions. A homogeneous mixture enters from the left-hand side. The characteristics (straight thin lines) carry this information into the triangular region, as indicated by the arrow. The bottom layer is filled by small particles and have upward sloping characteristics, whilst the top layer is filled with large particles and have downward propagating characteristics, which intersect with one another at the shocks. . . . . 67

3.2	Steady-state solutions for the concentration of small particles $\phi$ are shown as a function of the downslope coordinate $x$ and avalanche depth $z$ . The bulk flow is from left to right and the concentration is shown using a contour scale. A blue shading corresponds to higher concentrations of large particles than small, and red <i>visa versa</i> . Whereas green indicates an equal amount of both by volume fraction. The top 3 sets of panels assume linear velocity profiles corresponding to plug flow ( $\alpha = 1$ ), linear shear with basal slip ( $\alpha = 1/2$ ) and simple shear ( $\alpha = 0$ ), from top to bottom respectively. The bottom two panels correspond to Silbert et al.'s velocity $u = 5(1 - (1 - z)^{3/2})/3$ . The left hand panels are for a homogeneous inflow concentration $\phi_0 = 50\%$ and the righthand panels for 30%. The segregation number $S_r = 1$ , implies that all of the solutions segregate fully at $x = 1$ . . . . .	72
3.3	The shock positions for the Savage & Lun theory (3.29) (dashed line) and the current theory (solid line) (3.27) for homogeneous inflow concentrations of 50% (left panel) and 10% (right panel) in a simple shearing flow with $S_r = 1$ . The distances for complete segregation to occur are comparable for the dilute case, but differ significantly at larger concentrations. . . . .	75
3.4	Graph showing the particle paths for large (blue) and small (red) particles starting from an homogeneous inflow condition. The flow is from left to right and the plots are constructed for $S_r = 1$ . A path is drawn for 11 particles, of each type, whose initial height ranges from 0 to 1 in steps of 0.1. The left panel is for plug flow ( $\alpha = 1$ ) and the right for simple shear ( $\alpha = 0$ ). . . . .	78

- 3.5 The steady-state solution in depth-integrated velocity coordinates  $(x, \psi)$  of the characteristics for the normally graded case. The inflow concentration jump is located at  $(0, \psi_r)$  and the bulk flow is from left to right. The characteristics are shown as straight thin lines and the arrows show their direction of propagation. A rarefaction fan is centred at the discontinuity and a series of characteristics radiate away from it. The front marking the first small particles that propagate downwards is indicated by the downward bold characteristic emanating from the fan. This reaches the base at a distance  $x_b = \psi_r/S_r$  downstream and a curved (bold) shock wave is generated that separates the expansion fan from the pure phase of small particles that gather beneath. A similar situation occurs at the top boundary, where the large particles first reach the surface at  $x_s = (1 - \psi_r)/S_r$  and a curved shock is generated that separates the pure phase of large particles from the expansion fan. At a distance  $x_p$  downstream the two shocks meet and a third parallel shock at height  $1 - \psi_r$  is formed, creating a completely segregated inversely graded layer. . . . . 80
- 3.6 Steady-state solutions for the concentration of small particles  $\phi$  are shown as a function of the downslope coordinate  $x$  and avalanche depth  $z$ . The bulk flow is from left to right and the concentration is shown using a contour scale. A shade of blue corresponds to higher concentrations of large particles than small, and red vice versa. The bulk flow is from left to right and the top 3 sets of panels assume linear velocity profiles corresponding to plug flow ( $\alpha = 1$ ), linear shear with basal slip ( $\alpha = 1/2$ ) and simple shear ( $\alpha = 0$ ), from top to bottom respectively. The bottom two panels correspond to Silbert et al.'s velocity  $u = 5(1 - (1 - z)^{3/2})/3$ . The solution is plotted for  $z_r = 0.5$  (left) and  $z_r = 0.7$  (right) . . . . . 84

3.7	A contour plot of the segregation distance $L_s = S_r x_p$ as a function of the linear velocity profile parameter $\alpha$ and the initial discontinuity height $z_r$ . The dot-dash line shows the points where the maximum value of $L_s = 2$ is attained. . . . .	85
3.8	Graph showing the percentage difference, in segregation length, when using simple shear as an approximation to the Silbert profile against initial separation height $z_r$ . The maximum in the estimation is 2.78 and occurs when $z_r = 0.3$ . . . . .	87
3.9	Graph showing the particle paths for large (blue) and small (red) particles starting from a normally graded inflow condition. The flow is from left to right and the plots are constructed for $S_r = 1$ and $z_r = 0.5$ . A path is drawn for 6 particles, of each type, whose initial height ranges from 0 to 0.5 in steps of 0.1 for large and 0.5 to 1 in steps of 0.1 for small. The left panel is for plug flow ( $\alpha = 1$ ) and the right for simple shear ( $\alpha = 0$ ). . . . .	88
3.10	An exact solution for the time-dependent evolution of the small particle concentration $\phi$ in a steady uniform plug-flow. The bulk flow is from left to right and the concentration is shown using a contour scale. A shade of blue corresponds to higher concentrations of large particles than small, and red vice versa. Whereas green indicates there is an equal amount of both by volume fraction. Initially the chute is filled with a homogeneous mixture of particles with a concentration of 50%. At the inflow a homogeneous mixture of particles, also with concentration 50%, enters the chute and flows downstream. The segregation number is taken as $S_r = 1$ and plug velocity $u_0 = 1$ , which implies that the particles fully segregate at $x = 1$ . The steady-state is attained at $t = 1$ . . . . .	93

- 3.11 An exact solution for the time-dependent evolution of the small particle concentration  $\phi$  in a steady uniform plug-flow. The bulk flow is from left to right and the concentration is shown using a contour scale. A shade of blue correspond to higher concentrations of large particles than small, and red vice versa. Whereas green indicates there is an equal amount of both by volume fraction. Initially the chute is filled with a homogeneous mixture of particles with a concentration of 50%. The inflow concentration varies sinusoidally in time with amplitude 10% about a background concentration of 50%. The segregation number was taken to be  $S_r = 1$  and plug flow velocity, which implies that the particles fully segregate at  $x = 1$ . . . . . 95
- 3.12 An exact solution for the time-dependent evolution of the small particle concentration  $\phi$  in a steady uniform plug-flow. The bulk flow is from left to right and the concentration is shown using a contour scale. A shade of blue corresponds to higher concentrations of large particles than small, and red vice versa. Whereas green indicates there is an equal amount of both by volume fraction. Initially the chute is filled with a homogeneous mixture of particles with a concentration of 25%. The inflow starts at a concentration of 50%, after  $t = 0.5$  this is steps up to 75% . The segregation number is  $S_r = 1$  and plug velocity, is used, which implies that the particles fully segregate at  $x = 1$ . . . . . 97
- 3.13 The exact plug-flow solution for the concentration of small particles  $\phi$  is illustrated at a sequence of time-steps using the same contour scale as in all other figures. Initially the flow is normally graded and normally graded material is fed in at  $x = 0$  and flows downstream from left to right. The solution consists of a time-dependent, spatially uniform part that is separated by a transition line moving downstream at speed  $u_0$  from a steady-state region behind. The parameter  $z_r = 1/2$  for all columns and the segregation number is  $S_r = 1$ . . . . . 102

- 3.14 The exact plug-flow solution for the concentration of small particles  $\phi$  is illustrated at a sequence of time-steps using the same contour scale as in all other figures. Initially the flow is normally graded with  $z_r = 0.25$  and normally graded material is fed in at  $x = 0$ , at a time dependent height given by  $z_r = 0.75$ . The flow is from left to right. The solution consists of a time-dependent, spatially uniform part that is separated by a transition line moving downstream at speed 1 from a boundary controlled solution behind. The parameter  $S_r = 1$  is used. 104
- 3.15 The exact plug-flow solution for the concentration of small particles  $\phi$  is illustrated at a sequence of time-steps using the same contour scale as in all other figures. Initially the flow is normally graded with  $z_r = 0.5$  and normally graded material is fed in at  $x = 0$  at a time dependent height given by  $z_r = 0.5 + 0.1 \sin(10t)$ . The flow is from left to right. The solution consists of a time-dependent spatially uniform part that is separated by a transition line moving downstream at speed 1 from a boundary controlled solution behind. The parameter  $S_r = 1$  is used. . . . . 106
- 4.1 This figure graphically illustrates several limiters. Panel (A) shows the general *TVD* region (grey shaded region) and where the second-order Lax-Wendroff and Beam-Warming lie (dotted lines) on this plot. From here, it is clear that neither method is *TVD* for all possible values of  $\theta$ . The shaded region on panels (B)-(D) highlights the second-order *TVD* region. The black line of panel (B),(C) and (D) show the Minmod, Superbee and Woodward limiters respectively. All three produce second-order *TVD* methods. The Minmod limiter follows the lower boundary of the second-order *TVD* region, the Superbee the top boundary and the Woodward limiter lies somewhere between the two. 118

4.2	Figure showing the percentage error norm $\varpi$ against number of points used in the the computation for test case 1. The test was preformed with 10 different grids using between 100 and 1000 points ranging in steps of 100 and two different Courant number 0.8 and 1.0 . . . . .	126
4.3	Graph showing the numerical error compared to the analytic solution, in using the numerical method. The problem and its analytical solution are described in detail in section 3.3.3. The analytic solution reaches steady-state at $t = 1$ . The measure of the error $\varpi$ is given by (4.65) and the error is shown for three different grids 100 by 100, 500 by 500 and 1000 by 1000. The Superbee limiter was used for all cases. . . . .	128
4.4	Above are plots of the percentage error ( $\varpi$ ) against time. These are for the case of the inflow of homogeneous mixed material with equal volume of each type into a chute initially filled with small particles. The separate plots show the effect of changing the number of grid points, the limiter, the Courant number and the order of application of the split operators, respectively. If not stated on the plot, the runs are on a grid of 300 by 300 cells, with a Courant number of 0.8, the Superbee limiter and changing the order of application of the operators after each step. . . . .	130
4.5	The evolution of the volume fraction of small particles, $\phi$ , as a function of the downslope coordinate, $x$ , and avalanche depth, $z$ . The bulk flow is from left to right and the normal contour scale is used. The chute is initially filled with 50% small particles by volume and the same mixture flows in from the left. This case corresponds to a segregation number $S_r = 1$ and a shearing/translating flow with $\alpha = 0.8$ . . . . .	133

- 4.6 The evolution of the volume fraction of small particles,  $\phi$ , as a function of the downslope coordinate,  $x$ , and avalanche depth,  $z$ . The bulk flow is from left to right and the normal contour scale is used. The chute is initially filled with 50% small particles. At  $x = 0$ , a mixture of particles whose concentration varies sinusoidally in time, with amplitude 10% about a mean background concentration of 50%, enters the chute. This case corresponds to a segregation number  $S_r = 1$  and a shearing/translating flow with  $\alpha = 0.8$ . . . . . 134
- 4.7 The numerical solution for the concentration of small particles,  $\phi$ , is shown using the normal contour scale at a series of time-steps for a chute, which was initially filled with normally graded material separated by the line  $z_r = 1/2$ . A linear velocity profile with basal slip ( $\alpha = 1/2$ ) transports the material downslope from left to right and normally graded material is fed onto the chute at  $x = 0$  to replenish the avalanche. The discontinuity height is  $z_r = 1/2$  and the segregation number is  $S_r = 1$ . . . . . 136
- 4.8 The numerical solution for the concentration of small particles,  $\phi$ , is shown using a contour scale at a series of time-steps for a chute. which was initially filled with large particles. A linear velocity profile with basal slip ( $\alpha = 1/2$ ) transports the material downslope from left to right and normally graded material is fed onto the chute at  $x = 0$  to replenish the avalanche. The discontinuity height is  $z_r = 1/2$  and the segregation number is  $S_r = 1$  . . . . . 138

4.9	The figure shows the time-development of segregation from a chute initially filled with a homogeneous mixture with concentration 0.25. At the inflow boundary, a homogeneous mixture of higher concentration (0.75) is fed into the domain. All plots (except bottom right) are constructed with 1000 by 1000 points. The bottom two panels both show the solution at $t = 4$ , the left panel was constructed with 1000 by 1000 points and the right panel with 300 by 300 points. There is very little difference between the two plots. The normal contour scale has again been used. . . . .	139
5.1	Schematic diagram of analytic solution, showing the four key points which define the solution. Fans are generated from the two points on the centre line, which fill the domain contained by the solid lines. The top/bottom solid dots shows the generation location of the two shocks present in the ‘lens’. . . . .	142
5.2	Steady-state spatial $(\xi, z)$ solutions for the concentration of small particles $\phi$ are shown for a linear (top) and square root (bottom) velocity profiles. In this moving frame of reference the large particles enter from the bottom right and exit through the top right side. Whilst the small particles enter through the top left side and exit through the bottom left side. There are two shocks and two expansion waves which redistribute the particles. . . . .	145

5.3	Figure showing the particle paths of both the large and small particles for the case of linear shear. As before, the blue lines represent paths of the small particles and the red lines are the large particles. The paths are illustrated for five of each type of particle. The small particles are taken to enter at heights $z = 0.5, 0.6, 0.7, 0.8, 0.9$ and $1.0$ , and the large particles enter at heights $z = 0.0, 0.1, 0.2, 0.3, 0.4$ and $0.5$ . This highlights the ‘lens’ structure, shown in the top panel of 5.2 and shows how particles filter past each other in the lens, and exit at the same side they enter. . . . .	147
5.4	Graphs showing the development of the ‘lens solution’ starting from a initially horizontally segregated mixture. $S_r$ was taken to be 1. The plots are drawn in the centre of mass coordinates and the velocity field was taken to be the linear shearing case, i.e. $\hat{u} = 2z - 1$ . The chute was initially taken to contain a horizontally segregated solution with the small particles starting behind the large particles. The code was run using a grid of 300 by 300 points and Courant number of 0.8. This solution is seen to develop to the analytical solution discussed in the previous section. . . . .	150
7.1	Graph showing the measured size distribution for both the coarse glass (blue dots) and the sugar particles (red dots). The sugar particles where found to have a mean of 1.52 mm with a standard deviation of 0.11 mm, where as the glass has a mean of 0.72 mm with a standard deviation of 0.09 mm . . . . .	163

7.2	A series of shots from experiments of a mixture of sugar and course glass down an inclined plane. The chute is made of perspex and it is 5.1 cm wide and 148 cm long with an incline of 26 degrees to the horizontal. The end of the chute was closed and hence a shock wave is generated when the material reaches the bottom. This shock propagates up the chute until reaching the hopper. As the shock passes, the depth of the flow is seen to increase in thickness. The images on the left hand-side show the material flowing before the bottom has been reached and generated a shock wave. The images on the right are for the final deposit once the flow has come to rest. The top panels are for a gate height (initial depth) of 5 cm and the bottom panels 3 cm. The material used is a 50 % by volume fraction of sugar (red) and course glass (white), the properties of this material are summerized in table 7.1. The screws from the base of the chute into the side walls are 18 cm apart. . . . .	165
7.3	Above are a sequence of stills from a video of a mixture of sand and fine glass flowing down a rough incline, whose propeties are summerised in table 7.1. The sand accounts for 14% of the material by volume. The flow is from left to right. The chute is 1.2 metres long and 0.6 metres wide and was roughenend by glueing the sand to its surface. It was inclined at an angle of 30 degrees to the horzizontal. . . . .	167
A.1	Mohr diagram showing Coulomb yield criterion, bed friction angle, and active and passive stress conditions . . . . .	182

# Abstract

Segregation occurs in many natural and industrial free surface flows, and its study and understanding is of fundamental importance in many fields. The thesis formulates a new continuum model for this process in bi-dispersed equal density granular material. Numerous analytical solutions of this model are obtained and are shown to be in good qualitative agreement with existing experimental data. Then an accurate high order Total Variation Diminishing numerical scheme is developed to investigate time dependent flows and more complicated configurations. Additionally, the model is extended to include the effect of a passive non-viscous fluid occupying the pore space between the grains. The results of this extended model are in quantitative agreement with existing experiment data. A brief investigation of experiments to test further the predictions of this model was also undertaken. This included a study of the feed-back that segregation can have on the bulk properties of a flowing granular material, which highlights how this model could be used to investigate the important phenomenon of granular fingering in the future.

# Declaration

No portion of the work referred to in this thesis has been submitted in support of an application for another degree or qualification of this or any other university or other institution of learning.

# Copyright

Copyright in text of this thesis rests with the Author. Copies (by any process) either in full, or of extracts, may be made **only** in accordance with instructions given by the Author and lodged in the John Rylands University Library of Manchester. Details may be obtained from the Librarian. This page must form part of any such copies made. Further copies (by any process) of copies made in accordance with such instructions may not be made without the permission (in writing) of the Author.

The ownership of any intellectual property rights which may be described in this thesis is vested in the University of Manchester, subject to any prior agreement to the contrary, and may not be made available for use by third parties without the written permission of the University, which will prescribe the terms and conditions of any such agreement.

Further information on the conditions under which disclosures and exploitation may take place is available from the Head of the Department of Mathematics.

# Acknowledgements

I would like to thank my supervisor Dr.Nico Gray for his support and help over the three years of this PhD, his advice in many areas has proved to be invaluable. I would like to thank all the people who have given up their time to discuss this topic with me, without which many of the interesting ideas and directions encompassed in this work would never occurred.

I would like to thank Dr.Chris Paul for solving the numerous computing problems and technical queries during my time as a postgraduate at Manchester university.

Finally, I would like to thank Alex Heap and Cathy Kindred for help in proof reading this document, without whom, most of what is written in this thesis would be completely unintelligible.

# Dedication

For my sister Janet (June 4th 1964-21st August 2005).

Who taught me, that you are, only as old as you feel.

# Chapter 1

## Introduction

### 1.1 Particle size segregation mechanisms

Many industrial processes use materials in a granular form, as they are easy to produce and store. The mixing of powders and grains into a homogeneous blend is essential in numerous areas of industry, including coal, stock feed, pharmaceuticals, nuclear fuels, fertilizers, powders metallurgy, detergent and paint production. These fields represent a substantial world-wide financial turnover, sales in powdered metals alone exceed €6 billion in Europe and another \$5 billion in North America<sup>1</sup>. Segregation during transport and processing represents a huge problem in all these fields and remains poorly understood. The importance to industry of producing good mixtures and avoiding segregation is highlighted by the fact there have been over six hundred papers written on the topic in the engineering literature, before the beginning of the 1980's. Cooke, Stephens and Bridgewater [14], gave an overview of this vast amount of material.

One common industrial process is the rotating drum/cylinder. These are used extensively, especially in the food and pharmaceutical industry, to mix grains into a consistent blend (e.g. [61, 74, 36]). Whereas, the rotary kilns (long inclined rotating cylinder) are favoured by chemical engineers for sintering, calcination, humidification, oxidation, drying, mixing, induration, reducing, gas-solid reaction, incineration,

---

<sup>1</sup>based upon information obtained from [1] and referenced link e.g. [www.pmdatabase.com](http://www.pmdatabase.com)

heating, cooling processes, because of their continuous feed. By far the biggest user of these devices is the cement production industry. Cement is the basic ingredient of concrete and it is estimated that 1700 billion tonnes of cement are used every year<sup>2</sup>. This process is energy intensive and according to one estimate consumes 1% of world wide electricity production. The size of the particles entering the kiln has to be carefully controlled and a large percentage of the cost of production is absorbed in milling and sizing<sup>2</sup>, which is done to reduce the effect of size segregation when the material enters the rotary kiln. Experiments (e.g. [92, 44]) have shown an axial instability in these long rotating drums flows, leading to an axial banding, which results in a spatially segregated mixture. It is clear that, in industry, the effect of this unwanted segregation can cause many wide ranging effects, including tablets with too much, or too little, active ingredient, through to less effective washing detergents, [76].

Despite the huge effect size segregation has on common place industrial flows, very little theoretical work exist, and engineers rely on empirical “Do’s and Don’ts” e.g. Johanson [53]. This, and other similar literature, consists of a list of processes and procedures where segregation is likely to take place and recommends mixtures of different size particles are mixed immediately before use or final packaging. This requirement to keep remixing materials after transportation or processing and the heavy use of sampling and testing for quality control is very costly and time consuming.

There are several mechanisms for the segregation of dissimilar grains in granular flows [8], including inter-particle percolation, convection [27], inertia, buoyancy, collisional condensation [50], differential air drag, clustering [64] and ordered settling. This thesis, however, focuses on *kinetic sieving* [72], which is the dominant mechanism for particle-size segregation in dense granular free-surface flows. The basic idea is that, as grains avalanche downslope, the local void ratio fluctuates and the small particles fall into gaps which open up beneath them, as they are more likely to fit into the available space than the large ones. The small particles, therefore, migrate

---

<sup>2</sup>Information obtained from Malvern Process Systems prospective or alternatively their website located at [www.malps/ProcessEng/industries/cement/overview.htm](http://www.malps/ProcessEng/industries/cement/overview.htm)

towards the bottom of the flow and lever the large particles upwards due to force imbalances. In frictional flows this process is so efficient that segregated layers rapidly develop, with a region of 100% large particles separated by a concentration jump from a layer of 100% fines below, [72, 85]. In geology, this is known as *inverse* or *reverse* grading, [62], and distinguishes deposits from granular flows, such as rockfalls, lahars, debris-flows and pyroclastic flows, [83, 47], from *normally* graded deposits formed by settling in rivers and lakes, here, the Stokes drag implies the fines lie on top of the coarser particles. In more energetic flows, diffusive mixing competes with kinetic sieving to produce a smoothly varying inversely graded layer, [52]. Density differences between particles complicate the picture still further by introducing buoyancy effects. Although this is weaker than kinetic sieving, it is still strong enough to prevent particle-size segregation altogether, [23], if the large particles are sufficiently dense and promotes size-segregation when the small particles are denser.

The effect of size segregation is also often seen in the geological scale flows. These include the creation of lobate deposits, [11, 47], from pyroclastic flows and submarine landslides caused by volcano flank collapses, where “megablocks” of up to 1km in size have been observed in the lateral levees, [89]. It has long been acknowledged, in this community, that when granular material flows, an inverse grading of size is created in the avalanching material. These flows are often highly sheared due to the rough topography upon which they take place. When this inversely graded layer is sheared, large particles tend to migrate towards the front of the flow and smaller ones towards the rear. This has a striking effect on the bulk dynamics when the large particles are less mobile than the small ones. In debris-flows, particle size segregation causes the coarse particles to gather at the front, where the pore fluid pressure drops, the mobility of the flow decreases and a surge front develops, which is driven along by the high mobility, high pore pressure, fine grained material behind. Secondary surges are also observed to form spontaneously within the flow itself. As the debris-flow flows into the run-out zone the effect of size segregation becomes even more pronounced. The coarse grains come to rest and are bulldozed to the sides, to form stationary *lateral levees* that channelize the more mobile fine grain material



Figure 1.1: An experimental debris-flow descends the USGS Flume in Oregon, U.S.A. (left) and flows out onto a horizontal runout pad (centre) 82.5m from the release point (Images courtesy of USGS/Cascades Volcano Observatory). The large particles gather at the head of the flow, but encounter greater resistance in the run-out zone and are pushed to the side to form lateral coarse grained levees (dark regions) that channelize the finer grained (light) material in the interior. The same effect can be generated in the laboratory (right) with a 14% mixture of (orange) sand and (white) glass balotini. The flow becomes unstable and multiple fingers are formed each of which is bounded by a lateral levee.

and lead to significantly longer run-out distances than if it were unconfined. There is a large amount of field and large-flume experimental data of this process. The left panels of figure 1.1 shows one such experiment performed by USGS, in which they have a 60 metre long chute where they can carefully control the setup and initiation conditions. The middle panel shows a top view of the run-out zone, here segregation can clearly be seen and the fine material is channelized by large material building up at the side of the flow. This process is what leads to greatly increased flow distances than predicted by avalanche models that take no account of the segregation process. For sometime now, the particle-size segregation process and its subtle feedback onto the bulk flow, has been the single biggest stumbling block in accurately predicting the path and run-out distance of hazardous granular and granular-fluid flows in the natural environment, [45].

Rock avalanches and landslides can often have a deadly effect. For example, on

the 29th of April 1903, Turtle Mountain collapsed and created the largest landslide ever recorded in North America. Its path took it through the town of Frank, Alberta and destroyed 2/3 of the houses and claimed 76 lives. This flow contained a large number of massive limestone boulders, which bulldozed their way through most of the objects in their path. There is also increasing evidence that it is pyroclastic flows, not the air-fall pumice, that create most of the devastation in volcanic eruptions. These consist of a high speed avalanche of hot pumice and ash. Their direction is heavily influenced by the topography over which they are travelling, and size-segregation effects are also likely to play a role. Possibly the most famous pyroclastic flow is that of AD79 when Mount Vesuvius erupted, the resulting flow reached three Roman towns (Herculaneum, Oplontis and Pompeii) and the deposit created can be found up-to 10km from the source, [75]. A lot of geological disasters create avalanches with a variation in size of material, many of which consist of a large amount of small particles with the odd large boulders embedded. Therefore, trying to understand the segregation process, and eventually the feed-back this has on the bulk, is of vital importance in many areas of hazard protection.

Similar effects can be observed in dry granular flows in the laboratory [67, 68] by pouring a mixture of large rough sand particles and small glass ballotini down a slope. In these experiment a uniform flow front is seen to break down into a multiple finger state, two examples of which are shown in the right panel of figure 1.1. The white material is very smooth fine glass ballotini whereas the darker orange material is large rougher sand. On close inspection, these individual fingers look strikingly similar to the structure found in the large scale confined flows of USGS (middle panel). These experiments are discussed in more detail in §7.4. In [68] Pouliquen and Vallance proposed how the feed-back from the segregation process to the avalanche could be added. They allowed the coefficient of friction to be a function of the volume fraction of the small particles at any given point. They went on to show, using a shooting code, that the front is linearly stable for a homogeneous mixture but unstable if the rough material is forward of the smooth material. As they had no model of the segregation process, it was not possible to model the whole break-down from a uniform front.

Particle-size segregation can manifest itself in observed deposits in others ways. Often geologists encounter stratified reverse graded deposits, [62, 28, 11]. These are produced by a sequence of avalanches, each of which is brought to rest *en masse* by the upslope propagation of a shock wave. As the shock passes, the avalanche rapidly thickens and the inversely graded layers expand and are frozen into the deposit to create a two-layer reverse-graded *stripe*. This is then buried and the process is repeated to create the stratified deposit. This same process leads to patterns in rotating drums, in this situation the material is frozen into the solid body rotating region underneath an avalanching layer. These stripes are then periodically destroyed, on returning to the free surface, and reformed by the free flowing layer. The theory of Gray [36] gives a method of determining the interface between these fluid/solid-like regions, though, no model to describe the full process giving a complete treatment of the segregation exists.

It is clear that dense granular flows, where the phenomena of size segregation plays an important role, are common and occur across wide ranging length scales varying from table top to geophysical. The only existing theory to-date for this flow regime was derived by Savage & Lun [72] in 1988. They used statistical mechanics and information entropy ideas to derive a theory, which was able to predict the steady-state particle-size distribution in a steady uniform flow. This theory is looked at in more detail in §1.3. Jenkins & Yoon [50, 52] investigated one-dimensional steady-state segregation in energetic collisional flows. This theory is derived from the kinetic theory of granular material. The kinetic theory has been developed over the last twenty years starting with the original paper of Jenkins and Savage, [51], in 1983. One of the key assumptions of this theory is that particles only interact through binary collisions. Any segregation theory derived from this leads to a gradual transition between states of pure type. This matches experimental results for very high energy flows, but for slightly slower flows sharp transitions between pure regions are experimentally observed. In this thesis, attention is restricted to this intermediate region where there is flow, but enduring contacts between neighbouring particles still exist. This is often referred to as the granular fluid-state and most avalanche flows

take place in this velocity range. Dolgunin & Ukolov [21] have recently used a physical argument to arrive at a segregation model for these high energy flows which has the same structure of the Savage & Lun with an additional diffusion type term. Due to the physical nature of these arguments, the resulting model has a lot of free parameters that are fitted from experimental data.

## 1.2 Avalanche models

The purpose of this thesis is to develop a model of segregation in dense-granular free surface flows or avalanches. Therefore, some time will be taken to look at existing avalanche models. These fall into two main types; shallow water theories developed by Eglit, Grigorian & Kulikovskii ([41, 55, 26, 38]) and Mohr-Coulomb model developed by Savage & Hutter and later extended by numerous people including Gray, Denlinger and Iverson ([70, 71, 40, 19, 18]). These extensions include adding the effect of a viscous pore fluid and generalising to complicated, rapidly changing topography. This has allowed the construction of numerical algorithms that can cope with real-life geological flows for the first time.

The Savage-Hutter model is derived from general mass and momentum conservation laws. Coulomb's sliding friction law is applied at the base of the flow and the model is closed by assuming that the material is always in the a stress-state consistent with the Mohr-Coulomb yield criterion. The equations are integrated across the vertical direction,  $z$  dependence can be included by the addition of shape factors, discussed later. The resulting governing equations in Cartesian two-dimensional coordinates are

$$\frac{\partial h}{\partial t} + \frac{\partial}{\partial x} (hu) = d, \quad (1.1a)$$

$$\frac{\partial}{\partial t} (hu) + \frac{\partial}{\partial x} (\alpha_1 hu^2) + \frac{\partial}{\partial x} \left( k_x gh^2 \cos \xi \frac{h^2}{2} \right) = hgD, \quad (1.1b)$$

where  $d$  is the rate of deposition,  $\xi$  is the local angle of inclination of the slope, and  $h = h(x, t)$  is the local depth of the flow, measured in the direction opposed to gravity.

The driving force,  $D$ , applied to the avalanche is given by

$$D = \cos \xi (\tan \xi - \tan \delta), \quad (1.2)$$

where  $\delta$  is the angle of friction and Earth-pressure coefficient,  $k_x$ , arises from the Mohr-Coulomb closure model. The exact form of this and a derivation of the two-dimensional Savage Hutter avalanche model is considered in detail in appendix A. The shape factor,  $\alpha_1$ , arises from the depth integration and is often taken to be unity. A more detailed consideration of the possible values for the shape factors is discussed at the end of this chapter.

Anyone who is familiar with the theory of shallow water waves, for example, see [77], will observe similarity with (1.1). Considerably earlier in the Russian literature, [41], the same equation can be found, but with the identification that  $k_x = 1$  by assuming that a granular avalanche acts like an inviscid swallow fluid with a Coulomb basal sliding friction law. It still remains an open question within the field of which form of the Earth-Pressure coefficient should be taken.

Both sets of models assume that the granular avalanche is incompressible and the bulk material has a constant density, so

$$\nabla \cdot \mathbf{u} = 0 \quad (1.3)$$

must hold.

### 1.2.1 Vertical structure of avalanche models

The Savage-Hutter model is obtained by depth integrating the equations in the direction defined by gravity, see Appendix A for details. During this process, a vertical velocity structure needs to be assumed. In this section a model for this vertical structure for avalanching flows is considered.

One of the first sets of experiments to obtain the velocity field of a granular flow was performed by Vallance, [84]. These were carried out on a bumpy chute 1.2m long and 7.5cm wide, and the surface was roughened by sticking the material under investigation to its surface. Experiments were carried out with three different sizes

of glass spheres, polystyrene spheres and Ottawa sand and for a variety of chute inclination angles from 18.5 to 35 degrees. The method of horizontal trapping was used to determine the velocity structure. This process is quite intrusive and leads to the conclusion that vertical velocity profile is “approximately linear”. Further experiments and analysis suggested that the mean velocity scales with the depth of the flow to the power 3/2. The results also suggested that the bulk solids density across the chute is constant.

Later Pouliquen, [66], performed more detailed experiments on the mean flow velocity using a rough chute 200cm long and 70cm wide. He used a front tracking method and image processing to determine how far the front moved between each frame. In this case, four different systems were used with varying surface roughness and glass bead sizes. The full phase space of different angles and flow depth was investigated. This space could be divided into three regions where either no flow takes place, no steady flow was observed or steady uniform flows were achieved.

For the region of phase space where steady uniform flow was obtained, all the experimental data was found to collapse on to one curve if the Froude number was plotted against the ratio of the flow depth,  $h$ , to the depth of the remaining material after a flow had come to rest,  $h_{stop}$ , i.e.

$$\frac{\bar{u}}{\sqrt{gh}} = \beta \frac{h}{h_{stop}}. \quad (1.4)$$

The constant of proportionality  $\beta$  was found to be 0.136 and is independent of all flow properties.  $h_{stop}$  is a strong function of both the angle of inclination of the chute and the basal of roughness and seems to be all that is required to understand all properties of a chute flow. Equation (1.4) immediately reveals the same mean flow to the power 3/2 of flow depth law, which was first suggested by Vallance, [84]. This shows that this scaling to 3/2 can be produced in chute flows of substantially different aspect ratios.

Recently (2001) Silbert *et al.* [56] have used the constitutive law first proposed by Bagnold, in 1954 ([4]), to obtain a velocity profile for granular material in a chute flow. Bagnold [4] proposed that the shear stress  $\sigma_{xz}$  is proportional to the strain rate

$\dot{\gamma}$ , hence

$$\sigma_{xz} = A_{bag}^2 \dot{\gamma}^2, \quad (1.5)$$

where  $A_{bag}$  is a constant of proportionality,  $\sigma$  is the stress-tensor and the rate of strain is given by

$$\dot{\gamma} = \frac{\partial u(z)}{\partial z}. \quad (1.6)$$

Silbert *et al.* started from the two dimensional steady-state Cauchy equation, which states

$$\frac{\partial \sigma_{zz}}{\partial z} = \rho g \cos \theta, \quad (1.7a)$$

$$\frac{\partial \sigma_{xz}}{\partial z} = \rho g \sin \theta, \quad (1.7b)$$

where  $\theta$  is the angle of inclination of the chute. On the assumption that the granular material has a constant density throughout its depth, (1.7b) is easily integrated to give

$$\sigma_{xz} = \rho g \sin \theta (h - z). \quad (1.8)$$

It was also assumed the material is stress-free at a free surface located at  $z = h$ . Substituting this result into (1.5) reveals the result,

$$\frac{\partial u(z)}{\partial z} = \frac{1}{A_{bag}} \sqrt{\rho g \sin \theta (h - z)}. \quad (1.9)$$

Integrating (1.9) across the avalanche depth and applying a non-slip condition at  $z = 0$  gives the following velocity profile

$$u(z) = \frac{h^{3/2}}{A_{bag}} \left( \frac{2}{3} \sqrt{\rho g \sin \theta} \right) \left[ 1 - \left( \frac{h - z}{h} \right)^{3/2} \right]. \quad (1.10)$$

The mean velocity is clearly given by

$$\bar{u} = \frac{1}{h} \int_0^h u(z) dz. \quad (1.11)$$

Substituting (1.10) into (1.11) and after evaluation of the integral the implied mean velocity from this analysis is

$$\bar{u} = \frac{2}{5} \frac{h^{3/2}}{A_{bag}} \sqrt{\rho g \sin \theta}. \quad (1.12)$$

Immediately it is clear that this has the relationship of mean velocity proportional to flow depth to the power  $3/2$  shown in both the experiments of Vallance [84] and Pouliquen, [66]. Silbert *et al.* also performed three/two dimensional molecular dynamics simulations in two/one dimensional chutes. The chute was chosen to be periodic in the cross flow direction. Layers of around thirty particles deep were studied, which is considerably deeper than the layers obtained in the experimental studies, where 10-15 particles was more the norm. The flow was initiated by tilting the chute to a large angle and slowly reducing this until the flow obtained a steady state. Steady state was taken to be the point where the energy input from gravity was exactly balanced by the energy removed from the system by dissipation due to friction and collisions. They again constructed the full phase space where no flow was observed, no steady-state was observed and steady flow was obtained. These are comparable to the experimental diagrams constructed by Pouliquen [66]. The results for 3D and 2D are not identical and in the 3D simulations hysteric effects were observed in results near the domain boundaries. Also the location of these flow domains were found to be dependent on the coefficient of restitution and friction, of the particles. These simulations also showed that this derived velocity profile (1.10) holds for systems which are more than twenty particles deep. For these thinner layers a linear velocity profile seems to be more appropriate.

The velocity profile in (1.10) seems incompatible with the observations of Vallance [84], as Vallance found a linear profile with depth, but closer inspection of Vallance's experimental data show that for most were conducted with flow depths under the twenty particle diameters depth found to be required by the numerics. In addition, a small change in the gradient of the velocity profile, especially in the deeper flows, can be observed. It would be very hard to distinguish between a linear profile and  $z^{3/2}$  using this technique, as in most experiments the velocity was only measured at approximately ten different locations across the depth.

The shape factor that appear in the 2D Savage Hutter equations is given by

$$\alpha_1 = \frac{h \int_0^h u^2 dz}{\left( \int_0^h u dz \right)^2}. \quad (1.13)$$

This will be evaluated for the Silbert profile, first the mean square velocity needs to be computed. This is given by

$$\bar{u}^2 = \frac{1}{h} \int_0^h u^2 dz = \frac{1}{5} \frac{h^3}{A_{bag}^2} \rho g \sin \theta \quad (1.14)$$

Using results (1.14) and (1.12) with the definition (1.13) gives,

$$\alpha_1 = \frac{5}{4} \quad (1.15)$$

Note, that Louge [58] has extended Silbert *et al.*'s [56] theory to determine the constant of proportionality,  $A_{bag}$ .

### 1.3 Summary of the Savage-Lun Theory

Savage and Lun [72] proposed a model for kinetic sieving in dense dry cohesion-less granular flows. In this chapter an outline of their derivation is given and their main conclusions are summarised. This is not designed to be a comprehensive derivation of the model they present, but to explain the physical basis and structure that their argument takes. They consider a simplified problem involving steady two-dimensional flow of a binary mixture of particles of equal density. The flow is assumed to consist of a series of layers aligned parallel to the base of the flow, which is taken to be impermeable. Each of these layers is sheared relative to their neighbours with a constant mean rate, generated by a rough chute base. The flow is assumed to be sufficiently slow, such that, contacts between particles are long, i.e. the collisions are not binary. If the flow is too energetic, collisions will lead to diffusive remixing and in this limit the model of Jenkins & Yoon [52] is applicable.

Savage & Lun propose two mechanisms for the transfer of particles between these layers, the first of which was termed the “random fluctuating sieve”. At any instant in time, there will be a random distribution of void spaces within each layer. Due to the relative motion of layers, particles will be presented with voids beneath them. If the void is large enough the particle will fall into this hole and since the size of these spaces is randomly distributed the probability of a small particle filling a void

is greater than that of a large particle. Hence, with this mechanism small particles preferentially move towards the base of the flow.

The second mechanism is due to force imbalances on individual particles, this can ‘push’ a particle into an adjacent layer. This process was termed “squeeze expulsion” and is assumed to be size independent. It is then required that the flux due to this process is such that there is zero net total mass flux, when both mechanisms are considered.

### 1.3.1 Statistical mechanical description of the random fluctuating sieve

The first step in determining the fall velocity due to this mechanism is to determine the probability distribution of the voids within each layer. This is done using the ‘maximum-entropy approach’, e.g. [49, 10]. From this argument it can be shown that, if all void sizes are equally probable then the probability of finding a given void diameter ratio ( $E$ ) is

$$p(E) = \frac{1}{\bar{E} - E_m} \exp\left(-\frac{E - E_m}{\bar{E} - E_m}\right), \quad (1.16)$$

where  $E_m$  is the minimum possible and  $\bar{E}$  is the mean void diameter ratio.  $E$  is a dimensionless measure of the size of a void and is defined as the ratio of the diameter of a void to the mean *local* particle diameter. The result will be familiar to anybody with knowledge of the Maxwell-Boltzmann distribution for the probability of finding a particle at a given energy  $T$  (for example see [60]). The only difference is the fact that the distribution is shifted such that the minimum value is  $E_m$  not 0 and the mean value is  $\bar{E}$  not  $kT$ .

The number of small particles captured per unit area per unit time by a void having diameters in the range  $D_V \rightarrow D_V + dD_V$  is given by the flux of small particles relative to the layer below multiplied by the probability of a void, of that size, multiplied by the capture width of a void, of that size, i.e.

$$n_v \frac{n_s}{n_l + n_s} u_r D_c n_p p dE, \quad (1.17)$$

where  $n_l/n_s$  is the number of large/small particles the local vicinity,  $n_v/n_p$  is the number of voids/particles per unit area in a layer. It should be emphasised that  $n_p \neq n_s + n_l$ , as  $n_s$  and  $n_l$  are not per unit area,  $u_r$  is the relative velocity between the two layers, this is clearly just the product of the shear rate and the mean distance between adjacent layers,  $D_c$  is the capture width of void of size  $D_v$ . The latter is the distance over which a particle will feel the effect and the void and fall toward the void. This is approximately given by the loci of points where the centre of mass of the particle overlaps with the void, hence, it is taken that  $D_c = D_v + \bar{D}$ .

To obtain the number of small/large particles which fall due to this mechanism per unit time, equation (1.17) is integrated from the size of the particle to infinity. This produces the following results

$$N_s = n_v \frac{n_s}{n_l + n_s} u_r \bar{D} n_p [E_s - \bar{E} - E_m + 1] \exp \left\{ -\frac{E_s - E_m}{E - E_m} \right\} \quad (1.18a)$$

and

$$N_l = n_v \frac{n_s}{n_l + n_s} u_r \bar{D} n_p [E_l - \bar{E} - E_m + 1] \exp \left\{ -\frac{E_l - E_m}{E - E_m} \right\} \quad (1.18b)$$

where  $E_\nu = D_\nu/\bar{D}$  is the dimensionless diameter of the small/large particles respectively, for  $\nu = s, l$ . From this point onwards the convention that the subscript  $\nu$  will mean a quantity associated with small/large particles.

### 1.3.2 Continuum quantities

So far, a statistical approach has been used to determine the number of particles per unit time per unit volume which are captured by voids in the layer below. To produce a continuum model for the complete procedure of kinetic sieving the statistical results (1.18) are averaged to produce percolation velocities for each constituent,  $q_\nu$ . This average percolation velocity is defined as

$$q_\nu = -\frac{m_\nu N_\nu}{\rho_\nu}, \quad (1.19)$$

where  $m_\nu$  is the mass of an individual large/small particle and  $\rho_\nu$  is the density of a constituent per unit *total* volume. The minus sign signifies that the flux due to this “fluctuating sieve” is towards the base of the flow.

This mechanism only gives flow in the downwards direction, this has to be balance by the second “squeeze expulsion” process, thus the flux for this second process ( $q_{se}$ ) is defined such that the total mass flux is zero. Hence,

$$\rho_s q_s + \rho_l q_l + \rho q_{se} = 0, \quad (1.20)$$

where  $\rho$  is the bulk solid density (i.e. the intrinsic particle density). The intrinsic densities of small/large particles is given by

$$\rho_s = \frac{\rho \eta \sigma^3}{(1+e)(1+\eta \sigma^3)}, \quad (1.21a)$$

$$\rho_l = \frac{\rho}{(1+e)(1+\eta \sigma^3)}, \quad (1.21b)$$

respectively; where  $\eta = n_s/n_l$  is the number density ratio,  $\sigma = D_s/D_l$  is the ratio of the diameter of small to large particles and  $e$  is the volume voids ratio i.e. the volume of voids/volume of solids. Alternatively, the mass conservation equation (1.20) could have been written in the following form

$$\rho_l q_{N_l} + \rho_s q_{N_s} = 0, \quad (1.22)$$

where the  $q_N$ 's represent the net percolation flux of each constituent. It is assumed that this “squeeze expulsion” flux is the same for both particles, hence,

$$q_{N_s} = q_s + q_{se} \quad \text{and} \quad q_{N_l} = q_l + q_{se}. \quad (1.23)$$

It is convenient to write these net mass fluxes in terms of the statistical “fluctuating sieve” drop frequencies, determined in §1.3.1. Using (1.19), (1.20) and (1.23), the following results are obtained

$$\rho_l q_{N_l} = -\frac{\rho_s}{\rho} m_l N_l + \frac{\rho_l}{\rho} m_s N_s, \quad (1.24a)$$

$$\rho_s q_{N_s} = +\frac{\rho_s}{\rho} m_l N_l - \frac{\rho_l}{\rho} m_s N_s. \quad (1.24b)$$

Using the definitions of the densities, (1.21), this can be expressed in terms of percolation fluxes as

$$q_{N_l} = \frac{1}{1+\eta \sigma^3} (q_l - q_s), \quad (1.25a)$$

$$q_{N_s} = -\frac{\eta\sigma^3}{1 + \eta\sigma^3} (q_l - q_s). \quad (1.25b)$$

This second form will be found to be more convenient, in §2.3, when comparing this model to the new model proposed in §2.

So far, conservation of mass has only been considered in the normal to chute direction for steady uniform flow global mass conservation implies that,

$$\nabla \cdot (\rho_\nu v_\nu) = 0 \quad \nu = (s, l), \quad (1.26)$$

where  $v_\nu$  is the velocity of the constituent. Imposing that the downslope velocity is simple shear with a rate  $\gamma$ , these equations are reduced to

$$\gamma z \frac{\partial \rho_\nu}{\partial x} + \frac{\partial}{\partial z} [\rho_\nu q_{N_\nu}] = 0 \quad \nu = (s, l). \quad (1.27)$$

### 1.3.3 Solution of the Savage-Lun equations

These equations are coupled through the definition of the net percolation (1.24). This set of coupled equations is solved using the method of characteristics, which gives a family of characteristic curves on which the number ratio,  $\eta$ , is constant

$$z = [z_0^2 - 2D_l K_s x]^{\frac{1}{2}}, \quad (1.28)$$

where  $z_0$  is a constant corresponding to  $z$ -value of the characteristic line at the initial station  $x = 0$  and  $K_s$ , in general, is a complicated function of  $\eta$ . The method of characteristics will be discussed in more detail in §3.1.1, when it is used to solve the new model. In appendix B, the full form of this and the small  $\eta$  limit is discussed.

This characteristic solution leads to the small particles having a percolation rate toward the base of the flow given by  $K_s$ , which in the limit of  $\eta \rightarrow 0$  is a constant (see appendix B), this clearly has to break down at the base of flow as the bed is impermeable. At this point the fines accumulate and a region of 100% concentration is produced. Then, a shock condition should be applied, but they continued incorrectly, instead they assumed that the fall line (or shock) marking the 0% fines region, was given by the characteristic curve emanating from the top of the inflow boundary. The equation of the curve given by setting  $z_0 = h$  in (1.28), is

$$z_2 = (h^2 - 2D_l K_s x)^{\frac{1}{2}}. \quad (1.29)$$

Throughout this PhD the convention will be used that a shock emanating from the free surface will be labelled 2, a shock from the base of the flow 1 and a shock separating two regions of pure constituent 3. They then used the fact that, at any position along the chute, the depth-integrated flux of small particles must be equal to the inflow flux, i.e.

$$\int_0^h \gamma \rho_s z \, dz = \int_0^{z_1} \gamma z \, dz + \int_{z_1}^{z_2} \gamma \rho_s z \, dz, \quad (1.30)$$

which is easily evaluated to give the equation of shock 1 as

$$z_1 = (2D_l K_s \eta_0 \sigma^3 x)^{\frac{1}{2}}, \quad (1.31)$$

where  $\eta_0$  is  $\eta$  evaluated at  $x = 0$ . The intersection of these two lines marks the point that full segregation first occurs. The point is given by

$$x_s = \frac{h^2}{2D_l K_s (1 + \eta_0 \sigma^3)}, \quad (1.32a)$$

$$z_s = \left( \frac{\eta_0 \sigma^3}{1 + \eta_0 \sigma^3} \right)^{\frac{1}{2}} h. \quad (1.32b)$$

This solution is easily summarised in the following equations,

$$\left. \begin{aligned} z_1 &= (2D_l K_s \eta_0 \sigma^3 x)^{\frac{1}{2}}, & \text{in } 0 \leq x \leq x_s, \\ z_2 &= (h^2 - 2D_l K_s x)^{\frac{1}{2}}, & \text{in } 0 \leq x \leq x_s, \\ z_3 &= \left( \frac{\eta_0 \sigma^3}{1 + \eta_0 \sigma^3} \right)^{\frac{1}{2}} h, & \text{in } x > x_s, \end{aligned} \right\}. \quad (1.33)$$

which splits the domain into three regions. Above the line  $z_2$  for  $x \leq x_s$  and above  $z_3$  for  $x > x_s$ ,  $\eta = 0$  i.e. this region is filled purely with large particles. Between  $z_1$  and  $z_2$ ,  $\eta = \eta_0$  i.e. the homogeneously mixed inflow exists for a triangular domain enclosed by the 0% fall line and 100% concentrations line. Below  $z_2$  for  $x \leq x_s$  and below  $z_3$  for  $x > x_s$ ,  $\eta = \infty$  i.e. these regions contain purely small particles.

It has already been pointed out that the above analysis is not correct. The correct solution and the differences will be discussed in §3.1.5 in more detail.

### 1.3.4 Laboratory experiments

Savage & Lun also performed experiments on binary mixtures of large and small grains for flows down inclined chutes. They used glass beads where the small grains

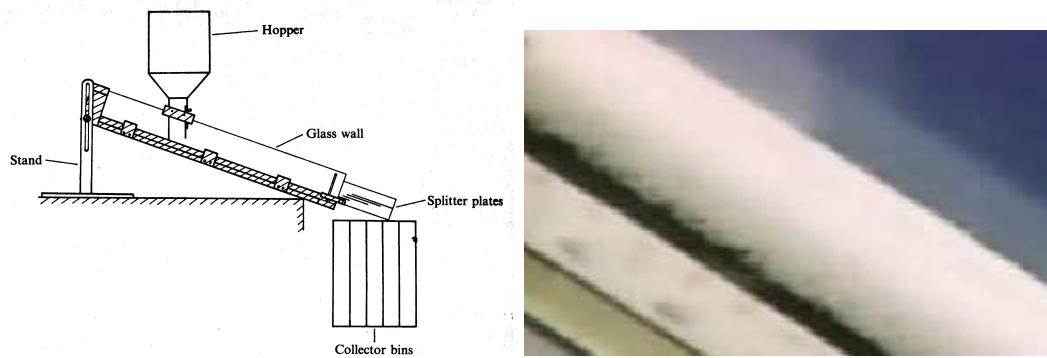


Figure 1.2: Diagram showing the experimental configuration of the experiments of Savage and Lun. The left panel shows a diagrammatic version of the equipment setup (taken from [72]). The right panel shows a still extracted from an animation of the experiments. In this the large particles are white and the small particles black, the shape segregation is apparent in this image

had a mean diameter of 0.943mm and the large 1.6mm, this implies  $\sigma = 0.589$ . The mean angle of repose was measured to be 25 degrees for both size particles. The chute was constructed such that it had smooth transparent glass side walls and a rough bottom. Its dimensions were 1 meter in length and 75 mm in width. A series of splitter plates were used to split the flow into five distinct layers. Each of these layers was directed into different collector bins. The concentration of fines was measured in each of the bins. The location of the feeding hopper could be moved and by changing the distance between the hopper and the splitter-plates, the full structure of the segregating flow could be built up, with a series of experiments.

They performed experiments at different flow depths and angles of inclination and found good agreement with the theory, especially in the relatively slow flow case. The physical information about the voids was computed assuming there were five particles around each void space. This information is exact for this configuration, but can be considered only approximate for real flow. Whereas, the information about packing fraction and bulk properties was experimentally determined using the data of Bridgewater *et al.* [9], who measured the percolation rate of a single small particle through a sheared bed of large granular material. The disagreement, between theory and experiment, increased with greater flow speed as diffusive remixing effects are apparent here. In this region, models based on the kinetic theory are more applicable.

The general theory predicts a longer segregation length than the dilute limit for  $\eta = 0.1$  and  $\eta = 0.15$  and does appear to give better agreement to the experimental results. At this point, it is worth pointing out that a correct application of a shock condition would increase the predicted segregation length and, hence, increase the accuracy of the dilute limit, this is discussed in more detail in section 3.1.5.

## 1.4 Aim of the thesis

Since the Savage & Lun theory [72] gives such good agreement with the experimental results, the question arises of what remains to be done on this topic and what is the aim of this thesis. Despite the apparent good agreement between this theory and experiments there are a few problems with it. Firstly, the question of what happens to gravity arises. In the above model the direction of segregation artificially appears as the direction the “fluctuating sieve” must act in. Additionally, there are no parameters which are affected by the strength of the gravitation field. Hence, this predicts that there will be no change in segregation length,  $x_s$ , as the strength of gravity is changed. This also raises the interesting question of what happened in the limit of zero gravity. Clearly if there is no gravitational field present the “fluctuating sieve” cannot be active, so this theory would predict a sudden stop in the segregation process at this point rather than a gradual increase in  $x_s$ , as  $g$  is decreased. Later, more detailed experiments by Valance & Savage [85] were performed. They reduce the effect of gravity by submerging the flow in a fluid and showed an increase in segregation length as gravity was reduced, this is discussed in more detail in section 6.

The reason for the absence of gravity in the Savage & Lun model is because of the way particles fall from one layer to another. If there is a space available the particle instantaneously falls and fills the space. In reality when a void is available and the particle is inside its capture width, it would start to fall under the influence of gravity. Also the particles are not contained within layers but are completely randomly distributed, therefore, to capture gravity the “fluctuating sieve” mechanism needs to

Number of particles around a void in a layer	$M/N$	$\bar{E}$	$k_{AV}$
3 (closest packing)	2.0	0.1547	0.466
4 (simple cubic)	1.0	0.414	0.63
5	0.6	0.701	0.712
6	0.5	1.000	0.765

Table 1.1: Values of various physical quantities for packing of equal sized spheres around a void, for the Savage-Lun Theory. Taken from p321 of [72]

be replaced with a continuum momentum balance description of this falling process that does not rely on the particles being contained within layers. Such a formulation of the “kinetic sieving” will be considered in §2.

Another major drawback of their model is its complexity. There are a host of parameters and variables in the final equation, which either, have to be experimentally determined, approximated by assuming perfectly spherical particles clustered around a void or estimated using physical arguments. This makes it very hard to apply in a quantitative way, as there is a degree of arbitrariness in these approximations. A classic example of this is the assumption that there are five equal sized particles around each void, this number was chosen because it was “felt to be reasonable ... for the present inclined-chute experiments”. Changes to the number of particles assumed to be around the void has a significant effect of the segregation length. Table 1.1 shows the change in value of varies quantities, which appear in the Savage & Lun theory against number of voids round a sphere. Assuming, as Savage & Lun do, that  $k_{LT} = 1.0$  and  $E_m = 0.1547$ , from (B.5), it is clear that the model would break down if there were only three spheres round each void, as  $\bar{E} = E_m$ . In addition, changing the assumed number of particles from 4 to 5 changes the segregation length, for the case  $\sigma = 0.5$ , by a factor of 4.8. The model breaks down again for six particles as the voids start to become too small to fit particles in.

## 1.5 Mixture theory

The model will be formulated using the framework of mixture theory, which is often used to study porous media flow problems (e.g. the flow of gas, oil and water mixtures through a deformable porous matrix) [63], sea ice dynamics [37], snow metamorphism [69], determining the properties of concrete [87], swelling of chemically active saturated clays [29] and many more applications.

Mixture theory deals with *partial* variables that are defined per unit volume of the mixture rather than *intrinsic* variables associated with the material, i.e. the values you would measure experimentally. The basic mixture postulate states that every point in the mixture is ‘occupied simultaneously by all constituents’, and, hence, at each point in space and time there are overlapping particle velocities (displacements) associated with the different constituents.

Since each constituent is assumed to exist everywhere, a volume fraction  $\phi^\nu$  is used to represent the percentage of the *local* volume occupied by constituent  $\nu$ . Clearly,

$$\sum_{\nu=1}^n \phi^\nu = 1, \quad (1.34)$$

where  $n$  is the number of constituents in the problem. Conservation laws can be derived for each individual constituent. The conservation laws for mass, momentum, energy and angular momentum are

$$\frac{\partial \rho^\nu}{\partial t} + \nabla \cdot (\rho^\nu \mathbf{u}^\nu) = m^\nu, \quad (1.35a)$$

$$\rho^\nu \frac{D_\nu u_i^\nu}{Dt} = \frac{\partial \sigma_{ij}^\nu}{\partial x_j} + \rho^\nu b_i^\nu + \beta_i^\nu + \tilde{\beta}_i^\nu, \quad (1.35b)$$

$$\rho^\nu \frac{D_\nu U^\nu}{Dt} = \rho^\nu r^\nu + \rho \left( \psi^\nu + \tilde{\psi}^\nu \right) - \frac{\partial q_j^\nu}{\partial x_j} + \delta_{ij} \sigma_{i\alpha}^\nu D_{\alpha j}^\nu, \quad (1.35c)$$

and

$$\psi^\nu = -\frac{1}{2} \sum_{\kappa=1}^n \delta_{ij} \left( \lambda_{i\alpha}^{\nu\kappa} (W_{\alpha j}^\kappa - W_{\alpha j}^\nu) \right) + \beta_i^{\nu\kappa} (v_i^\nu - v_i^\kappa), \quad (1.35d)$$

respectively, where  $\frac{D_\nu}{Dt} = \frac{\partial}{\partial t} + u_i^\nu \frac{\partial}{\partial x_i}$  is the total derivative moving with constituent  $\nu$ . The host of parameters which appear in the theory are summarised in table 1.2. The generality of the theory is clear from (1.35). For example, when considering sea-ice,

Variable	Description
$\rho$	Density
$t$	Time
$u^\nu$	Velocity of constituent $\nu$
$m^\nu$	Rate of mass transfer to constituent $\nu$ per unit mixture volume
$m^{\nu\kappa}$	Rate of mass transfer to constituent $\nu$ from constituent $\kappa$
$\sigma_{ij}^\nu$	Partial stress tensor of constituent $\nu$
$b_i^\nu$	Body force per unit mass on constituent $\nu$
$\beta_i^\nu$	Interaction body forces on constituent $\nu$ per unit mixture mass
$\tilde{\beta}_i^\nu$	Interacting body force due to mass transfer $m^\nu$
$r^\nu$	Rate of energy supply per unit mass of constituent $\nu$
$\psi^\nu$	Rate of energy transfer to constituent $\nu$ per unit mass (independent of transfer due to mass transfer)
$\tilde{\psi}^\nu$	Rate of energy transfer to constituent $\nu$ per unit mass (solely due to mass transfer)
$q_i^\nu$	Energy flux in constituent $\nu$ per unit mixture volume
$D_{ij}^\nu$	Partial strain rate of constituent $\nu$
$\lambda_{ij}^{\nu\kappa}$	The interaction couple on constituent $\nu$ from constituent $\kappa$
$W_{ij}^\nu$	Partial spin of constituent $\nu$
$\beta_i^{\nu\kappa}$	Interaction body forces on constituent $\nu$ from constituent $\kappa$
$u_i^\nu$	Velocity of constituent $\nu$
$U^\nu$	Energy of constituent $\nu$

Table 1.2: Summary of the variables used in full mixture theory in their most general form

[37], the ice is allowed to gain heat from the water, which in turn, melts the ice creating a mass transfer to the water and hence a drag force on the moving ice-block.

The reason for separating out the contribution to both the interaction body force and rate of energy supply due to mass transfer is because relationships can be shown between these and the  $m^\nu$ . The relationships between these quantities are simply given by,

$$\sum_{\nu=1}^n \rho \tilde{\beta}_i^\nu = \sum_{\nu=1}^n m^\nu v_i^\nu, \quad (1.36a)$$

$$\rho \tilde{\psi}^\nu = -\frac{1}{2} \sum_{\nu=1}^n m^{\mu\kappa} (U^\nu - U^\kappa). \quad (1.36b)$$

The  $\beta_i^\nu$  are representations of the internal forces between the constituent, so it is obvious from Newton's Third Law that

$$\sum_{\nu=1}^n \beta_i^\nu = 0. \quad (1.37)$$

Stating it in this form indicates that these internal drags are closely related to the intrinsic stress field of the constituents, this point will be expanded upon with an example in the next section.

Most of the variables appearing in the theory are partial not intrinsic, these are defined, such that, their sum is equal to the bulk quantity. For example,

$$\rho = \sum_{\nu=1}^n \rho^\nu, \quad (1.38)$$

this makes the bulk quantities easy to calculate, by simply summing over all constituents. Various relations can be shown between the intrinsic (the convention of a superscript \* denoting a intrinsic variable) and partial variables. The relationships for velocity and density are

$$\rho^\nu = \phi^\nu \rho^{\nu*}, \quad u^\nu = u^{\nu*}, \quad (1.39)$$

but no relationship can be shown between the partial and intrinsic stress of the constituents in general. For the case where the stress tensor can be represented by a hydrostatic pressure field, it is common in the application of mixture theory to assume a linear volume fraction scaling for the pressure as well i.e.

$$p^\nu = \phi^\nu p^{\nu*}. \quad (1.40)$$

From Archimedes' Principle, (1.40) can be shown to be correct for a fluid constituent interacting with a fluid constituent. Archimedes' principle states that the uplift on an object, submerged in a fluid  $a$ , is proportional to the weight of fluid displaced by the object, i.e.  $\rho^{a*}V|g|$  where  $V$  is the volume of the object. Therefore, for a collection of objects (particles) making up a constituent the following result must hold

$$\nabla p^\mu = -\rho^{a*} \mathbf{g} \Phi^\mu, \quad (1.41)$$

for the force per unit mixture volume. This can be integrated to give the contribution to individual partial pressure due to the presence of the fluid is and is in accordance with (1.40).

A similar argument cannot be constructed for the pressure due to the presence of the granular material, as there is no equivalent principle for the force on a granular material submerged in other granular material. In §2.2, the particle size segregation theory departs from this standard pressure relationship, since the bulk pressure is not shared in proportion to the local volume fraction of each constituent.

### 1.5.1 Slow flow of a viscous fluid flow through a porous matrix

As discussed in the general framework, in mixture theory, the interaction is broken down into the stress tensor and the internal forces. To solve any physical problem the form of these interaction terms needs to be determined. In this section, the problem of determining the internal drag for the viscous fluid phase flowing slowly through a porous matrix, will be considered. This will be seen to be closely related to segregation in granular flows as the small particles can be thought of as percolating slowly through a porous media.

Henry Darcy, in Appendix D of [17], published the results from a series of experiments to determine the law of slow viscous fluid flow through a porous matrix. These original experiments were performed using siliceous sand of the Saone and water. The conclusions were

“ It thus appears that for sand of comparable nature, one can conclude that output volume is proportional to the head and inversely related to the thickness of the layer traversed.”

Later this result has been generalised to include the effect of changing the viscosity of the fluid. Hence, it is normally stated, for example [6], as

$$-\nabla p^{f*} = \frac{\mu}{k} \mathbf{Q} \quad (1.42)$$

where  $\mu$  is the viscosity of the fluid,  $k$  is the matrix permeability and  $\mathbf{Q}$  is the volume of fluid discharged per unit time per unit area. The superscript  $f$  is just used to indicate that this pressure drop is applied to the fluid constituent. It is clear, that  $\mathbf{Q}$  is just  $\phi^f \mathbf{v}^f$  written in terms of the mixture theory variables and if the matrix is also allowed to move then the most general form of Darcy Law is

$$-\nabla p^{f*} = \frac{\mu \phi^f}{k} (\mathbf{v}^f - \mathbf{v}^s), \quad (1.43)$$

where  $\mathbf{v}^s$  is the velocity of the matrix.

So far, we have expressed Darcy's Law in its most general form in terms of the framework of mixture theory. For rocks and aggregates there is a range of permeabilities of  $k \approx 10^{-7} \rightarrow 10^{-16} \text{m}^2$  and for gas, water and oils a range a viscosity range of  $\mu \approx 10^{-5} \rightarrow 10^{-3} \text{Pa s}$ . It can be shown that for slow flow with zero body force and no mass transfer within these ranges of parameters the momentum balance equation (1.36a) is reduced to

$$\rho \boldsymbol{\beta} = -\nabla p^f. \quad (1.44)$$

The partial pressure gradient can be expanded in terms of intrinsic variables, with application of (1.40), i.e.

$$\frac{\partial p^f}{\partial x} = \phi^f \frac{\partial p^{f*}}{\partial x} + p^{f*} \frac{\partial \phi^f}{\partial x}. \quad (1.45)$$

Substitution of (1.45) and (1.43) into (1.44) leads to an expression for the Darcy drag of

$$\rho \boldsymbol{\beta} = -\frac{\mu}{k} (\phi^f)^2 (\mathbf{v}^f - \mathbf{v}^s) + \frac{p^f}{\phi^f} \nabla \phi^f. \quad (1.46)$$

Now that the drag has been determined, the problem is closed and can be solved for various situations. Numerous problems that include a viscous fluid where this Darcy drag is used can be found in [63].

There is an alternative way of looking at the way this result is derived. The pressure gradient and drag terms are modelled together by specifying a rule for the intrinsic pressure gradient. A proposed relationship between the intrinsic pressure and other variables can be used to derive a drag relation. This is the normal situation when considering complex fluids. An experimentally, or physically, derived form of the intrinsic stress tensor will be known and can then be used in the above manner to calculate the internal drag between the constituents; this creates in the framework of mixture theory. This is exactly what is done when modelling the load distribution in §2.2.1

# Chapter 2

## A Theory for particle size segregation in granular free-surface flows

### 2.1 Mixture framework and conservation laws

In this chapter, a simple two-component particle size segregation model will be formulated ignoring the effects of air. The granular material is assumed to be a bi-dispersed mixture of ‘large’ and ‘small’ particles. The constituent letters  $l$  and  $s$  will be used for the ‘large’ and ‘small’ particles throughout. This problem will be formulated using the framework of mixture theory, as introduced in §1.5. Since a two constituent model is being considered (1.34), implies

$$\phi^s + \phi^l = 1. \tag{2.1}$$

In reality the flow consists of three-constituents, the additional component being the ‘void’ space between the particles. The effect of including this space is minor and is discussed in more detail in §6.

A granular free-surface flow will automatically find its own energy equilibrium. In these flows, energy is removed by friction, with the base of the chute and inelastic

collisions between particles. There is an input of gravitational potential energy resulting from the materials' motion downslope. If the rate of energy input is greater than the rate of removal, from the system, the kinetic energy of individual particles will increase leading to a greater number of collisions and, hence, bring the material back to equilibrium. Therefore, it is a very good assumption that there is no net flow of energy into or from the flow, hence, the general conservation of energy, (1.35c), will not be considered. In the molecular dynamics simulations discussed in §1.2.1, the reaching of this balance between gravitational input and dissipation of energy in the system is used as the definition of achieving steady-state and the end of any transients. This gives further weight to the validity of this assumption for the flow regimes under consideration here. It has already been discussed in §1.1, that as the total kinetic energy of the flow is increased, this model will break down and a binary collision model, for example [52], needs to be considered.

Additionally, the particles are not allowed to break or amalgamate, therefore, there is zero mass transfer between the constituents implying  $m^\mu = 0$ . The stress tensor will be assumed to be approximated by a hydrostatic pressure field

$$\sigma_{zz}^\mu = -p^\mu. \quad (2.2)$$

Even in granular statics the principle stress axis ( $\sigma_{11}, \sigma_{22}$ ) dominates, and in the case of avalanching this assumption is an extremely good approximation. For details of why this term is the leading order term for avalanching material, see [38] for details, or Appendix A for an outline.

The only body force in this problem will be gravity and it will have the same effect on both constituents, hence,

$$b_i^\mu = g_i. \quad (2.3)$$

Under these circumstances the general framework of mixture theory (1.35) is reduced to

$$\frac{\partial \rho^\mu}{\partial t} + \nabla \cdot (\rho^\mu \mathbf{u}^\mu) = 0, \quad (2.4a)$$

for mass and

$$-\nabla p^\mu + \rho^\mu \mathbf{g} + \rho^\mu \boldsymbol{\beta}^\mu = \rho^\mu \frac{D_\mu \mathbf{v}^\mu}{Dt}, \quad (2.4b)$$

for momentum. Experimental observations of size segregation in granular flows, on the geological scale [11, 47], in industrial flows [61, 74, 36] and on the laboratory scale [72, 85] all show that the ratio of the segregation length ( $L$ ), defined as the distance at which a fully segregated state is first observed, is an order of magnitude greater than the thickness of the avalanche. This leads to the conclusion that in the normal direction the acceleration term can be neglected and the momentum equation (2.4b) is further reduced to

$$-\nabla p^\mu + \rho^\mu \mathbf{g} + \rho \boldsymbol{\beta}^\mu = 0. \quad (2.5)$$

The bulk density,  $\rho$ , and the bulk pressure,  $p$ , are defined as the sum of the partial densities and partial pressures, hence,

$$\rho = \rho^l + \rho^s, \quad p = p^l + p^s. \quad (2.6)$$

Since this is a two component model, it follows from (1.37) that

$$\boldsymbol{\beta}^s = -\boldsymbol{\beta}^l, \quad (2.7)$$

which is simply a statement that the drag applied to the small constituent by the large, is equal and opposite to that applied by the small on the large constituent.

The relationship between the intrinsic variables and their partial counterparts for velocity and density are given by (1.39), whereas, as previously noted, for the pressure, the standard linear volume fraction scaling will be modified.

## 2.2 The particle size segregation model

Let  $Oxyz$  be a coordinate system with the  $x$ -axis pointing down a chute inclined at an angle  $\zeta$  to the horizontal, the  $y$ -axis across the chute and the  $z$ -axis being the upward pointing normal as shown in figure 2.1. The large and small particles are assumed to have the same constant density

$$\rho^{l*} = \rho^{s*}, \quad (2.8)$$

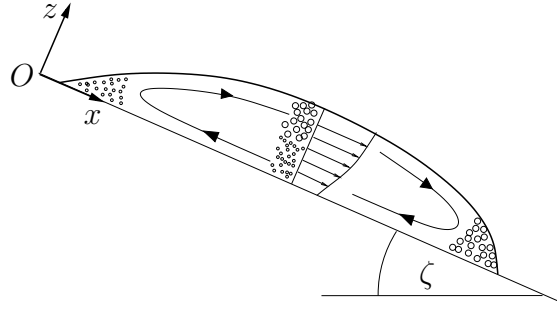


Figure 2.1: A diagram showing the coordinate system  $Oxz$  with the  $x$ -axis pointing down a chute, which is inclined at an angle  $\zeta$  to the horizontal. The  $y$ -axis is into the plane of the paper and the  $z$ -axis is normal to the slope. Particle-size segregation takes place within the avalanche creating inversely-graded layers. In the centre of mass frame the velocity field is such that the material is circulated round, as indicated by the solid line. When shear is present, the large particles have a tendency to move towards the front of the flow and the fines towards the rear.

which is necessarily equal to the bulk density,  $\rho$ . Here and through this thesis the  $*$  is being used to indicate an intrinsic variable. It should be emphasised that, since the interstitial pore space has been incorporated into each phase, the intrinsic densities,  $\rho^{\mu*}$ , are in fact the mean solids fraction multiplied by the bulk solid density, therefore, (2.8) implicitly assumes that the mean solids fraction is a constant, which is consistent with the results of Vallance [84]. The sum of the normal momentum balance component (2.4b) over large and small constituents, implies

$$-\frac{d}{dz} (p^l + p^s) - (\rho^s + \rho^l)g \cos \zeta + \rho(\beta^s + \beta^l) = 0, \quad (2.9)$$

where  $g$  is the constant of gravitational acceleration. Using (2.6), (2.1) and (2.7), the bulk pressure can be shown to be

$$\frac{dp}{dz} = -\rho g \cos \zeta. \quad (2.10)$$

Since  $\rho$  is constant and the free-surface is traction free, (2.10) can be integrated through the avalanche depth,  $h$ , revealing that the bulk pressure is hydrostatic

$$p = \rho g(h - z) \cos \zeta. \quad (2.11)$$

The key idea behind the kinetic sieving model is that, whilst the small particles percolate through the matrix, they support less of the overburden pressure, and

the large particles must, therefore, carry proportionately more of the load. A new pressure scaling is therefore introduced

$$p^l = f^l p, \quad p^s = f^s p, \quad (2.12)$$

where the factors  $f^l$  and  $f^s$  determine the proportion of the hydrostatic load that is carried by the large and small particles. Specific forms for these factors will be proposed later, but it is worth noting that (2.6) implies that they must sum to unity

$$f^l + f^s = 1. \quad (2.13)$$

### 2.2.1 Determining the drag law

To close the model, the interaction drag needs to be specified, which will be performed in a similar manner to the determination of the Darcy drag in §1.5.1. In the example discussed in §1.5.1, a pressure gradient leads to a proportional difference in velocity between matrix and fluid. The simplifications made to the momentum equations for this situation are similar to the ones for this granular model. In this situation, each constituent takes a share of the overburden pressure, which was discussed above, its share is given by  $f^\mu \nabla p^*$ . Due to the similarity with Darcy's Law, it seems reasonable to assume that this pressure gradient will drive a linear velocity difference between this constituent and the matrix, i.e.

$$f^\mu \nabla p^* = c \rho^\mu (\mathbf{u} - \mathbf{u}^\mu), \quad (2.14)$$

where  $c$  is the coefficient of inter-particle drag and

$$\mathbf{u} = (\rho^l \mathbf{u}^l + \rho^s \mathbf{u}^s) / \rho, \quad (2.15)$$

is the bulk velocity. It should be noted, that  $c$  has dimension of  $s^{-1}$ , and  $1/c$  is a measure of the time taken for a particle to percolate a set distance for a given pressure gradient. Hence, physically,  $c$  is a measure of the resistance on a particle to its percolation from the matrix. Equation (2.14) states that for each constituent its share of the overburden pressure drives a flow relative to the bulk flow, which itself is just given by the barycentric velocity of the two constituents.

Due to the use of the non-standard pressure scaling (2.12), the expansion of the partial pressure, (2.14), in terms of the intrinsic pressure takes the form

$$\frac{\partial p^\mu}{\partial x} = f^\mu \frac{\partial p}{\partial x} + p \frac{\partial f^\mu}{\partial x}, \quad (2.16)$$

which is more general than the standard expression (1.45). Following the same procedure as §1.5.1 leads to an interaction drag of the form

$$\rho \boldsymbol{\beta}^\mu = p \nabla f^\mu - \rho^\mu c (\mathbf{u}^\mu - \mathbf{u}), \quad \mu = l, s. \quad (2.17)$$

In terms of the Savage-Lun model this drag is a continuum version of the “squeeze expulsion” mechanism for the momentum balance. Since its effect is to induce a difference in velocity between the constituent and the bulk flow. As the bulk flow velocity is linked back to the constituent velocity through the definition of the barycentric velocity (2.15), this automatically enforces that there is no momentum transfer between the two constituents in regions of 100% concentration. Additionally, (2.7) means the momentum lost by one constituent is gained by the other, hence, no momentum is lost or gained by this mechanism. The constant of proportionality,  $c$ , is a measure of how much force is required to create a velocity difference of a given magnitude, i.e. the lower the value, the easier it is for particles to slide past one another. In general, this constant would be expected to depend on material properties like particle shape and surface roughness, but not on kinematic properties.

### 2.2.2 Individual constituent velocities

The large and small particle percolation velocities are assumed to be of the same order of magnitude as the normal bulk velocity, but much smaller than typical bulk downstream velocities. To reflect this, the constituent velocities in the down and cross-slope directions are assumed to be equal to the bulk down and cross-slope velocity components, i.e.

$$u = u^\mu, \quad v = v^\mu, \quad \mu = l, s. \quad (2.18)$$

Whilst the normal constituent velocities,  $w^\mu$ , are obtained by substituting (2.17) into the normal component of the momentum balance equation (2.5), to give

$$\nabla p^\mu = -\rho g \cos \zeta + p \nabla f^\mu - \rho^\mu c (w^\mu - w). \quad (2.19)$$

Expanding the right hand side of (2.19), using (2.16), and eliminating the dependence of the pressure, using (2.12), leads to an expression for the normal to chute velocity, for each constituent, relative to the bulk velocity

$$\phi^\mu w^\mu = \phi^\mu w + (f^\mu - \phi^\mu)(g/c) \cos \zeta, \quad \mu = l, s. \quad (2.20)$$

The significance of the pressure scalings  $f^\mu$  is now clear. If  $f^\mu > \phi^\mu$ , then the particles will rise, if  $f^\mu < \phi^\mu$  the particles will fall and if  $f^\mu = \phi^\mu$ , there will be no motion relative to the bulk normal flow.

Written in this form, (2.20) is a flux conservation equation, which has been derived from a momentum balance equation. Physically this equation states that the flux of small particles is comprised of three parts; the first term on the right hand-side represents the flux due to advection with the bulk flow. The second term consists of two parts, a non-preferential part proportional to  $\phi^\mu$ , due to “squeeze expulsion” and the second part (proportional to  $f^\mu$ ) represents the “fluctuating sieve”. This will be discussed in more detail in the next section. With this observation it is now clear that,  $f^\mu > \phi^\mu$  means the “squeeze expulsion” flux is greater than the “fluctuating sieve” and on average the particles will rise and visa-versa for  $f^\mu < \phi^\mu$ .

### 2.2.3 The load sharing factors

Since  $\phi^l = 1 - \phi^s$ , the pressure scalings  $f^\mu$  can, without loss of generality, be assumed to be a function of the local volume fraction of small particles  $\phi^s$  only. The functional form must satisfy the constraint that when only one type of particle is present it must support the entire load, i.e.

$$\begin{aligned} f^l = 1, f^s = 0 & \quad \text{when} \quad \phi^s = 0, \\ f^s = 1, f^l = 0 & \quad \text{when} \quad \phi^s = 1. \end{aligned} \quad (2.21)$$

The  $f$  factors are equivalent to the “fluctuating sieve” mechanism in the Savage-Lun theory, as they can be considered to be a model of the percentage of particles that are falling for a given volume fraction and constituent. It should be possible to construct factors that give the same functional dependence as the ones Savage & Lun derived. By casting them into this form, gravity will be retained and a segregation direction clearly defined. For ease, the simplest non-trivial functions that satisfy the constraints (2.21) and the condition (2.13) will be considered. These are

$$\begin{aligned} f^s &= \phi^s - B\phi^s(1 - \phi^s), \\ f^l &= (1 - \phi^s) + B\phi^s(1 - \phi^s), \end{aligned} \quad (2.22)$$

where the non-dimensional factor  $B$  determines the magnitude of the pressure perturbation away from the hydrostatic. When the functions (2.22) are substituted into (2.20), they imply that the large and small particle percolation velocities, relative to the bulk, are

$$\begin{aligned} w^l - w &= +q\phi^s, \\ w^s - w &= -q\phi^l, \end{aligned} \quad (2.23)$$

respectively, where

$$q = (B/c) g \cos \zeta, \quad (2.24)$$

is the mean segregation velocity. The large particles, therefore, move up through the matrix at a velocity proportional to the volume fraction of small particles, whilst the small particles drain down at a velocity proportional to the volume fraction of large particles. In both cases, the segregation stops when a 100% concentration of that constituent is reached.

## 2.2.4 The segregation equation

An equation to compute the volume fraction,  $\phi^s$ , can be formulated by substituting (2.23) into the mass balance (2.4a) for the small particles, to give

$$\frac{\partial \phi^s}{\partial t} + \frac{\partial}{\partial x}(\phi^s u) + \frac{\partial}{\partial y}(\phi^s v) + \frac{\partial}{\partial z}(\phi^s w) - \frac{\partial}{\partial z}(q\phi^s\phi^l) = 0. \quad (2.25)$$

It is immediately clear that, the governing equation for the large particles has exactly the same form with the only difference being that there is an opposite sign in the final

segregation term, since the volume fractions are related through (2.1). Physically this says that the large particles are advected with bulk flow, but the segregation ‘force’ is in the opposite direction. Without any loss of generality, only the equations for the small particles will be considered from this point onwards.

The bulk flow,  $\mathbf{u} = (u, v, w)$ , can either be prescribed or computed from the avalanche models discussed in §1.2. Both sets of models assume that the granular avalanche is incompressible i.e.

$$\frac{\partial u}{\partial x} + \frac{\partial v}{\partial y} + \frac{\partial w}{\partial z} = 0, \quad (2.26)$$

with constant uniform bulk density and a hydrostatic pressure distribution through their depth. This is consistent with the bulk density and pressure fields assumed in this model, and the incompressibility condition is recovered by summing the mass balance equations (2.4a) over the large and small constituents and using (2.8).

## 2.3 Comparison with the Savage & Lun theory

Direct comparison between the two models governing equations (2.25) and Savage and Lun’s (1.27) is difficult, as the Savage-Lun theory is formulated in terms of the number density ratio,  $\eta$ , and the particle diameter ratio,  $\sigma$ , instead of volume fractions. Relationships between these different variables are easily obtained by expressing the volume fraction relations in terms of the number and diameter of the particles. Physically the volume fraction of each constituent is the total volume of that constituent over the total volume of both constituents, i.e.

$$\phi^s = \frac{n_s(D_s)^3}{n_l(D_l)^3 + n_s(D_s)^3}, \quad \phi^l = \frac{n_l(D_l)^3}{n_l(D_l)^3 + n_s(D_s)^3}. \quad (2.27)$$

Dividing top and bottom of these results by  $n_l(D_l)^3$  reveals the relationship between the number density and the volume fraction variables, is given by

$$\phi^l = \frac{1}{1 + \eta\sigma^3}, \quad \phi^s = \frac{\eta\sigma^3}{1 + \eta\sigma^3}, \quad (2.28)$$

revealing a connection between the microscopic variables like number density,  $\eta$ , and the macroscopic variables, for example, volume fraction  $\phi$ . It is possible to write

(1.27) in terms of these macroscopic variables, using (2.28), (1.25) becomes

$$q_{N_l} = q_{SL}\phi^s, \quad (2.29a)$$

$$q_{N_s} = -q_{SL}\phi^l. \quad (2.29b)$$

where

$$q_{SL} = q_l - q_s. \quad (2.30)$$

On substitution back into the small particle mass balance equation (1.27) and application of (1.25), the following results for the small particles is revealed

$$\gamma z \frac{\partial \phi^s}{\partial x} - \frac{\partial}{\partial z} (q_{SL}\phi^s\phi^l) = 0. \quad (2.31)$$

To be consistent with (2.1) the volume voids ratio  $e$  has been taken to be zero, in (1.25). This is because in this model only the solid volume has been considered. Equation (2.1) can easily be generalised to allow for this constant voids space by replacing it with  $\phi^s + \phi^l + e = 1$ , which does not change the result as the constant cancels out. This and other generalisations to the derivation presented above are discussed in more detail in §6.

Writing (1.27) in the form of (2.31) it is clear that this is equivalent to the steady state version of (2.25) with the bulk flow velocity field taken to be  $\mathbf{u} = (\gamma z, 0, 0)$ , which is in agreement with the bulk velocity assumption of Savage & Lun. The models only differ in their definitions of the segregation velocities  $q$  and  $q^{SL}$ , in (2.24) and (2.30). A significant advantage of the new theory is that the segregation velocity is dependent on the normal component of gravity,  $g \cos \zeta$ , which automatically defines the direction for segregation and ensures that there is no segregation in the absence of gravity. Even though the two equations have the same structure, the lack of gravity in the original Savage-Lun model makes it impossible to use this comparison to obtain expressions for the undetermined quantities  $c$  and  $B$ , in terms of the particle parameters. Additionally the new equation is more general and able to deal with any velocity profile and also provides information about the temporal development of segregating flows, which is essential for a large number of important applications including the fingering instability [67, 68].

The load sharing factors  $f^\mu$  were chosen to give the simplest possible mathematical structure that leads to segregation. This leads to a  $q$  that is constant, ultimately it may be possible to incorporate some of the other more complex dependencies of  $q^{SL}$ , but, for the remainder of this thesis, the constant case is investigated.

## 2.4 Non-dimensional segregation equation

Avalanche models all exploit the shallowness of the flow to derive a system of depth-averaged mass and momentum equations for the thickness and the mean downslope velocity. Anticipating that the bulk flow will be computed using such models, the variables are non-dimensionalised by the standard avalanche scalings

$$x = L\tilde{x}, \quad z = H\tilde{z}, \quad (u, v) = U(\tilde{u}, \tilde{v}), \quad w = (HU/L)\tilde{w}, \quad t = (L/U)\tilde{t}, \quad (2.32)$$

where  $U$  is a typical downslope velocity magnitude, and the typical avalanche length  $L$  is much larger than the typical thickness  $H$ . Dropping the tildes and the superscript  $s$ , the segregation equation (2.25) becomes

$$\frac{\partial\phi}{\partial t} + \frac{\partial}{\partial x}(\phi u) + \frac{\partial}{\partial y}(\phi v) + \frac{\partial}{\partial z}(\phi w) - S_r \frac{\partial}{\partial z}(\phi(1-\phi)) = 0, \quad (2.33)$$

where the non-dimensional segregation number

$$S_r = \frac{qL}{HU} \quad (2.34)$$

is the ratio of the mean segregation velocity to typical magnitudes of the normal bulk velocity,  $w$ . The non-dimensional form of the incompressibility condition (2.26) can be used to simplify the conservation form of the segregation equation (2.33) to

$$\frac{\partial\phi}{\partial t} + u \frac{\partial\phi}{\partial x} + v \frac{\partial\phi}{\partial y} + w \frac{\partial\phi}{\partial z} + S_r(2\phi - 1) \frac{\partial\phi}{\partial z} = 0, \quad (2.35)$$

which, when  $\mathbf{u}$  is given, is a classical first order quasi-linear equation for the volume fraction of small particles. When  $S_r \equiv 0$  there is no segregation and (2.35) reduces to the *tracer equation*, which has been used by Gray & Tai [33] and in later publication Gray, Tai and Hutter [34] to model the formation of stratification patterns in a

pre-segregated bi-disperse mixture. The non-dimensional segregation number  $S_r$  determines the strength of the segregation. Strong segregation is usually observed, [72], when there is a significant gradient in the downslope velocity through the avalanche depth, but segregation can also occur, over longer distances, in avalanches with weak shear. Avalanche models usually assume a *plug flow* regime with uniform down- and cross-slope velocity profiles, but vertical structure can easily be incorporated by the inclusion of *shape factors* (e.g. [70]) in the depth averages of  $u^2$ ,  $uv$  and  $v^2$  in the momentum transport terms, see section §1.2 for details. Both strong and weak shear can be generated in laboratory experiments, and it is therefore of interest to see what effect they have on the resulting particle size distribution.

# Chapter 3

## Analytical solutions

In this section a series of analytical solutions to the segregation equation (2.35) will be constructed. They will be used for two main purposes: firstly, to gain an understanding of both the mathematical and physical phenomena that the solutions of the equation possess and secondly they will be used as a test bed for the numerical algorithms developed in chapter 4. The solutions found will also be compared and contrasted to those of Savage & Lun, discussed in §1.3.3, and used to further analyse the differences and similarities between the two theories.

### 3.1 Steady-state segregation in steady uniform flows with homogeneous inflow conditions

The first problem that will be considered is the steady-state segregation generated by a homogeneous inflow of particles in a shearing flow. This is precisely the situation Savage & Lun [72] considered with their model and which they compared to a series of detailed laboratory experiments (for more details see §1.3). A slightly more general velocity field than simple shear, given by

$$u = u(z), \quad v = 0, \quad w = 0, \quad (3.1)$$

will be considered. Using conservation of mass, this velocity field implies that the avalanche is of constant thickness. Experimentally this situation is relatively easy

to reproduce. To achieve this requires that the angle of inclination of the chute is approximately equal to the angle of friction of the granular material being used.

Under the velocity field (3.1), the conservation form of the segregation equation (2.33) reduces to

$$\frac{\partial}{\partial x}(\phi u) - S_r \frac{\partial}{\partial z}(\phi(1 - \phi)) = 0, \quad (3.2)$$

where  $S_r$  is the non-dimensional segregation number given by (2.34). This must be solved subject to the condition that a homogeneous mixture of concentration  $\phi_0$  enters the chute at  $x = 0$ ,

$$\phi(0, z) = \phi_0, \quad 0 \leq z \leq 1, \quad (3.3)$$

and there is no normal flux through the free-surface or the base. Representing the segregation equation in flux form, (3.2), reveals its physical meaning, whereby the flux of small particles in the  $x$ -direction is  $\phi u$  and  $\phi(1 - \phi)$  in the  $z$ -direction. Therefore, no flux through the free-surface and base can mathematically be represented as,

$$\phi(1 - \phi) = 0, \quad \text{at } z = 0, 1. \quad (3.4)$$

This equation will be used to enforce no flux in the development of the analytical solution, but in the numerical solutions it will be imposed more directly. The numerical method calculates the numerical fluxes across boundaries between adjoining cells, therefore this flux will be set identically to zero across the top and bottom boundaries of the computational domain, details can be found in §4.

### 3.1.1 Characteristics

The conservative segregation equation (3.2) can be rewritten as a simple first order, quasi-linear equation by expanding out the derivatives to give

$$u \frac{\partial \phi}{\partial x} + S_r(2\phi - 1) \frac{\partial \phi}{\partial z} = 0. \quad (3.5)$$

Solutions to (3.5) may be constructed by the method of characteristics, which can be found in many textbooks, for example [2, 30, 77, 7]. The method of characteristics is a way of reducing a hyperbolic PDE to family of ODEs. Along a characteristic  $\phi$

is constant and will be taken to be equal to  $\phi_\lambda$ , this implies the equation is only a function of one variable, hence

$$x = x(r), \quad z = z(r), \quad (3.6)$$

where  $r$  is a measure of the distance along a given characteristic. Therefore, the derivative of  $\phi$  with respect to  $r$  will be given by

$$\frac{d\phi}{dr} = \frac{dx}{dr} \frac{\partial\phi}{\partial x} + \frac{dz}{dr} \frac{\partial\phi}{\partial z}. \quad (3.7)$$

Comparison with (3.5) reveals for the following results,

$$\frac{dx}{dr} = u, \quad \frac{dz}{dr} = (2\phi_\lambda - 1), \quad (3.8)$$

where the subscript  $\lambda$  is used to label the characteristic under discussion and is a constant along this curve. Eliminating  $r$  from (3.7) leads to a family of ODEs,

$$u \frac{dz}{dx} = S_r(2\phi_\lambda - 1), \quad (3.9)$$

which is equivalent to the original PDE (3.2). As  $\phi_\lambda$  is constant and  $u$  is a function of  $z$ , this is a separable equation that can easily be integrated once the velocity field is known. Solutions for general velocity fields can, however, be constructed by defining a depth-integrated velocity coordinate

$$\psi = \int_0^z u(z') dz', \quad (3.10)$$

which increases monotonically with increasing  $z$ , provided  $u > 0$ . Even though  $\psi$  has been used for this variable, it should not be confused with rate of energy transfer in the general framework of mixture theory, as in this model an energy equation is never considered or used. Since the avalanche velocity magnitude is set by the scalings (2.32), it may be assumed without loss of generality, that  $\psi = 1$  at the free surface  $z = 1$ . Differentiating the velocity transform (3.10) using the chain rule reveals,

$$\frac{d\psi}{dx} = u \frac{dz}{dx}. \quad (3.11)$$

Substitution of (3.11) into the characteristic equation (3.9) gives

$$\frac{d\psi}{dx} = S_r(2\phi_\lambda - 1), \quad (3.12)$$

which is independent of the prescribed velocity field, meaning that the constructed solution is valid for any field consistent with (3.1). The physical solution is simply obtained by inverting (3.10) for any prescribed  $u(z)$ . The solution of (3.12) is

$$\psi = S_r(2\phi_\lambda - 1)(x - x_\lambda) + \psi_\lambda, \quad (3.13)$$

where  $(x_\lambda, \psi_\lambda)$  is the initial position of the characteristic. Therefore, in transformed variables all characteristics are straight lines, the gradients of which are set by the non-dimensional segregation parameter and the small particle concentration. For regions with 100% concentration of large particles the characteristics propagate downwards with gradient  $-S_r$ , for regions with 100% concentration of small particles the characteristics propagate upwards with gradient  $S_r$  and for particles entering the domain with concentration  $\phi_0$  the characteristics has a gradient of  $S_r(2\phi_0 - 1)$ , which may point either upwards or downwards, depending on the value of  $\phi_0$ .

Physically, the characteristics represent the propagation of information into the domain. The boundary condition for the top and bottom boundary (3.4) have two solutions  $\phi = 0, 1$ . In order for information to propagate into and not out of the domain the condition  $\phi = 1$  must be enforced at the base of the flow and  $\phi = 0$  at the free-surface. The characteristics are illustrated for an inflow concentration of 60% in figure 3.1.

### 3.1.2 Segregation jump condition

As can be seen from figure 3.1 there are three lines on which the characteristics intersect. These are points where the inflow and boundary information meet and are inconsistent with each other. At these points the classical continuous solutions break down and shock conditions need to be applied to obtain a discontinuous solution. This is a common situation and the construction of these ‘shock conditions’ is discussed in detail, for the case of incompressible fluids, in [77], whereas [2] gives a treatment for numerous different problems, including traffic flow, gas dynamics, plasticity and the mechanics of granular materials. In [7] a more abstract treatment, independent of any underlying physical problem, can be found. In one-dimensional problems these

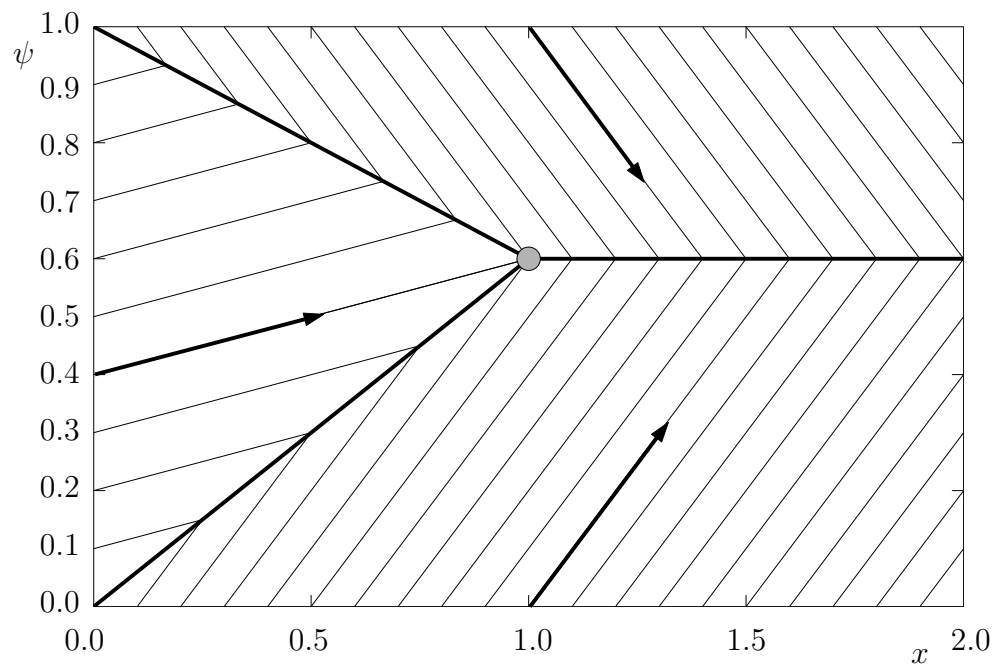


Figure 3.1: A plot of the steady-state solution in depth-integrated velocity coordinates  $(x, \psi)$  for an inflow concentration  $\phi_0 = 0.6$  and  $Sr = 1$ . The bulk flow is from left to right. The shocks (straight thick lines) meet at the triple-point (grey circle) and divide the domain into three regions. A homogeneous mixture enters from the left-hand side. The characteristics (straight thin lines) carry this information into the triangular region, as indicated by the arrow. The bottom layer is filled by small particles and have upward sloping characteristics, whilst the top layer is filled with large particles and have downward propagating characteristics, which intersect with one another at the shocks.

shocks arise due to characteristics whose paths converge and intersect, then shock conditions are used to continue the solutions beyond this point. Here it is due to an ‘incompatibility’ between inflow and boundary conditions and the solution is already known on both sides of the shock. Therefore, it will be used to check the boundary and inflow conditions are mathematically consistent and to determine the precise location of the discontinuity.

The jump or shock condition can be derived from an integral version of the conservative form of the segregation equation (3.2). Integrating this from  $L_1$  to  $L_2$  with respect to  $z$  gives

$$\frac{\partial}{\partial x} \int_{L_1}^{L_2} \phi u \, dz - S_r [\phi(1 - \phi)]_{L_1}^{L_2} = 0. \quad (3.14)$$

Assuming that there is a jump in  $\phi$  located at  $z = s(x)$ , equation (3.14) becomes

$$\frac{\partial}{\partial x} \left[ \int_{L_1}^{s^-} \phi u \, dz + \int_{s^+}^{L_2} \phi u \, dz \right] - S_r [\phi(1 - \phi)]_{L_1}^{L_2} = 0, \quad (3.15)$$

where the plus/minus superscripts denote evaluation of the limits on right/left side of the discontinuity respectively. Leibniz’s rule, e.g. §3.3.7 of [3], states

$$\frac{\partial}{\partial x} \int_{b(x)}^{a(x)} f(x, z) \, dz = \int_{b(x)}^{a(x)} \frac{\partial f(x, z)}{\partial x} \, dz - f(x, b(x)) \frac{\partial b}{\partial x} + f(x, a(x)) \frac{\partial a}{\partial x}, \quad (3.16)$$

which will be used to differentiate under the integral sign. Interchanging the order of differentiation and integrating using (3.16), (3.15) can be expressed as

$$\int_{L_1}^{L_2} \frac{\partial}{\partial x} (\phi u) \, dz - \frac{ds}{dx} [\phi u]_-^+ - S_r [\phi(1 - \phi)]_{L_1}^{L_2} = 0, \quad (3.17)$$

where the jump bracket  $[\phi]_-^+ = \phi^+ - \phi^-$  is the difference of the enclosed quantity on the forward and rearward sides of the shock. Shrinking the domain  $[L_1, L_2]$  onto the shock by taking the limits  $L_1 \rightarrow s^-$  and  $L_2 \rightarrow s^+$  yields the jump condition

$$[\phi u s' + S_r \phi(1 - \phi)]_-^+ = 0, \quad (3.18)$$

where  $s' = ds/dx$ . This can be rearranged to give

$$u \frac{ds}{dx} = S_r (\phi^+ + \phi^- - 1), \quad (3.19)$$

which is an ordinary differential equation for the position of the shock. Using depth integrated-velocity coordinates, defined in (3.10), (3.11) shows this can be transformed to

$$\frac{d\psi}{dx} = S_r(\phi^+ + \phi^- - 1), \quad (3.20)$$

which is independent of the assumed velocity profile.

### 3.1.3 Shock solutions in mapped coordinates

Savage & Lun's [72] experiments showed that a layer of 100% fines developed near the base and that there was a sharp concentration jump between this region and the homogeneous inflowing mixture. There is a simple physical explanation for this, as the mixture flows into the chute, small particles drain down through the matrix and in turn lever large particles towards the surface. The net effect of this is that the local volume fraction of small particles remains at the inflow concentration  $\phi_0$  throughout most of the flow, just as the solution by the method of characteristics suggests. However, at the lower boundary there are no more large particles to be levered up, and the no-normal flux condition (3.4) implies that a region of 100% fines develops at the base. This layer becomes progressively thicker downstream, because no large particles can be supplied from the pure phase. They also observed the development of a similar concentration shock near the free-surface, between a region of 100% large particles and the homogeneous mixture. This time the pure phase of large particles is generated because there are no more small particles to fall down through the matrix.

This is demonstrated in the characteristic diagram 3.1 which shows three different regions with  $\phi = 0, \phi_0$  and 1 separated by shocks. It still remains to compute and check the consistency of these boundaries (shocks) using the shock condition (3.20). The position of the lower shock, which separates the fines from the homogeneous mixture, can be computed from (3.20) by substituting  $\phi^+ = \phi_0$  and  $\phi^- = 1$  and integrating subject to the boundary condition that  $\psi = 0$  at  $x = 0$ . This implies

$$\psi_1 = S_r\phi_0x, \quad (3.21)$$

where, as before in §1.3.3, the subscript 1 is used to denote the lower shock. In depth integrated-velocity coordinates this grows linearly with downstream distance, as shown in figure 3.1, but, in general, when mapped back to physical coordinates, it will describe a curve. Specific results for a range of velocity profiles will be analyzed at the end of this section, once the complete solution has been constructed.

Using exactly the same arguments as above, the position of the top shock,  $\psi_2$ , can be computed by substituting  $\phi^+ = 0$  and  $\phi^- = \phi_0$  into (3.20) and integrating subject to the boundary condition  $\psi_2 = 1$  at  $x = 0$ , which implies

$$\psi_2 = 1 - S_r(1 - \phi_0)x. \quad (3.22)$$

This shock falls linearly from the free surface and meets the bottom shock at  $x_p = 1/S_r$  at a height  $\psi = \phi_0$  in depth-integrated velocity variables. When the two shocks merge a third shock is formed, between the pure phases of small and large particles, creating a *triple-point*. The final (third) shock position is determined by substituting  $\phi^+ = 0$  and  $\phi^- = 1$  into (3.20) and integrating to give

$$\psi_3 = \phi_0, \quad \text{for } x \geq x_p. \quad (3.23)$$

The solution consists of three domains of constant concentration, which are separated by straight shocks (3.21)-(3.23) in depth-integrated velocity coordinates  $(x, \psi)$ . This is exactly as illustrated in figure 3.1, confirming the inflow and boundary are consistent. The full structure is now clear, at  $x = 0$  the homogeneous mixture enters the domain and the initial concentration,  $\phi_0$ , is swept into the triangular region adjacent to the  $\psi$ -axis by the characteristics. At the base, and free-surface, there are no more large, or small, particles to propagate through the domain and pure phases of small and large particles develop near the base and free-surface respectively. Within these pure regions no further segregation takes place and the particles move downstream along constant height trajectories by virtue of (2.23). The small particles have characteristics that propagate upwards and the large ones propagate downwards. These eventually intersect, either with one another or with the characteristics from the homogeneous domain, to generate the three shocks.

### 3.1.4 Physical solutions

The beauty of the depth-integrated velocity coordinates is that the solution given by (3.21)–(3.23) is valid for all velocity fields that satisfy the constraint that  $u(z) > 0$ . To visualize specific results in physical coordinates, a velocity field must be prescribed and the integral (3.10) solved to obtain  $\psi = \psi(z)$ . A series of linear velocity profiles

$$u = \alpha + 2(1 - \alpha)z, \quad 0 \leq \alpha \leq 1, \quad (3.24)$$

are investigated here, where the parameter  $\alpha$  is used to generate plug flow,  $\alpha = 1$ , simple shear,  $\alpha = 0$ , and shear with basal slip, for intermediate values. The integral (3.10) implies that the depth-integrated velocity coordinate is

$$\psi = \alpha z + (1 - \alpha)z^2, \quad (3.25)$$

which has the property that at the free-surface  $\psi(1) = 1$ , as required. Note, for the case  $\alpha = 0$ , this velocity field (3.25) is equal to zero at the point  $z = 0$ . As this is an isolated point no problems arise with uniqueness when the integral transformation (3.10) is applied. This can easily be inverted to give the position of the shocks in physical space

$$z = \begin{cases} \psi, & \alpha = 1, \\ \frac{-\alpha + \sqrt{\alpha^2 + 4(1 - \alpha)\psi}}{2(1 - \alpha)}, & \alpha \neq 1. \end{cases} \quad (3.26)$$

The exact solutions are illustrated in figure 3.2 for a series of linear velocity profiles generated by parameter values of  $\alpha = 0, 1/2, 1$ , initial concentrations of  $\phi_0 = 50\%$  and  $30\%$  and for a segregation number  $S_r = 1$ . Plug flow is the simplest case as the physical and transformed coordinates are identical. The shocks and characteristics are therefore all straight lines, as described above. The solutions are shown in the top two panels using a contour scale, blue regions are small particle dominated, red regions large particle dominated, with the darker shades indicating a higher concentration and green represents equal volumes of both. For 50% inflow concentration, the third shock lies at  $z = 0.5$  to create an inversely-graded layer of large particles overlying small particles. At 30% inflow concentration, the solutions are similar, but the third shock lies at  $z = 0.3$ .

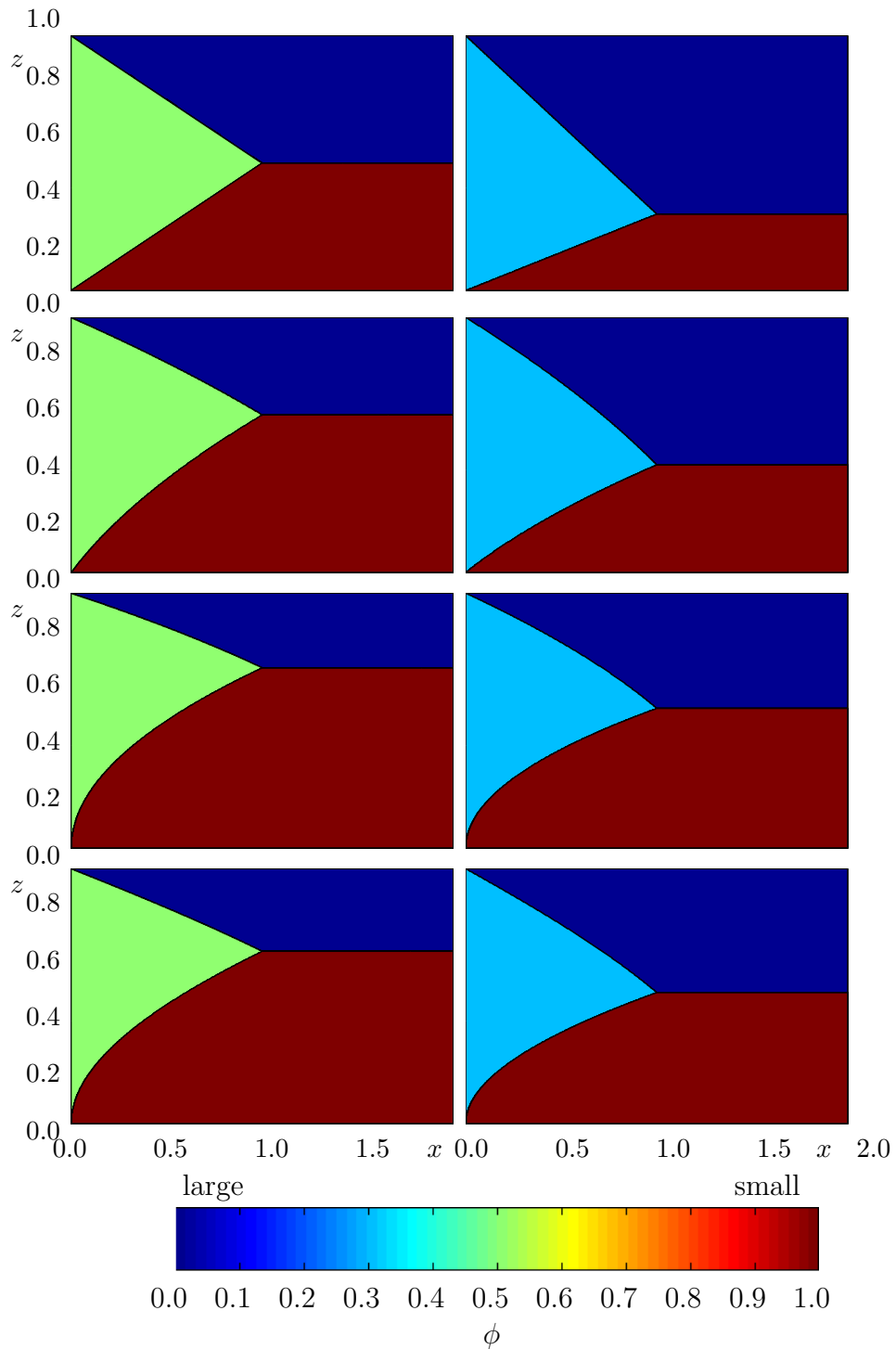


Figure 3.2: Steady-state solutions for the concentration of small particles  $\phi$  are shown as a function of the downslope coordinate  $x$  and avalanche depth  $z$ . The bulk flow is from left to right and the concentration is shown using a contour scale. A blue shading corresponds to higher concentrations of large particles than small, and red visa versa. Whereas green indicates an equal amount of both by volume fraction. The top 3 sets of panels assume linear velocity profiles corresponding to plug flow ( $\alpha = 1$ ), linear shear with basal slip ( $\alpha = 1/2$ ) and simple shear ( $\alpha = 0$ ), from top to bottom respectively. The bottom two panels correspond to Silbert et al.'s velocity  $u = 5(1 - (1 - z)^{3/2})/3$ . The left hand panels are for a homogeneous inflow concentration  $\phi_0 = 50\%$  and the righthand panels for  $30\%$ . The segregation number  $S_r = 1$ , implies that all of the solutions segregate fully at  $x = 1$ .

The intermediate case of shear and translation is often observed in physical flows and lies between simple shear and plug flow. Solutions for  $\alpha = 1/2$  are shown in the middle two panels of figure 3.2, i.e. for the velocity field  $u = z + 1/2$ . The shocks (3.21)–(3.23) and characteristics (3.13) are mapped to the physical space using the full quadratic mapping defined in (3.26). The solution, therefore, has the same basic structure as the other two cases. The upper and lower shocks are not straight lines, but are less curved than in simple shear and the lower shock has a finite gradient at the origin. The final layer thickness of large particles lies between that of uniform flow and simple shear in both the 30% and 50% concentration cases.

### 3.1.5 Comparison to Savage-Lun

For simple shear flow the solution is constructed by substituting the shock relations (3.21)–(3.23) into the mapping (3.26) with  $\alpha = 0$ , to give

$$\left. \begin{aligned} z_1 &= (S_r \phi_0 x)^{\frac{1}{2}} && \text{in } 0 \leq x \leq 1/S_r, \\ z_2 &= (1 - S_r(1 - \phi_0)x)^{\frac{1}{2}} && \text{in } 0 \leq x \leq 1/S_r, \\ z_3 &= (\phi_0)^{\frac{1}{2}} && \text{in } x > 1/S_r, \end{aligned} \right\} \quad (3.27)$$

which is illustrated in the second from bottom two panels of figure 3.2. The upper and lower shocks have square root profiles, with the lower one having an infinite gradient at the origin. The third shock is again straight, but it is significantly higher than in plug flow. This reflects the fact that there is a far greater total flux of particles in the upper fast moving layers of the flow than in the lower, slower moving layers.

Savage & Lun constructed steady-state solutions for this case, which were discussed in detail in §1.3.3. For (1.33) to be compared directly to (3.27), they firstly need to be non-dimensionalised using the scaling given in (2.32) and written in terms of volume fractions using the relations (2.27). Additionally a relationship between  $\eta_0$  and  $\phi_0$  must be obtained from their definitions this is clearly given by (2.28)<sub>2</sub> with  $\eta/\phi$  replaced with  $\eta_0/\phi_0$  respectively i.e.,

$$\phi_0^s = \frac{\eta_0 \sigma^3}{1 + \eta_0 \sigma^3}, \quad (3.28)$$

where  $\sigma$  is the ratio of the particle diameters. Putting all these results into (1.33) gives the Savage-Lun shock relations in terms of volume fractions as,

$$\left. \begin{aligned} z_1 &= \left( S_s \frac{\phi_0}{1 - \phi_0} x \right)^{\frac{1}{2}} && \text{in } 0 \leq x \leq (1 - \phi_0)/S_s, \\ z_2 &= (1 - S_s(1 - \phi_0)x)^{\frac{1}{2}} && \text{in } 0 \leq x \leq (1 - \phi_0)/S_s, \\ z_3 &= (\phi_0)^{\frac{1}{2}} && \text{in } x > (1 - \phi_0)/S_s, \end{aligned} \right\} \quad (3.29)$$

where

$$S_s = \frac{2LD_l K_s}{H^2}. \quad (3.30)$$

In general,  $K_s$  is a complicated function of  $\eta$ , hence  $S_s$  is not a constant. See Appendix B for details.

Superficially, (3.29) looks similar to (3.27) but these are based on an incorrect assumption, as discussed in §1.3.3. Instead of using a shock condition, Savage & Lun assumed that the fall line (or shock), marking the 0% fines region, was given by the characteristic curve emanating from the top of the inflow boundary. The authors then used the fact that, at any position along the chute, the depth-integrated flux of small particles must be equal to the inflow flux. The upper and lower shocks are steeper than those in the correct solution and therefore the distance for complete segregation is shorter. However, the conservation of the depth-integrated flux of small particles ensures that the final height of the third shock is correct. If shock conditions had been applied, the structure would be identical to that of (3.27), with the only difference being in the definition of the segregation strength  $S_s$  compared to  $S_r$ , as defined in (3.30) and (2.34) respectively.

As discussed in Appendix B, in the low  $\eta$  limit,  $K_s$  is a constant. From (B.5) and the scalings given in (2.32) it follows that in this limit  $S_s \rightarrow S_r$  and the theories predict exactly the same structure. This vindicates the choice of the form of the load factors (2.21), as this simplest form is just equivalent to the dilute limit of the Savage-Lun theory.

With this comparison complete it is clear that (3.27) represents the correct dilute limit solutions of the Savage-Lun theory, where (3.29) describes the incorrectly solved

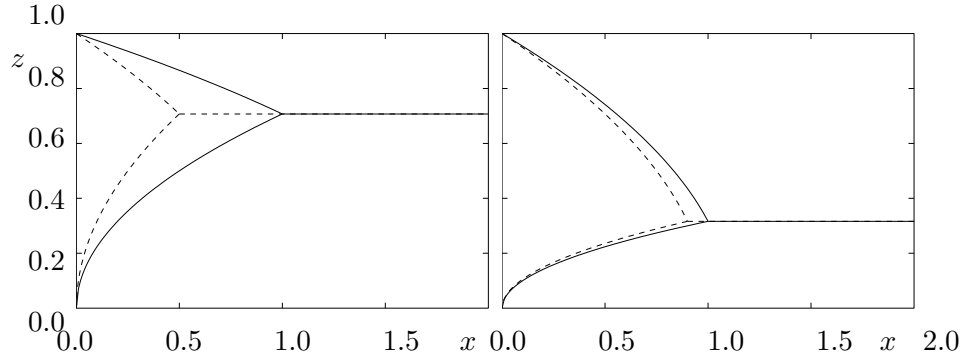


Figure 3.3: The shock positions for the Savage & Lun theory (3.29) (dashed line) and the current theory (solid line) (3.27) for homogeneous inflow concentrations of 50% (left panel) and 10% (right panel) in a simple shearing flow with  $S_r = 1$ . The distances for complete segregation to occur are comparable for the dilute case, but differ significantly at larger concentrations.

solution to the general Savage-Lun equations. As discussed in §1.3.4, their experiments showed very good agreement with the incorrect solution to the general theory. Figure 3.3 shows that for  $\eta = 0.1$ , which is in the range where the experiments were performed, there is only a small difference between the two solutions. Therefore, there is still very good agreement between the new theory and the experiments of Savage & Lun [72] and Vallance & Savage [85].

Note, figure 3.3 has been constructed for two different values of  $\phi_0$ . Assuming that  $\sigma = 1/2$ , which is around the typical value for an experiment, implies that the left panel is for  $\eta_0 = 0.21$  and the right for  $\eta_0 = 1.14$ . This indicates that the models are in agreement for all the experiments Savage & Lun performed, as they never considered  $\eta$  greater than 0.15.

### 3.1.6 A velocity field that scales with the thickness to the power 3/2

As discussed in §1.2.1, there is considerable evidence that the mean velocity of chute flows scales with the thickness of the layer to the power 3/2. For this reason the velocity profile proposed by Silbert *et al.* [56], given by equation (1.10), will be investigated. Before continuing, this profile needs to be non-dimensionalised subject

to the scaling in (2.32) and recalling  $\bar{u}$  given by (1.12), reveals the dimensionless downslope velocity profile as

$$u = \frac{5}{3} \left[ 1 - (1 - z)^{3/2} \right]. \quad (3.31)$$

The integral transform (3.10) implies that the depth integrated velocity coordinate is

$$\psi = \frac{5}{3}z - \frac{2}{3} \left[ 1 - (1 - z)^{5/2} \right]. \quad (3.32)$$

This transformation can not be inverted to give explicit relations for the shocks, but it is a simple procedure to produce contour plots of the results, which are shown in the bottom two panels of figure 3.2. They look quite similar to the case of simple shear as the bottom shock has an infinite gradient at the origin, but the third shock is not as high. This minor discrepancy between the two profiles would be very hard to see experimentally, and the linear shearing profile remains a very good approximation to this more complicated profile.

### 3.1.7 Particle paths

To understand these solutions, it is instructive to explore the trajectories of the large and small particles moving through the flow. The idea and detailed explanation of particle paths can be found in many standard textbooks, for example §1.8 of [88].

The particle-paths of constituent  $\mu$  are obtained by solving

$$\frac{dx^\mu}{dt} = u^\mu, \quad \frac{dy^\mu}{dt} = v^\mu, \quad \frac{dz^\mu}{dt} = w^\mu, \quad \mu = l, s. \quad (3.33)$$

For this model the individual constituent velocities are given by (2.18) and (2.23), with the bulk velocity under consideration in this section, i.e (3.1), (3.33) is reduced to the following,

$$\frac{dx^s}{dt} = u(z), \quad \frac{dz^s}{dt} = S_r(1 - \phi), \quad \frac{dx^l}{dt} = u(z), \quad \frac{dz^l}{dt} = -S_r\phi, \quad (3.34)$$

which has been written in terms of non-dimensional variables, using (2.32).

Eliminating time, to obtain the particle paths, and changing to the depth integrated coordinates, using (3.11), gives the particles paths as

$$\frac{d\psi^s}{dx^s} = -S_r(1 - \phi) \quad \text{and} \quad \frac{d\psi^l}{dx^l} = S_r\phi. \quad (3.35)$$

The particles will enter the chute at  $x = 0$  at a height  $z_0$  where, for both large and small particles,  $0 \leq z_0 \leq 1$ . Initially the particles find themselves in a region of concentration  $\phi_0$ . Integrating (3.35) gives the paths as

$$\psi^s = -S_r(1 - \phi_0)x^s + \psi_0, \quad \psi^l = S_r\phi_0x^l + \psi_0, \quad (3.36)$$

where  $\psi_0 = \int_0^{z_0} u(z') dz'$ . For the series of linear velocities (3.24) under consideration,

$$\psi_0 = \alpha z_0 + (1 - \alpha) z_0^2. \quad (3.37)$$

The small particles will continue along this trajectory until they cross the lower shock, given by (3.21), which occurs at the point

$$x = \frac{\psi_0}{S_r}, \quad \psi = \psi_0\phi_0. \quad (3.38)$$

Whereas, the large particles will head upward until crossing the shock emanating from the top corner of the inflow, (3.23), occurring at

$$x = \frac{1 - \psi_0}{S_r}, \quad \psi = \phi_0 + \psi_0 - \psi_0\phi_0. \quad (3.39)$$

After the large/small particles cross the top/bottom shock they find themselves in a region filled of there own type and (3.36) implies the trajectories then become parallel to the base of the flow.

The particle paths are illustrated in figure 3.4. The homogeneous mixed region is immediately obvious, in this region the small particles can be seen to percolate down as the large particles are levered up toward the free surface. In both the simple shear and the plug flow case, shock 2 (top) is also given by the particle path of the small particle started at the point  $z = 0$ , likewise shock 1 (bottom) is the trajectory of a large particle starting at the very bottom of the chute, as is expected from the physical explanation of the shocks in §3.1.4

As discussed previously, there is the same flux of material above and below shock 3 (the segregation shock) even in the shear case. This is neatly illustrated by figure 3.4 as the flux is simply related to the number of particle paths and the same number of particles can be seen above and below this shock in both cases.

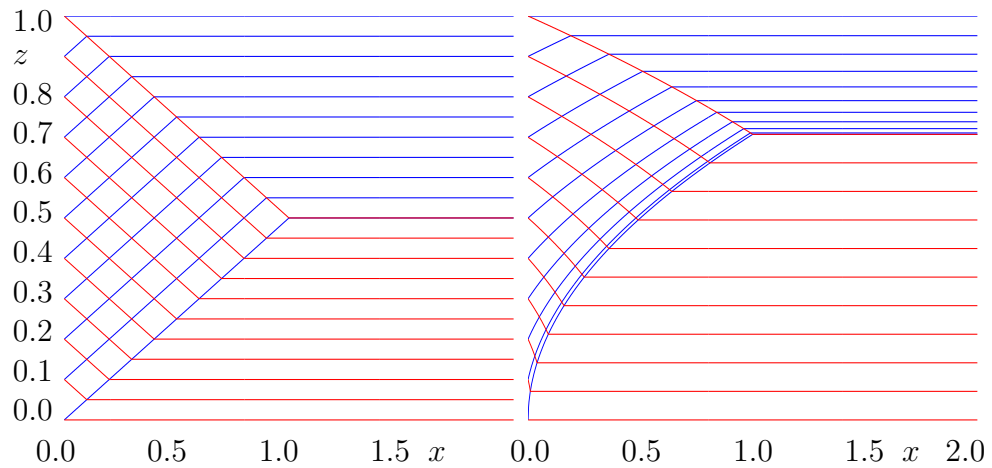


Figure 3.4: Graph showing the particle paths for large (blue) and small (red) particles starting from an homogeneous inflow condition. The flow is from left to right and the plots are constructed for  $S_r = 1$ . A path is drawn for 11 particles, of each type, whose initial height ranges from 0 to 1 in steps of 0.1. The left panel is for plug flow ( $\alpha = 1$ ) and the right for simple shear ( $\alpha = 0$ ).

## 3.2 Steady-state segregation in steady uniform flow with normally graded inflow conditions

The exact solutions for the segregation from a homogeneously mixed inflow were motivated by the experiments and approximate solutions of [72]. In practice, it is quite difficult to generate a homogeneous inflow, as the material tends to segregate in transport and setup. Such segregation can be seen in the original videos they recorded. This is a minor effect but can be avoided by using an alternative inflow configuration in which the particles are normally graded, i.e. with the small particles on top of the large particles. Analytical solutions for such a case are now considered.

### 3.2.1 General solution for arbitrary positive velocity fields

The same velocity, as in previous section (3.1), will be considered. As before, this velocity profile reduces the segregation equation (2.33) to the form of (3.5), which in this case is subject to the normally graded inflow condition, with a pure phase of small particles lying above a pure phase of large particles, at  $x = 0$ . Mathematically

this is given by,

$$\phi(0, z) = \begin{cases} 1 & z_r \leq z \leq 1, \\ 0 & 0 \leq z < z_r, \end{cases} \quad (3.40)$$

where  $z_r$  is the height of the sharp interface. In addition, as before, no particles are allowed to pass through the free-surface or base of the flow, which implies that (3.4) must be applied at both  $z = 0, h$ .

The same depth integrated transform, (3.10), will be used. Hence, following the analysis in §3.1.1, the characteristics are again given by

$$\psi = S_r (2\phi_\lambda - 1) (x - x_\lambda) + \psi_\lambda. \quad (3.41)$$

Before continuing, the initial condition (3.40) needs to be transformed into the depth integrated coordinates (3.10). In this coordinate system it becomes

$$\phi(0, \psi) = \begin{cases} 1 & \psi_r \leq \psi \leq 1, \\ 0 & 0 \leq \psi < \psi_r, \end{cases} \quad (3.42)$$

where

$$\psi_r = \int_0^{z_r} u(z') dz'. \quad (3.43)$$

Figure 3.5 illustrates how the characteristics propagate downstream from the inflow at  $x = 0$ . Above the discontinuity, the particles are all small and the characteristics propagate upwards with gradient  $S_r$ , whilst below the discontinuity, where the particles are all large, the characteristics propagate downwards with gradient  $-S_r$ . These characteristics are consistent with the no flux boundary conditions (3.4), therefore no shocks are generated when these intersect the top/bottom boundaries.

At the point  $x = 0, \psi = \psi_r = \psi(z_r)$  all values of  $\phi_\lambda$  are present from 0 to 1, therefore a rarefaction fan is formed from this point. The equation of this fan is simply obtained by substituting in the value of the emanation point,  $(0, \phi_r)$ , in to the general characteristic equation (3.41). After rearranging this gives,

$$\phi_\lambda = \frac{1}{2} \left( 1 + \frac{\psi - \psi_r}{S_r x} \right). \quad (3.44)$$

The solution described by (3.44) is valid until the  $\phi_\lambda = 0$  characteristic emanating from the fan propagates down and reaches the base of the flow at  $x_b = \psi_r/S_r$ , and

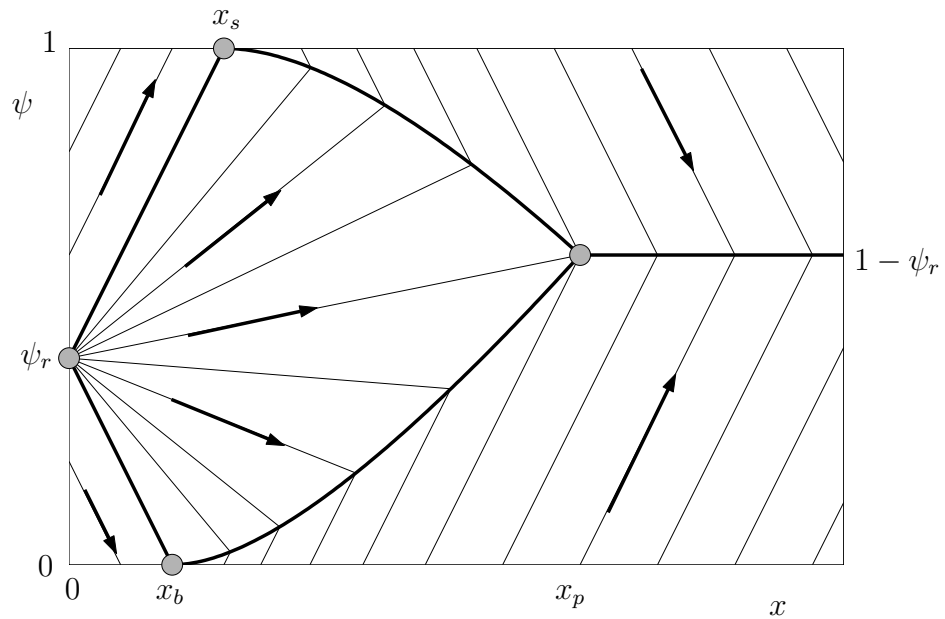


Figure 3.5: The steady-state solution in depth-integrated velocity coordinates  $(x, \psi)$  of the characteristics for the normally graded case. The inflow concentration jump is located at  $(0, \psi_r)$  and the bulk flow is from left to right. The characteristics are shown as straight thin lines and the arrows show their direction of propagation. A rarefaction fan is centred at the discontinuity and a series of characteristics radiate away from it. The front marking the first small particles that propagate downwards is indicated by the downward bold characteristic emanating from the fan. This reaches the base at a distance  $x_b = \psi_r/S_r$  downstream and a curved (bold) shock wave is generated that separates the expansion fan from the pure phase of small particles that gather beneath. A similar situation occurs at the top boundary, where the large particles first reach the surface at  $x_s = (1 - \psi_r)/S_r$  and a curved shock is generated that separates the pure phase of large particles from the expansion fan. At a distance  $x_p$  downstream the two shocks meet and a third parallel shock at height  $1 - \psi_r$  is formed, creating a completely segregated inversely graded layer.

generates a shock wave. Physically this characteristic represents the front between a region of purely large particles and the first small particles that propagate downwards. Within the avalanche a downward motion of small particles automatically implies that there is a corresponding upward flux of large particles by (2.23). However, at the lower boundary, there are no more large particles available and the flux condition (3.4) implies that the small particles separate out into a pure phase. This concentration shock then propagates upwards into the domain as more and more particles separate out.

In §3.1.2 the following shock condition was derived,

$$\frac{d\psi}{dx} = S_r (\phi^+ + \phi^- - 1), \quad (3.45)$$

in depth integrated coordinates. This condition remains valid for this situation. The shock  $\psi_1$ , that forms when the lead characteristic  $\phi_\lambda = 0$  reaches the base, has a pure phase of small particles on the forward side,  $\phi^+ = 1$ , and the expansion fan (3.44) on the rearward side. Substituting these into (3.45) implies

$$\frac{d\psi_1}{dx} = \frac{1}{2} \left( 1 + \frac{\psi_1 - \psi_r}{S_r x} \right), \quad (3.46)$$

which is a linear separable ODE and can be integrated subject to the initial condition that  $\psi_1 = 0$  at  $x = \psi_r/S_r$  to give the height of the bottom shock as

$$\psi_1 = \psi_r + S_r x - 2\sqrt{S_r \psi_r x}. \quad (3.47)$$

A similar situation develops on the upper side of the expansion fan. The  $\phi_\lambda = 1$  characteristic marks the front of large particles that propagate upwards into the pure phase of small particles entering from the inflow. This reaches the free-surface  $\psi = 1$  at  $x_s = (1 - \psi_r)/S_r$  and a shock  $\psi_2$  is formed between a pure phase of large particles on the forward side,  $\phi^+ = 0$  and the expansion region (3.44) on the rearward side. The shock condition (3.45) yields a linear ordinary differential equation which can be integrated to give

$$\psi_2 = \psi_r - S_r x + 2\sqrt{S_r(1 - \psi_r)x}. \quad (3.48)$$

The lower shock (3.47) increases in height with downstream distance  $x$ , whilst the upper shock decreases in height. The two shocks meet at

$$x_p = \frac{1}{S_r} (\sqrt{\psi_r} + \sqrt{1 - \psi_r})^2, \quad \psi_p = 1 - \psi_r, \quad (3.49)$$

and a third shock  $\psi_3$  is formed between the large and small particles. In this case the jump condition (3.45) reduces to  $d\psi/dx = 0$ , so that for this shock

$$\psi_3 = \psi_p, \quad \text{for } x \geq x_p, \quad (3.50)$$

and it is parallel to the downstream coordinate. The point  $x_p$  determines the downstream location at which complete segregation first occurs. It is proportional to  $1/S_r$ , which, like the solutions §3.1.4, show that inversely graded layers form at shorter downstream distances when the segregation number  $S_r$  is larger. The segregation distance also depends on  $\psi_r$ , which is qualitatively different to the homogeneous inflow case, where the distance for complete segregation was independent of the initial concentration. The transform (3.43) implies that  $x_p$  is dependent of both the initial segregation height  $z_r$  and the underlying velocity field  $u(z)$ . This means that comparison with experiments cannot be conducted unless detailed information on the velocity field is known.

The region above this final  $\psi_3$  shock is filled with large particles, which implies that  $\phi = 1$  on the top boundary after  $x_s$ . This clearly has to be the case as the characteristics represent the direction of information propagation from the boundary. As no information can cross the shock it must take a value such that the solution exists in this region. Therefore the point  $x_s$  represents the location where the boundary solution switches from  $\phi = 0$  to  $\phi = 1$ . As already discussed, physically this represents the arrival of the first large particles at the top boundary and the formation of a pure large phase. Mathematically, this switch is required so that a solution exists in the whole domain. Similar arguments can be constructed for the opposite switch in the value of  $\phi$  at the bottom boundary, occurring at the point  $x_b$ . Figure 3.5 shows the full diagram of the characteristics and how information from the boundary is propagated and fills the whole domain.

### 3.2.2 Physical solutions

In this section the physical solution for a number of different velocity fields, as in §3.1.4, will be investigated. Initially we will look at a series of linear velocity fields given by (3.24). As before, with this velocity profile, the mapping back into physical space is given by (3.26).

The physical solutions are illustrated for three values of  $\alpha$  and two values of  $z_r$  in the top six panels of figure 3.6, for  $S_r = 1$ . A contour scale is used to help identify regions of high concentrations of small particles (red) and large grains (blue). The top two panels correspond to plug flow where, in this case, the physical and depth-integrated coordinates are identical,  $\psi = z$ , so the fan is bounded by straight lines and the upper and lower curved concentration shocks have square-root dependence as defined in (3.47) and (3.48). The point  $x_p$  where the two shocks meet, and the grains separate out into stratified inversely graded layers, is dependent on the height of the inflow discontinuity  $z_r$ . Equation (3.49) implies  $x_p = 2$  for  $z_r = 1/2$ , whilst for  $z_r = 0.7$  the shocks meet slightly earlier at  $x_p = 1.91$ . The upper middle panels of figure 3.6 show the solutions for linear shear and translation with  $\alpha = 1/2$ , which requires the full quadratic mapping (3.25). The characteristics in the expansion fan are now curved, rather than straight. This is because as the small particles percolate down through the matrix their downslope velocity becomes progressively less, even though the percolation velocity at a given concentration remains constant by (2.23). As a consequence, the lower  $\phi_\lambda = 0$  characteristic emanating from the fan reaches the base of the avalanche slightly earlier than for plug flow, whilst the upper characteristic  $\phi_\lambda = 1$  reaches the free-surface slightly further downstream. The combination of the mapping and these shifts in the initiation point of the shocks results in the upper and lower shocks meeting at a far higher level in the avalanche, so that the layer of inversely graded large particles is much thinner for sheared flow than for plug-flow. Physically, the reason for this is that there is simply a far higher mass flux of particles in the upper rapidly moving layer of the flow. The segregation length  $x_p$ , where the two shocks meet, is in almost the same position for both  $z_r = 0.5$  and  $0.7$ . For simple

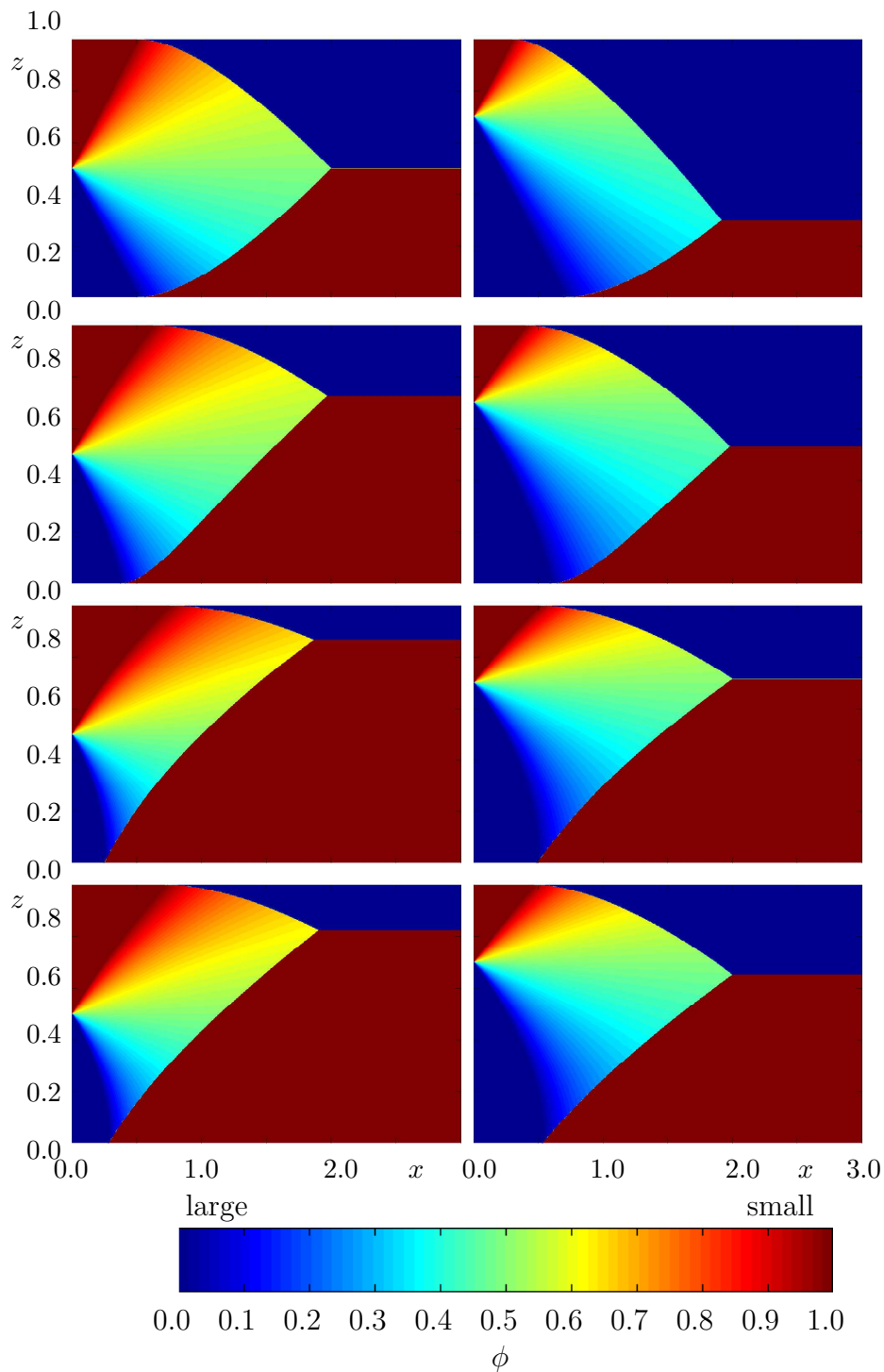


Figure 3.6: Steady-state solutions for the concentration of small particles  $\phi$  are shown as a function of the downslope coordinate  $x$  and avalanche depth  $z$ . The bulk flow is from left to right and the concentration is shown using a contour scale. A shade of blue corresponds to higher concentrations of large particles than small, and red vice versa. The bulk flow is from left to right and the top 3 sets of panels assume linear velocity profiles corresponding to plug flow ( $\alpha = 1$ ), linear shear with basal slip ( $\alpha = 1/2$ ) and simple shear ( $\alpha = 0$ ), from top to bottom respectively. The bottom two panels correspond to Silbert et al.'s velocity  $u = 5(1 - (1 - z)^{3/2})/3$ . The solution is plotted for  $z_r = 0.5$  (left) and  $z_r = 0.7$  (right)

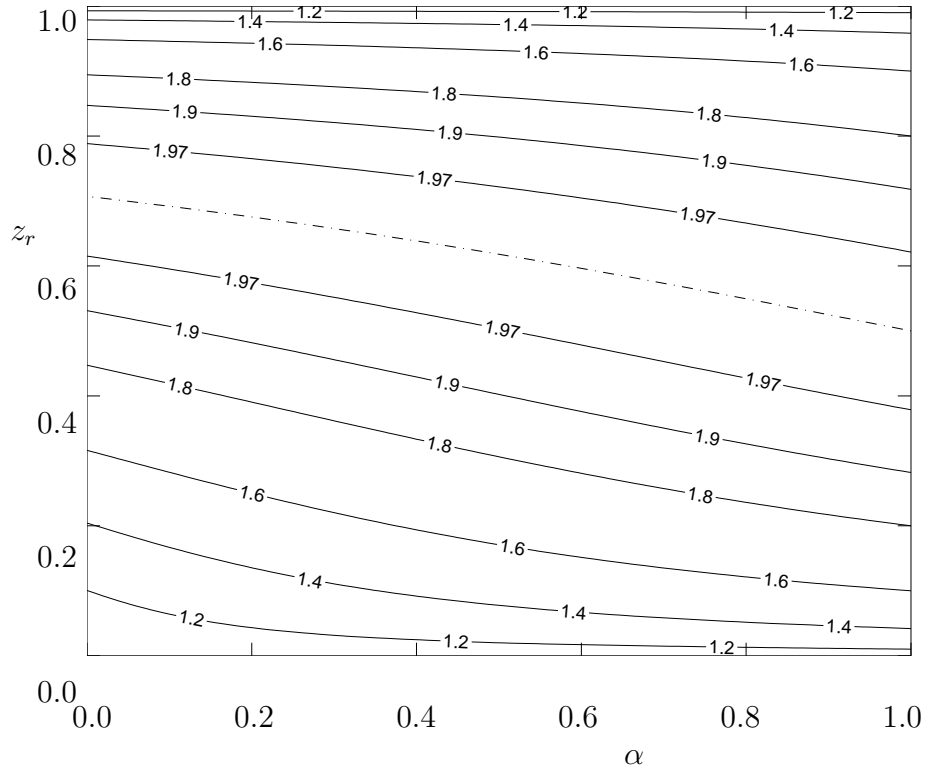


Figure 3.7: A contour plot of the segregation distance  $L_s = S_r x_p$  as a function of the linear velocity profile parameter  $\alpha$  and the initial discontinuity height  $z_r$ . The dot-dash line shows the points where the maximum value of  $L_s = 2$  is attained.

shear,  $\alpha = 0$ , the reverse mapping (3.26) reduces to  $z = \sqrt{x}$ . The lower characteristic, which marks the first small particles percolating downwards and emanates from the fan, has an infinite gradient at  $z = 0$ , which is caused by the zero velocity at the base of the avalanche. In addition, the lower shock now has a concave instead of convex profile and the layer of rapidly moving large particles far downstream is even thinner than for linear shear and translation. Interestingly, the segregation length is now longer for  $z_r = 0.7$  than for  $z_r = 0.5$ , with  $x_p = 1.99$  and  $x_p = 1.86$  respectively, reversing the order found in plug-flow.

It should be noted that the segregation strength parameter,  $S_r$  could be scaled out, for the situation under investigation. It has been left in to emphasise the effect of changing the strength has on the equation solution. To remove this effect

$$L_s = x_p S_r, \tag{3.51}$$

will be defined. Considering  $L_s$  will give information about the difference in segregation lengths of the same materials between different configurations. For all values of  $\alpha$  and different initial concentrations  $L_s = 1$  for the homogeneous inflow case. Therefore, this can be considered the ratio of the segregation length in homogeneous inflow case to any other configuration for a given set of two granular materials.

As pointed out above for this configuration, there is a complicated dependence of the segregation length  $x_p$  on both  $\alpha$  and  $z_r$ . To investigate this further we differentiate (3.49) with respects to  $\psi_r$ , this reveals

$$\frac{\partial x_p}{\partial \psi_r} = \frac{1}{S_r} \frac{(1 - 2\psi_r)}{\sqrt{\psi_r - \psi_r^2}} = 0. \quad (3.52)$$

The maximum segregation parameter  $L_s$  is equal to 2 and this is attained when  $\psi_r = 1/2$ , or, equivalently using (3.43), when  $\alpha = (1/2 - z_r^2)/(z_r - z_r^2)$ , as shown by the dot-dash line in figure 3.7. By expressing (3.49) as

$$S_r x_p = 1 + 2\sqrt{\psi_r - \psi_r^2}, \quad (3.53)$$

it is immediately clear that the lower limit of  $L_s$ , for this configuration, is 1 and is achieved in either limit of  $\psi_r \rightarrow 0, 1$ . This should be expected as in these limits you are approaching very thin initial layers of one or the other constituent, therefore, the inflow looks like a homogeneous inflow. Figure 3.7 demonstrates how the segregation parameter  $L_s = S_r x_p$  varies as a function of  $\alpha$  and  $z_r$ . This shows that the segregation distance is strongly dependent on  $z_r$  and only weakly dependent on  $\alpha$ .

Finally we investigate the Silbert *et al.*, [56], velocity profile. The transformation to physical space is given by (3.32). As discussed in §3.1.6 it is not possible to invert this for explicit relations for the shocks, but it is easy to numerically solve and to construct contour plots of this solution. These are illustrated by the bottom two panels of figure 3.6. Again, there is very little difference between this case and simple shear. The final shock is lower which is a representation of the lower net flux in the upper half of the flow with the Silbert *et al.* profile. Figure 3.8 shows the percentage error between the simple shear case ( $\alpha = 1$ ) and the Silbert profile. There is no difference between the case when  $z_r = 0, 0.7$  and 1 and it attains a maximum error

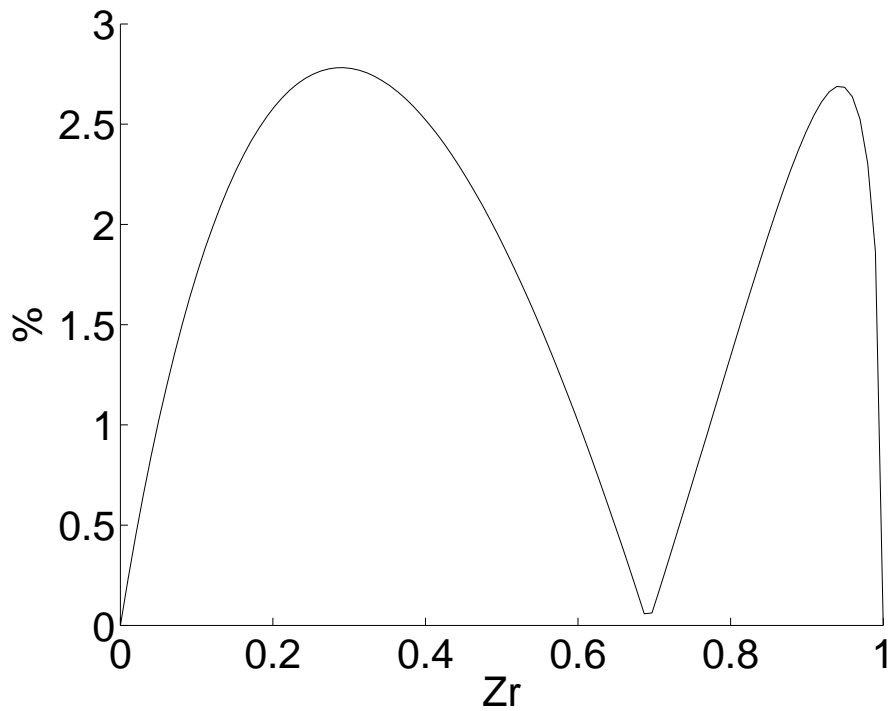


Figure 3.8: Graph showing the percentage difference, in segregation length, when using simple shear as an approximation to the Silbert profile against initial separation height  $z_r$ . The maximum in the estimation is 2.78 and occurs when  $z_r = 0.3$

of 2.78% at the point  $z_r = 0.3$ . This shows that for all values of  $z_r$ , simple shear is a good approximation and from this point onwards the Silbert *et al.* profile will no longer be considered.

### 3.2.3 Particle paths

As done previously the particle paths will be determined. Equation (3.35) remains valid for this configuration, but this time the values of  $z_0$  are restricted. For the large particles  $0 \leq z_0 \leq z_r$  and small particles  $z_r \leq z_0 \leq 1$ . As the particles are initially in a pure phase of their own type, they travel downstream at their initial height  $\psi_0$ , given by (3.37) for the linear velocity profiles. The particles move along until they intersect the expansion fan, inside  $\phi$  is given by (3.44), and the point of intersection  $x_e$  is given by

$$x_e^s = \frac{\psi_0 - \psi_r}{S_r}, \quad x_e^l = \frac{\psi_r - \psi_0}{S_r}. \quad (3.54)$$

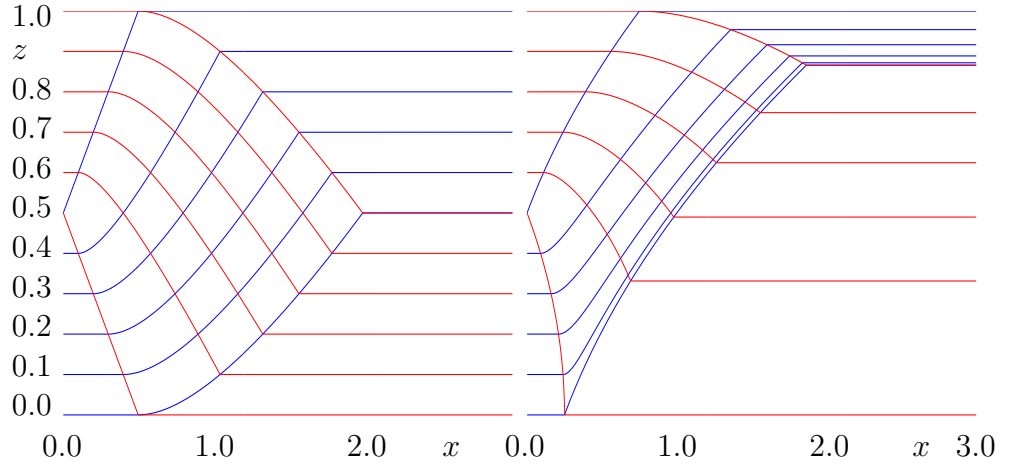


Figure 3.9: Graph showing the particle paths for large (blue) and small (red) particles starting from a normally graded inflow condition. The flow is from left to right and the plots are constructed for  $S_r = 1$  and  $z_r = 0.5$ . A path is drawn for 6 particles, of each type, whose initial height ranges from 0 to 0.5 in steps of 0.1 for large and 0.5 to 1 in steps of 0.1 for small. The left panel is for plug flow ( $\alpha = 1$ ) and the right for simple shear ( $\alpha = 0$ ).

Equation (3.36) is easily integrated subject to these conditions to give,

$$\psi^l = \psi_r + S_r x^l - 2\sqrt{S_r x_e^l} \sqrt{S_r x^l}, \quad \psi^s = \psi_r - S_r x^s + 2\sqrt{S_r x_e^s} \sqrt{S_r x^s}. \quad (3.55)$$

Since the second term grows quicker than the third, it is clear that within the fan the large particles are forced upwards and small particles percolate downwards. To conclude the particle-path analysis, the exit point from the fan needs to be computed. For large particles this occurs when they cross shock 1, whose equation is given by (3.47), solving (3.55) and (3.47) gives this exit point,  $x_x^l$  as

$$x_x^l = \left( \sqrt{1 - \psi_r} + \sqrt{S_r x_x^l} \right)^2 / S_r, \quad \psi_x^l = 1 - S_r x_e^l. \quad (3.56)$$

For the small particles this occurs on crossing shock 2, given by (3.48) and happens at the point

$$x_x^s = \left( \sqrt{\psi_r} + \sqrt{S_r x_x^s} \right) / S_r, \quad \psi_x^s = S_r x_e^s. \quad (3.57)$$

On exit from the fan, the particles again enter a pure phase of their own type and move downstream at a constant height  $\psi_x^l$ . The full particle-paths have now been determined and are illustrated in figure 3.9

For the plug-flow case consider a single large particle entering with initial height  $z_0 = 0.2$ , shown on figure 3.9. This particle moves along at height  $z_0$  until a small particle percolates past it, this is highlighted by the crossing of the first red particle path. Once it has passed this point small particles percolate passed, and it is levered upward passing more small particles. Eventually it crosses the small particle path emanating from the point  $z = 1$ , after this point it has passed all the small particles and is in a region of pure large particles, hence it is no longer pushed upwards and remains at this height for the rest of the length of the chute.

### 3.3 Time-dependent segregation in steady uniform plug-flows with homogeneous inflow conditions

Segregation by kinetic sieving is usually associated with flows that are strongly sheared through their depth. However, many geophysical scale ([20]) and laboratory scale ([70, 54]) avalanches have relatively blunt downstream velocity profiles with slip at the base. Segregation can still occur in these flows provided the particle size difference is large enough and the agitation strong enough for the matrix to dilate sufficiently for percolation to take place. Considerable insight into segregation in this weak shear limit is provided by the case of plug flow.

#### 3.3.1 Segregation in independent columns

For uniform plug-flow in a domain of unit height the segregation equation (2.25) reduces to

$$\frac{\partial \phi}{\partial t} + u_0 \frac{\partial \phi}{\partial x} - S_r \frac{\partial}{\partial z} (\phi(1 - \phi)) = 0, \quad (3.58)$$

where the transport velocity  $u_0$  can, without loss of generality, be assumed to be unity by virtue of the scalings in (2.32). As the velocity is independent of depth, considerable simplification can be achieved by transforming to a frame moving downstream with speed  $u_0 \equiv 1$  (from non-dimensionalisation). Using the change of coordinates

$$t' = t, \quad \xi = x - t, \quad z' = z, \quad (3.59)$$

the segregation equation (3.58) reduces to

$$\frac{\partial \phi}{\partial t} - S_r \frac{\partial}{\partial z} (\phi(1 - \phi)) = 0, \quad (3.60)$$

in the moving frame, where the primes are now dropped. Since, this equation is independent of  $\xi$  it implies that particle size segregation in a fixed moving column of granular material is completely independent of the segregation taking place in adjacent columns. This uncoupling is very useful for the construction of exact time-dependent solutions.

A comparison of (3.60) with (3.2) shows that the segregation problem in a moving column has exactly the same structure as the steady-state problem with  $u \equiv 1$ , except that the spatial coordinate is now replaced by time. The solutions constructed in §3.1 can therefore be applied directly here. To apply the solution from §3.1 the following identifications need to be made: Firstly since (3.60) is equivalent to (3.2) with  $u \equiv 1$  then the integral transform (3.10) simply implies that  $\psi = z$ . So the shock equation for this problem is simply

$$\frac{dz}{dt} = S_r (\phi^+ + \phi^- - 1). \quad (3.61)$$

If each of these independent homogeneous columns is assumed to be created at  $t = t_c$  with concentration  $\phi_c$ . It is clear that the shock solution (3.21)-(3.23) is valid with the changes  $x \rightarrow t - t_c$ ,  $\phi_0 \rightarrow \phi_c$  and  $\psi = z$ . Hence the solution of (3.58) is

$$\left. \begin{aligned} z_1 &= S_r \phi_c (t - t_c) && \text{in } 0 \leq t - t_c \leq 1/S_r, \\ z_2 &= 1 - S_r (1 - \phi_c) (t - t_c) && \text{in } 0 \leq t - t_c \leq 1/S_r, \\ z_3 &= \phi_c && \text{in } t - t_c > 1/S_r, \end{aligned} \right\} \quad (3.62)$$

which separate the homogeneous mixture and the pure phases in an exactly analogous manner to the problems in §3.1. These solutions are effectively illustrated in the top two panels of figure 3.2, the only difference is that the  $x$ -axis must now be replaced by the  $t - t_c$  axis.

### 3.3.2 General time-dependent solutions for plug-flow

A full time-dependent solution can be constructed for plug flow, by using the simple column solution (3.62) in a series of adjacent columns moving downstream at speed

$u_0 \equiv 1$ . The coordinate  $\xi$  will be used to uniquely identify each column, by labelling them using their initial position

$$\xi = x, \quad \text{at } t = 0. \quad (3.63)$$

It follows, from (3.59), that at a general time  $t$  column  $\xi$  has position

$$x = \xi + t. \quad (3.64)$$

Columns with positive  $\xi$  are therefore initially within the avalanche, whilst columns with negative  $\xi$  first enter the avalanche, at  $x = 0$ , at time  $-\xi$ . The *transition point*,  $\xi = 0$ , between the columns initially within the avalanche and those that subsequently enter it, is transported downstream with constant speed  $u_0 \equiv 1$  and has position

$$x_{\text{trans}} = t. \quad (3.65)$$

Since the columns are independent of one another, different values of the constants  $t_c$  and  $\phi_c$  can be chosen in each column, and they may therefore be considered to be functions of  $\xi$ . A single function  $\varphi$  is therefore used to parameterise both the initial and boundary conditions. Assuming that the homogeneous inflow concentration varies as  $\varphi(t)$ , and that the initial mixture has a uniform concentration equal to  $\varphi(0)$ , the column parameters  $t_c$  and  $\phi_c$  are

$$\begin{aligned} t_c = 0, \quad \phi_c = \varphi(0), \quad \text{for } \xi \geq 0, \\ t_c = -\xi, \quad \phi_c = \varphi(t_c), \quad \text{for } \xi < 0. \end{aligned} \quad (3.66)$$

Substituting these into the solutions (3.62) implies that the three shocks are simply time-dependent in the region that was initially in the chute

$$\left. \begin{aligned} z_4 = S_r \varphi(0)t & \quad \text{in } 0 \leq t \leq 1/S_r, \\ z_5 = 1 - S_r[1 - \varphi(0)]t & \quad \text{in } 0 \leq t \leq 1/S_r, \\ z_6 = \varphi(0) & \quad \text{in } t > 1/S_r, \end{aligned} \right\} \text{ and } x \geq t(= x_{\text{trans}}), \quad (3.67)$$

but have both space and time dependence in the region that flows into the chute

$$\left. \begin{aligned} z_1 = S_r \varphi(t-x)x & \quad \text{in } 0 \leq x \leq 1/S_r, \\ z_2 = 1 - S_r[1 - \varphi(t-x)]x & \quad \text{in } 0 \leq x \leq 1/S_r, \\ z_3 = \varphi(t-x) & \quad \text{in } x > 1/S_r, \end{aligned} \right\} \text{ and } x < t(= x_{\text{trans}}). \quad (3.68)$$

Note that in the above equations the round brackets  $()$  are being used to emphasize the functional dependence of  $\varphi$ , i.e. in (3.67)  $\varphi$  is a constant and in (3.68)  $\varphi$  is a function of  $\xi = t - x$ . The shock solutions (3.67)–(3.68) determine the general solution for the small particle concentration for any time-dependent function of the inflow concentration  $\varphi$ . The full solution, given by (3.67) and (3.68) has been shown to be made up, in general, of six shocks. The numbering system has been chosen such that it is consistent with all previous sections. It will be shown in this section that shocks 1 through to 3 tend towards the steady-state shocks of the homogeneous inflow (§3.1), for constant inflow problems. Whereas shocks 4–6 are transitional and are not found in the steady-state solution. Shock 4 emanates from the bottom boundary, 5 from the top and 6 is another segregation shock.

### 3.3.3 Solution for $\varphi = 0.5$

Three solutions for different function  $\varphi$  will be constructed to illustrate the use of the column solution. The first case to be considered will be,

$$\varphi = 1/2. \quad (3.69)$$

Physically this describes a chute which, at  $t = 0$ , is filled with homogeneously mixed material with  $\phi = 0.5$ . At the inflow the same material is fed in, the flow begins to move at  $t = 0$  and from that point is allowed to segregate. Substituting (3.69) into (3.67) and (3.68) reveals the solution to be given by,

$$\left. \begin{array}{l} z_4 = S_r t/2 \quad \text{in } 0 \leq t \leq 1/S_r, \\ z_5 = 1 - S_r t/2 \quad \text{in } 0 \leq t \leq 1/S_r, \\ z_6 = 1/2 \quad \text{in } t > 1/S_r, \end{array} \right\} \text{ and } x > t \quad (3.70)$$

$$\left. \begin{array}{l} z_1 = S_r x/2 \quad \text{in } 0 \leq x \leq 1/S_r, \\ z_2 = 1 - S_r x/2 \quad \text{in } 0 \leq x \leq 1/S_r, \\ z_3 = 1/2 \quad \text{in } x > 1/S_r, \end{array} \right\} \text{ and } x < t.$$

From here is clear the transition point, given by  $x_{\text{trans}} = t$ , marks the divide between the steady-state solution and the region of transient adjustment to the initial conditions and it propagates downstream with speed  $u_0 \equiv 1$ .

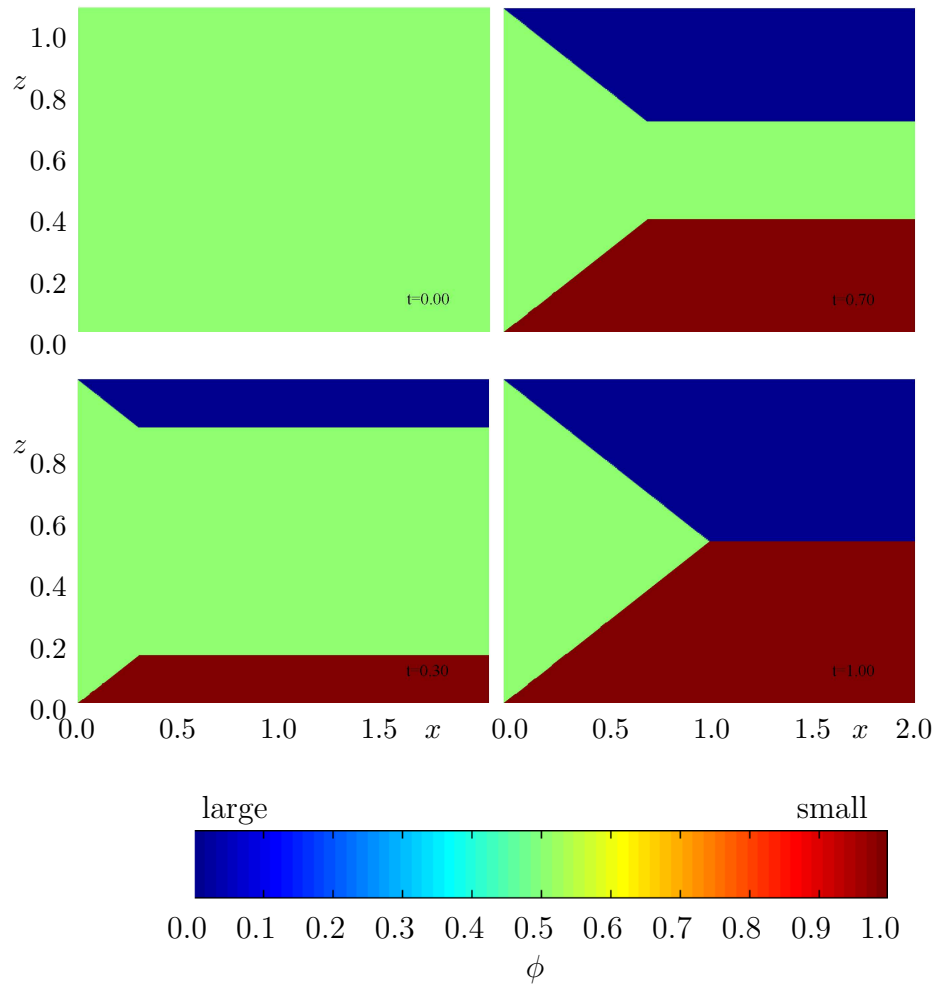


Figure 3.10: An exact solution for the time-dependent evolution of the small particle concentration  $\phi$  in a steady uniform plug-flow. The bulk flow is from left to right and the concentration is shown using a contour scale. A shade of blue corresponds to higher concentrations of large particles than small, and red vice versa. Whereas green indicates there is an equal amount of both by volume fraction. Initially the chute is filled with a homogeneous mixture of particles with a concentration of 50%. At the inflow a homogeneous mixture of particles, also with concentration 50%, enters the chute and flows downstream. The segregation number is taken as  $S_r = 1$  and plug velocity  $u_0 = 1$ , which implies that the particles fully segregate at  $x = 1$ . The steady-state is attained at  $t = 1$ .

Figure 3.10 shows contour plots of the solution of these six shocks for a series of time intervals and  $S_r = 1$ . Initially the chute is entirely filled with a homogeneous uniform mixture with a concentration of 50%. Immediately after the system is released the particles segregate in the interior, creating two spatially uniform shocks that separate the pure phases from the mixture. These two shocks eventually meet at  $t = 1$  to create a stationary third shock at  $z = 1/2$ , which separates the large particles from the small ones beneath. As this process is taking place, new material is fed into the chute and segregates, creating two additional straight shocks from the top and bottom corners of the inflow, these shocks meet at  $x = 1$ , which from (3.64) occurs at  $t = 1$ . From this it is clear that shocks 3 and 6 are created at the same time, shock 3 is created at  $(x, t) = (1, 1)$  and grows with time whereas shock 6 exists initially from  $x \in [1, \infty)$ , but its initiation point moves forward with time. It is clear that these shocks, 3 and 6, are two parts of the same physical shock and can be replaced with

$$z_3 = 0.5 \quad x > 1 \quad t > 1. \quad (3.71)$$

It is now apparent that after  $t = 1$  the solution is completely steady for the entire length of the semi-infinite chute. This steady-state solution is precisely the same as the one shown in the top left panel of figure 3.2, as expected.

### 3.3.4 Sinusoidally Oscillating Inflow Conditions

In physical experiments the material entering the avalanche is supplied from a hopper and once flow starts, inhomogeneities often develop, causing the inflow concentration to vary as a function of time. Exact solutions for the plug-flow regime can be constructed for this case, using the method above.

Suppose that the variation in the homogeneous inflow concentration is parameterized by

$$\varphi = 0.5 + 0.1 \sin(10t). \quad (3.72)$$

Substituting (3.72) into (3.67) and (3.68) shows that this time the six shocks, making

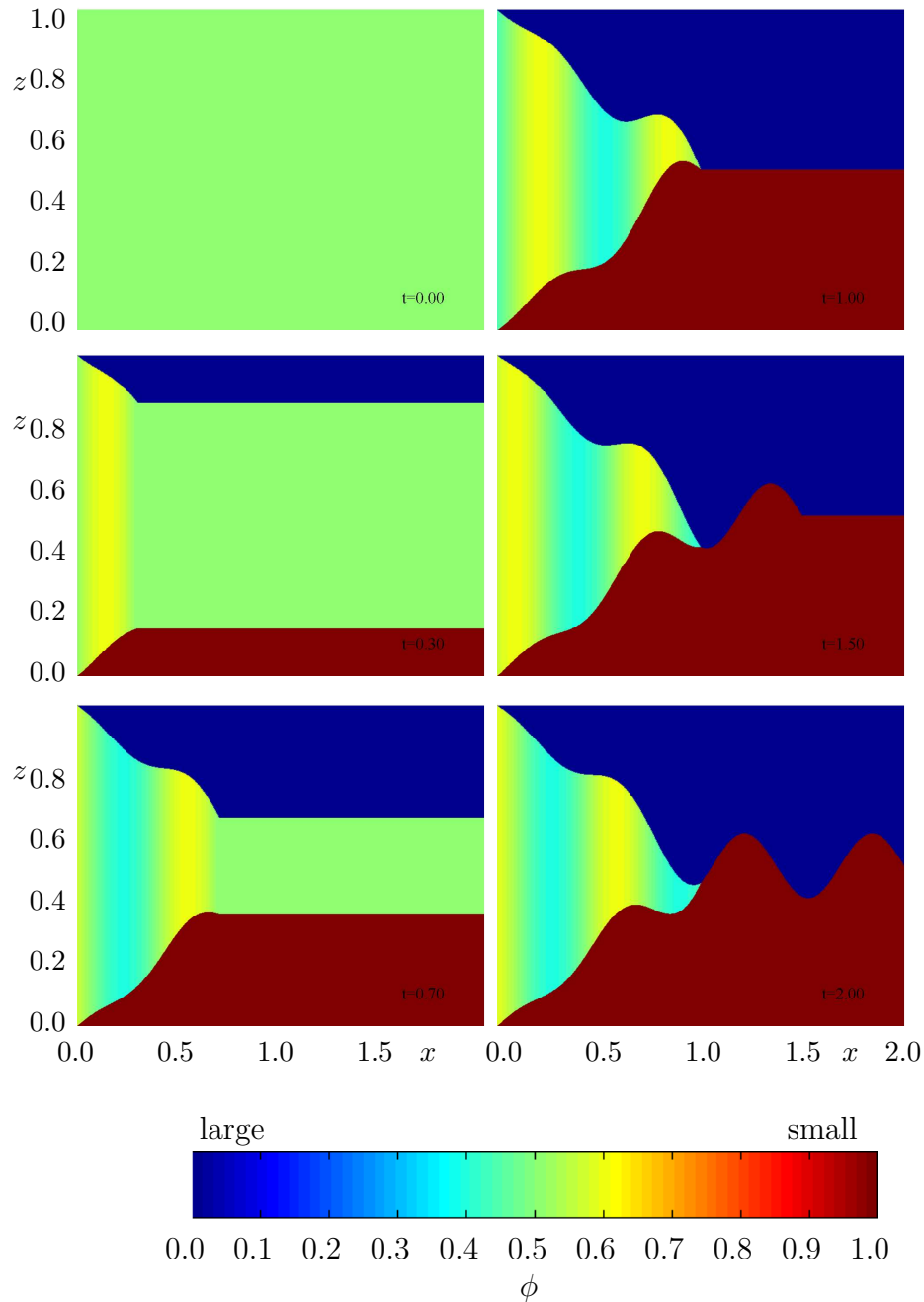


Figure 3.11: An exact solution for the time-dependent evolution of the small particle concentration  $\phi$  in a steady uniform plug-flow. The bulk flow is from left to right and the concentration is shown using a contour scale. A shade of blue correspond to higher concentrations of large particles than small, and red vice versa. Whereas green indicates there is an equal amount of both by volume fraction. Initially the chute is filled with a homogeneous mixture of particles with a concentration of 50%. The inflow concentration varies sinusoidally in time with amplitude 10% about a background concentration of 50%. The segregation number was taken to be  $S_r = 1$  and plug flow velocity, which implies that the particles fully segregate at  $x = 1$ .

up the solution, are given by

$$\left. \begin{aligned}
 z_4 &= S_r t/2 & \text{in } 0 \leq t \leq 1/S_r, \\
 z_5 &= 1 - S_r t/2 & \text{in } 0 \leq t \leq 1/S_r, \\
 z_6 &= 1/2 & \text{in } t > 1/S_r,
 \end{aligned} \right\} \text{ and } x > t$$

$$\left. \begin{aligned}
 z_1 &= S_r x [0.5 + 0.1 \sin(10(t-x))] & \text{in } 0 \leq x \leq 1/S_r, \\
 z_2 &= 1 - S_r [0.5 - 0.1 \sin(10(t-x))] & \text{in } 0 \leq x \leq 1/S_r, \\
 z_3 &= 0.5 + 0.1 \sin(10(t-x)) & \text{in } x > 1/S_r,
 \end{aligned} \right\} \text{ and } x < t.$$

(3.73)

This solution is illustrated, for  $S_r = 1$ , in figure 3.11 at a sequence of time intervals. The structure in front of the transition point is identical to that of the first problem, with two uniform shocks generated at the boundaries that propagate inwards and meet at  $(z, t) = (1/2, 1)$ , to leave a stationary shock. However, behind the transition, in the domain controlled by the boundary conditions, the sinusoidal variation propagates into the domain and distorts the shocks, which are fully time and space dependent. The shocks 1 and 2 oscillate 180 degrees out of phase and the third shock moves exactly in phase and with the same period as the inflow condition. At  $t = 1$  the two shocks meet at  $x = 1$  to form a triple point, which oscillates up and down with time. For  $t > 1$  the segregation shock becomes time-dependent in the region controlled by the boundary conditions and remains straight in the region determined by the initial conditions, as shown in the right middle panel of figure 3.11.

Such regular sinusoidal variations are unlikely to occur in an experiment setup, but this problem still gives insight into the effect of fluctuations of the feed condition. This problem will also produce an interesting test case for numerical algorithms that are constructed in §4, as there are three fully time and spatially dependent shocks for the method to resolve.

### 3.3.5 Piece-wise Continuous Solution

Since the solution (3.67) and (3.68) only depend on  $\varphi$  it is still valid for piecewise continuous data. With this in mind one final problem will be considered. The chute will initially be filled with a homogeneous mixture of concentration  $\phi = 0.25$  at time

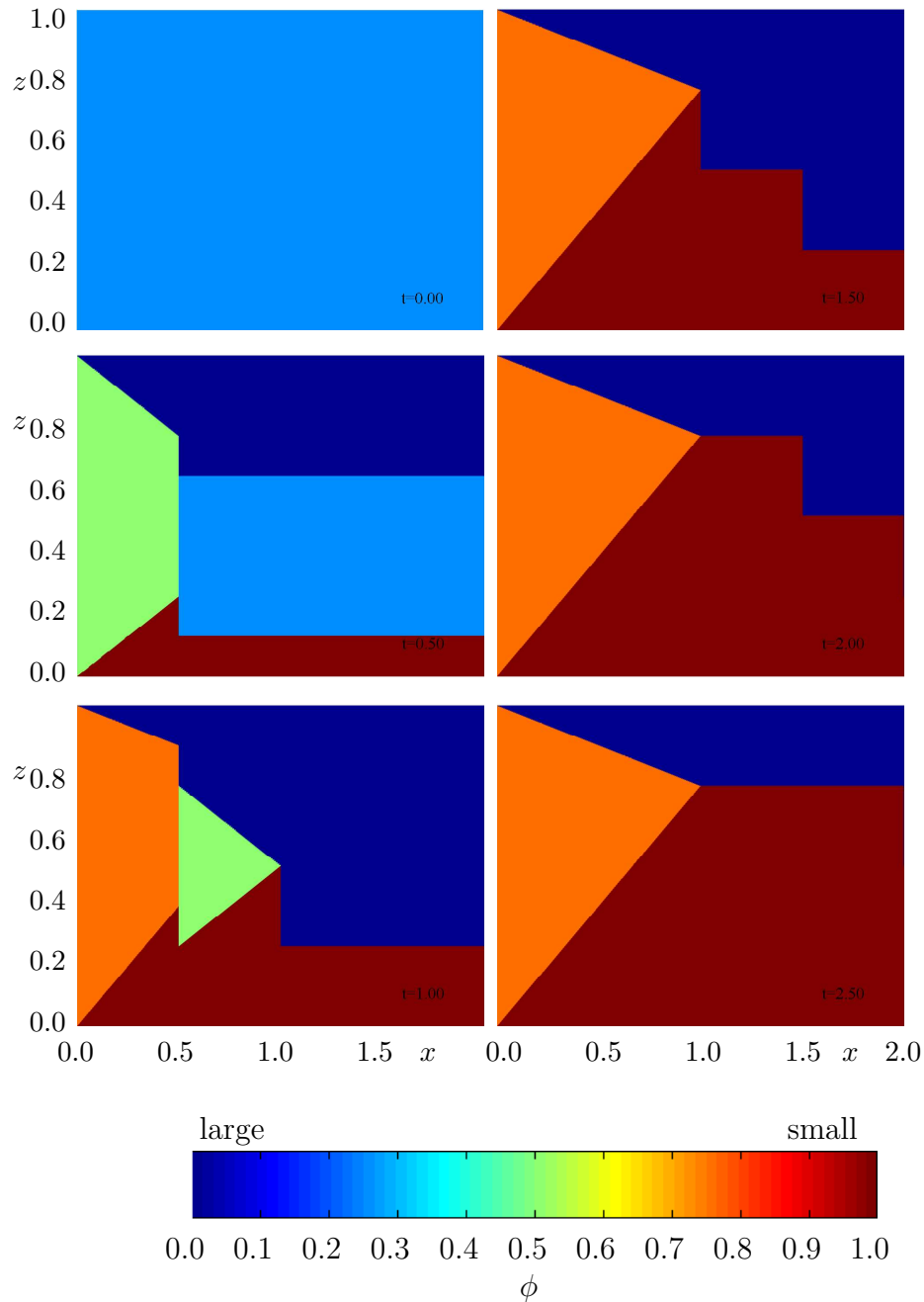


Figure 3.12: An exact solution for the time-dependent evolution of the small particle concentration  $\phi$  in a steady uniform plug-flow. The bulk flow is from left to right and the concentration is shown using a contour scale. A shade of blue corresponds to higher concentrations of large particles than small, and red vice versa. Whereas green indicates there is an equal amount of both by volume fraction. Initially the chute is filled with a homogeneous mixture of particles with a concentration of 25%. The inflow starts at a concentration of 50%, after  $t = 0.5$  this is steps up to 75%. The segregation number is  $S_r = 1$  and plug velocity, is used, which implies that the particles fully segregate at  $x = 1$ .

$t = 0$ , a concentration of  $\phi = 0.5$  will be fed into the domain and at  $t = 0.5$  this inflow concentration will be increased to  $\phi = 0.75$ . This implies

$$\varphi(t) = 0.25 + 0.25H(t) + 0.25H(t - 0.5), \quad (3.74)$$

where  $H(t)$  is the Heaviside step function and is defined as

$$H(t) = \begin{cases} 0 & t \leq 0 \\ 1 & t > 0 \end{cases}. \quad (3.75)$$

Substituting (3.74) into (3.67) and (3.68) reveals the solutions to be

$$\left. \begin{aligned} z_4 &= S_r t / 4 && \text{in } 0 \leq t \leq 1/S_r, \\ z_5 &= 1 - S_r 3t / 4 && \text{in } 0 \leq t \leq 1/S_r, \\ z_6 &= 1/2 && \text{in } t > 1/S_r, \end{aligned} \right\} \text{ and } x > t, \quad (3.76)$$

$$\left. \begin{aligned} z_1 &= S_r x [0.25 + 0.25H(t - x) + 0.25H(t - x - 1/2)] && \text{in } 0 \leq x \leq 1/S_r, \\ z_2 &= 1 - S_r [0.75 - 0.25H(t - x) - 0.25H(t - x - 1/2)] && \text{in } 0 \leq x \leq 1/S_r, \\ z_3 &= 0.25 + 0.25H(t - x) + 0.25H(t - x - 1/2) && \text{in } x > 1/S_r \end{aligned} \right\}$$

and  $x < t$ .

The solutions for  $S_r = 1$  are shown in figure 3.12. The first panel shows the initial chute filled with a 25% mixture of small particles. The middle left panel shows the situation at  $t = 0.5$ . The material that started in the chute has been advected along while segregating. A straight shock moving up with speed 0.25 is generated from the bottom boundary and from the top a straight shock moves down with speed 0.75. These two shocks meet at  $t = 1$  and produce a segregation shock from the point  $x = 1, z = 1/4$  and stretching to infinity. Behind these shocks the inflow conditions generate two shocks from the corners, which will meet at  $x = 1, z = 1/2$ . When these meet at  $t = 1$  a second segregation shock is generated, at the higher height of  $z = 1/2$ , this is then also advected downstream with the bulk flow. At  $t = 1/2$  the inflow conditions change, modifying the gradient of the shocks generated from the corners. At  $t = 1.5$  these new inflow conditions cause the segregation shock to jump again to the height of  $z = 3/4$ . After  $t = 1.5$  everything behind the point  $x = 1$  is steady and the segregation shock, with two jumps, continues to be advected with the

bulk flow. At  $t = 2.5$  the solution is steady for a chute of length of  $x = 2$  and the infinite chute problem never reaches a steady-state, but the solution becomes steady behind the point  $x = t - 0.5$  for  $t > 0.5$ .

This problem creates a very difficult test case for the numerical algorithms developed, as there are a lot of shocks with sharp gradients in its solution. A detailed analysis of how the numerics perform on this problem is considered in §4.

### 3.4 Time-dependent segregation in steady uniform plug flows from initially normally graded inflow conditions

In this section, as in the previous section, time-dependent plug flow solutions will be investigated, but this time subject to the inflow condition discussed in §3.2, i.e. (3.42). As before, the segregation equation (2.25) with the bulk velocity given by  $\mathbf{u} = (u_0, 0, 0)$  and under the transformation (3.59) is reduced to (3.60). Following the discussion in §3.3 the solution derived in §3.2 is valid with the following identifications

$$x \rightarrow t - t_c \quad , \quad \psi \rightarrow z \quad \text{and} \quad \psi_r \rightarrow z_c, \quad (3.77)$$

where  $t_c$  is the time and  $z_c$  is the initial height of separation for each of these independent columns. Therefore using (3.77) with the solution for normal graded inflow conditions (3.44), (3.47), (3.48) and (3.50) gives the independent column solution for this setup.

The concentration within the expansion fan is therefore

$$\phi = \frac{1}{2} \left( 1 + \frac{z - z_c}{S_r(t - t_c)} \right), \quad |z - z_c| < S_r(t - t_c), \quad z_1 < z < z_2, \quad (3.78)$$

where the shocks

$$\left. \begin{aligned} z_1 &= z_c + S_r(t - t_c) - 2\sqrt{S_r z_c(t - t_c)}, & (t - t_c) < t_p, \\ z_2 &= z_c - S_r(t - t_c) + 2\sqrt{S_r(1 - z_c)(t - t_c)}, & (t - t_c) < t_p, \\ z_3 &= 1 - z_c, & (t - t_c) \geq t_p, \end{aligned} \right\} \quad (3.79)$$

and the triple-point

$$t_p(z_c) = \frac{1}{S_r} (\sqrt{z_c} + \sqrt{1 - z_c})^2. \quad (3.80)$$

This time-dependent solution for the evolution of the concentration in a column of material moving downstream with speed  $u_0 \equiv 1$  is effectively illustrated in the top two panels of figure 3.6, except that the  $x$ -axis must now be replaced by the  $t - t_c$  axis.

As before, since the columns are independent, different values of  $z_c$  and  $t_c$  can be chosen for each. A single function  $\mathcal{Z}$  can be used to parameterise both the initial and boundary conditions. Assuming the chute is initially filled with small on top of large separated at a height of  $\mathcal{Z}(0)$  and the separation height at the inflow boundary varies as  $\mathcal{Z}(t)$ , then the column parameters are given by,

$$\begin{aligned} t_c = 0, \quad z_c = \mathcal{Z}(0), \quad \text{for } \xi \geq 0, \\ t_c = -\xi, \quad z_c = \mathcal{Z}(t_c), \quad \text{for } \xi < 0. \end{aligned} \quad (3.81)$$

Substitution of (3.81) into (3.79) gives the equation of the six shocks, which bound the solution,

$$\left. \begin{aligned} z_4 &= \mathcal{Z}(0) + S_r t - 2\sqrt{S_r \mathcal{Z}(0)t} \quad \text{in } 0 \leq t \leq t_p(\mathcal{Z}(0)), \\ z_5 &= \mathcal{Z}(0) - S_r t + 2\sqrt{S_r \mathcal{Z}(0)t} \quad \text{in } 0 \leq t \leq t_p(\mathcal{Z}(0)), \\ z_6 &= 1 - \mathcal{Z}(0), \quad \quad \quad \text{in } t > t_p(\mathcal{Z}(0)) \end{aligned} \right\} \quad \text{and } x > t, \\ \left. \begin{aligned} z_1 &= \mathcal{Z}(t-x) + S_r x - 2\sqrt{S_r x \mathcal{Z}(t-x)} \quad \text{in } 0 \leq x \leq t_p(\mathcal{Z}(t-x)), \\ z_2 &= \mathcal{Z}(t-x) - S_r x + 2\sqrt{S_r x \mathcal{Z}(t-x)} \quad \text{in } 0 \leq x \leq t_p(\mathcal{Z}(t-x)), \\ z_3 &= 1 - \mathcal{Z}(t-x), \quad \quad \quad \text{in } x > t_p(\mathcal{Z}(t-x)) \end{aligned} \right\} \quad (3.82)$$

and  $x < t$ ,

where the same numbering convention as the previous section has been adopted and

$$t_p(\mathcal{Z}) = \frac{1}{S_r} (\sqrt{\mathcal{Z}} + \sqrt{1 - \mathcal{Z}})^2. \quad (3.83)$$

Additional to these shocks, the solution contains two expansion fans, one in space

and the other in time. These are given by substituting (3.81) into (3.78), producing,

$$\begin{aligned} \phi_{e_t} &= \frac{1}{2} \left[ 1 + \frac{z - \mathcal{Z}(0)}{S_r t} \right] & z_4 < z < z_5, \quad |z - \mathcal{Z}(0)| < S_r t, \quad x > t, \\ \phi_{e_x} &= \frac{1}{2} \left[ 1 + \frac{z - \mathcal{Z}(t-x)}{S_r x} \right] & z_1 < z < z_2, \quad |z - \mathcal{Z}(t-x)| < S_r x, \quad x < t. \end{aligned} \quad (3.84)$$

The full solution for any  $\mathcal{Z}$  is described by (3.82),(3.83) and (3.84).

### 3.4.1 Solution $\mathcal{Z} = 0.5$

As for the previous case of homogeneous inflow, the solution will be investigated for several different functions of  $\mathcal{Z}$ . The first case which will be considered is

$$\mathcal{Z} = 0.5. \quad (3.85)$$

This corresponds to the chute initially being filled with small on top of large separated at a height by the line  $z = 0.5$ . At  $t = 0$  the material starts to move and the same configuration is fed in.

Substitution of (3.85) into (3.82),(3.83) and (3.84) shows the solution is composed of the following six shocks and two expansion fans,

$$\left. \begin{aligned} z_4 &= 1/2 + S_r t - 2\sqrt{1/2 S_r t} & \text{in } 0 \leq t \leq t_p, \\ z_5 &= 1/2 - S_r t + 2\sqrt{1/2 S_r t} & \text{in } 0 \leq t \leq t_p, \\ z_6 &= 1/2 & \text{in } t > t_p, \\ \phi_{e_t} &= \frac{1}{2} \left[ 1 + \frac{z - 1/2}{S_r t} \right] & \text{in } z_4 < z < z_5 \end{aligned} \right\} \text{and } x > t$$

$$\left. \begin{aligned} z_1 &= 1/2 + S_r x - 2\sqrt{1/2 S_r x} & \text{in } 0 \leq x \leq t_p, \\ z_2 &= 1/2 - S_r x + 2\sqrt{1/2 S_r x} & \text{in } 0 \leq x \leq t_p, \\ z_3 &= 1/2 & \text{in } x > t_p, \\ \phi_{e_x} &= \frac{1}{2} \left[ 1 + \frac{z - 1/2}{S_r x} \right] & \text{in } z_1 < z < z_2 \end{aligned} \right\} \text{and } x < t \quad (3.86)$$

where  $t_p = 2/S_r$ .

The solution generated by (3.86) is illustrated in figure 3.13. It consists of two parts. For  $\xi \geq 0$  a spatially uniform time-dependent expansion fan develops and shock

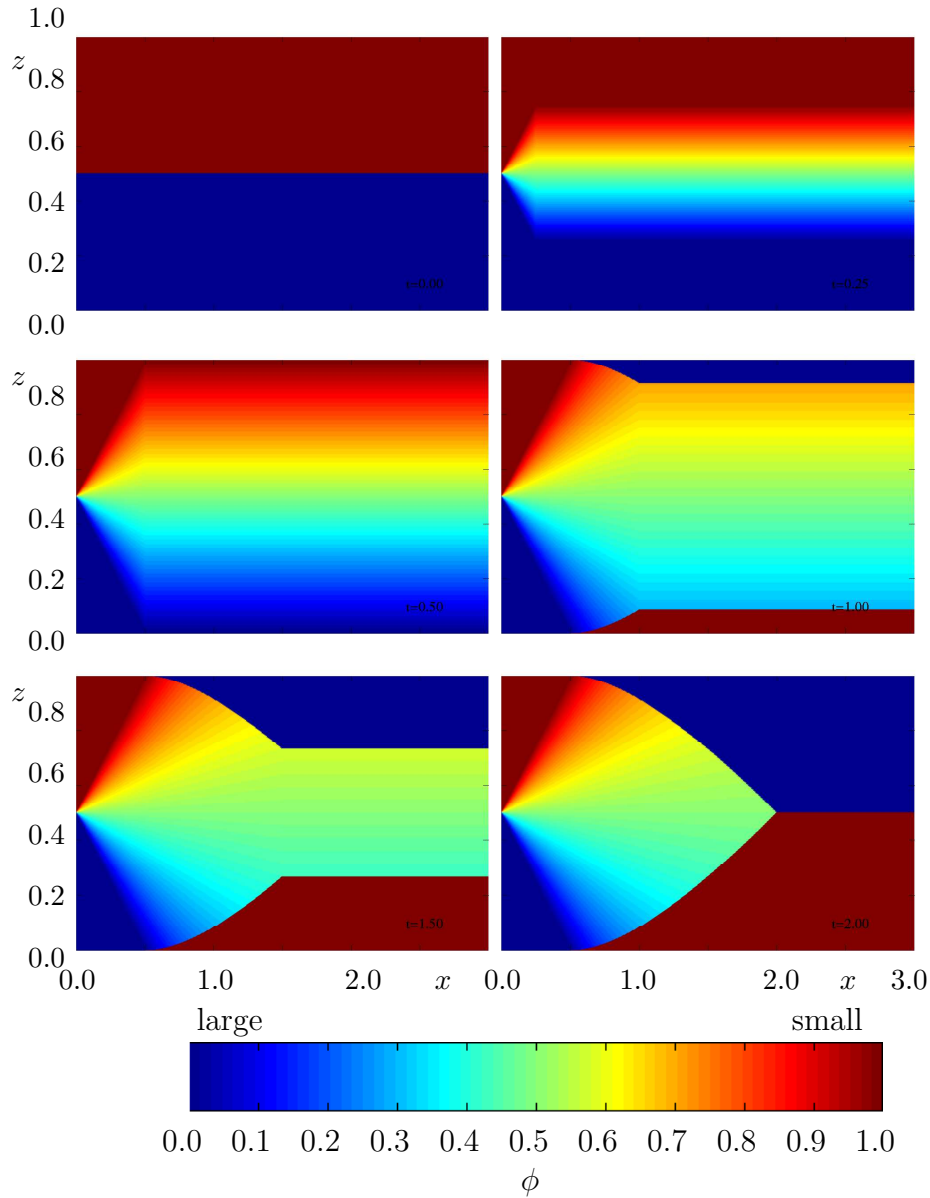


Figure 3.13: The exact plug-flow solution for the concentration of small particles  $\phi$  is illustrated at a sequence of time-steps using the same contour scale as in all other figures. Initially the flow is normally graded and normally graded material is fed in at  $x = 0$  and flows downstream from left to right. The solution consists of a time-dependent, spatially uniform part that is separated by a transition line moving downstream at speed  $u_0$  from a steady-state region behind. The parameter  $z_r = 1/2$  for all columns and the segregation number is  $S_r = 1$ .

waves are subsequently generated when the fronts reach the surface and base of the flow. These then propagate into the domain before they meet to form a spatially and temporally uniform third concentration shock separating an inversely graded layer of large particles from the fines beneath. Columns which enter the chute after  $t = 0$  are equivalent to a steady-state solution in a fixed frame of reference. A *transition line*  $\xi = 0$ , therefore moves downstream at speed 1 and separates the time-dependent solution from the steady-state solution behind. At time  $t = 2$  the upper and lower shocks meet in the time-dependent region to form an inversely-graded layer and there is no further change in the solution. In the plug-flow case the solution, therefore, attains a global steady-state in finite time.

### 3.4.2 Piece-wise continuous solution

In this section the solution to the problem of initially filling the chute with normally graded material separated at a height  $z = 0.25$ , with material separated at the higher height of  $z = 0.75$  fed in from the boundary will be investigated. This corresponds to

$$\mathcal{Z} = 0.25 + 0.5H(t), \quad (3.87)$$

where  $H$  is defined by (3.75). Substitution of (3.87) into (3.82),(3.83) and (3.84) gives the full solutions as

$$\left. \begin{aligned} z_4 &= 1/4 + S_r t - \sqrt{S_r t} && \text{in } 0 \leq t \leq t_p, \\ z_5 &= 1/4 - S_r t + \sqrt{S_r t} && \text{in } 0 \leq t \leq t_p, \\ z_6 &= 3/4 && \text{in } t > t_p, \\ \phi_{e_t} &= \frac{1}{2} \left[ 1 + \frac{z - 1/4}{S_r t} \right] && \text{in } z_4 < z < z_5 \end{aligned} \right\} \text{and } x > t$$

$$\left. \begin{aligned} z_1 &= 3/4 + S_r x - \sqrt{3S_r x} && \text{in } 0 \leq x \leq t_p, \\ z_2 &= 3/4 - S_r x + 2\sqrt{S_r x} && \text{in } 0 \leq x \leq t_p, \\ z_3 &= 3/4 && \text{in } x > t_p, \\ \phi_{e_x} &= \frac{1}{2} \left[ 1 + \frac{z - 3/4}{S_r x} \right] && \text{in } z_1 < z < z_2 \end{aligned} \right\} \text{and } x < t$$

where  $t_p = \frac{1}{S_r} \left( \frac{1}{2} + \frac{\sqrt{3}}{2} \right)^2 \approx 1.866$ .

(3.88)

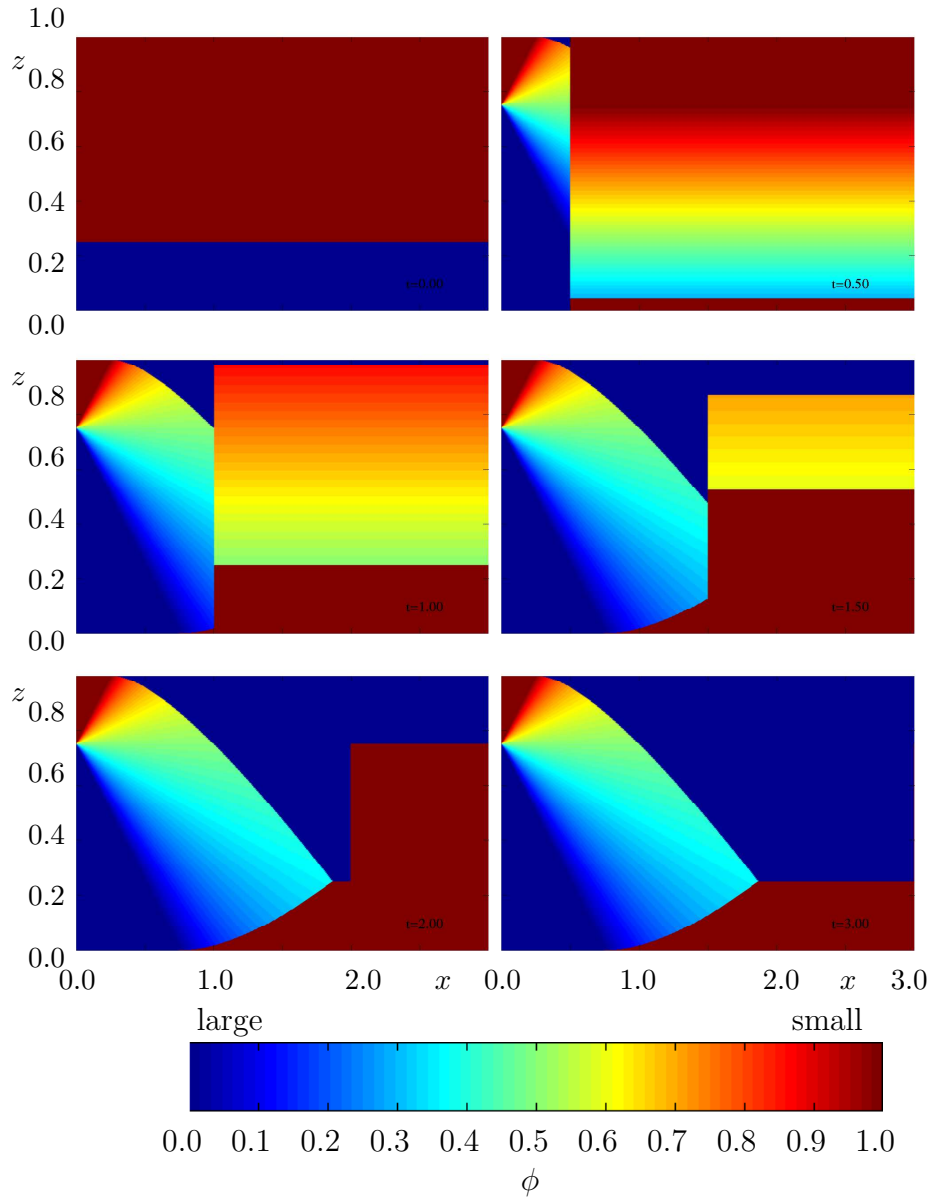


Figure 3.14: The exact plug-flow solution for the concentration of small particles  $\phi$  is illustrated at a sequence of time-steps using the same contour scale as in all other figures. Initially the flow is normally graded with  $z_r = 0.25$  and normally graded material is fed in at  $x = 0$ , at a time dependent height given by  $z_r = 0.75$ . The flow is from left to right. The solution consists of a time-dependent, spatially uniform part that is separated by a transition line moving downstream at speed 1 from a boundary controlled solution behind. The parameter  $S_r = 1$  is used.

This takes on such a simple form, since for  $x < t$ ,  $t - x > 0$ , hence  $\mathcal{Z}(t - x) = 3/4$  in (3.83). Due to the fact  $t_p(\mathcal{Z}) = t_p(1 - \mathcal{Z})$  the transition point is in the same place for both the steady and time dependent expansion fans. This is clearly shown by figure 3.14. Behind the transition point a spatial expansion point is mapped out that has  $z_r = 0.75$  and in front a temporal expansion fan with  $z_r = 0.25$  evolves. Since  $t_p = 1.866$  is the same for both of these fans, at the same time, the spatial fan becomes fully developed and the temporal fan is destroyed, as shown by the bottom left panel. After this point a segregation shock with a jump location at  $x = t$  is formed and is advected downstream with the bulk velocity. This is the final quasi-steady state of the solution and a finite length  $L$  steady-state will be achieved at  $t = L$ .

The solution to this problem is not very physical but it will again create an interesting and tricky test problem for the numerical algorithms.

### 3.4.3 Solution for $\mathcal{Z} = 0.5 + 0.1 \sin(10t)$

The final problem which will be investigated is the effect of a small perturbation to the inflow condition, hence

$$\mathcal{Z} = 0.5 + 0.1 \sin(10t). \quad (3.89)$$

Physically, this corresponds to the chute initially filled with normally graded material segregated by the line  $z = 0.5$ . At  $t = 0$  this material is allowed to flow and segregate, while normally graded material is fed in from the boundary with a point of segregation that varies with dimensionless amplitude 0.1 and frequency  $10/2\pi$ .

Substitution of (3.88) in the general solution gives

$$\left. \begin{aligned} z_4 &= 1/2 + S_r t - \sqrt{2S_r t} & \text{in } 0 \leq t \leq 2/S_r, \\ z_5 &= 1/2 - S_r t + \sqrt{2S_r t} & \text{in } 0 \leq t \leq 2/S_r, \\ z_6 &= 1/2, & \text{in } t > 2/S_r \\ \phi_{et} &= \frac{1}{2} \left[ 1 + \frac{z - 1/2}{S_r t} \right] & \text{in } z_4 < z < z_5 \end{aligned} \right\} \text{and } x > t, \quad (3.90)$$

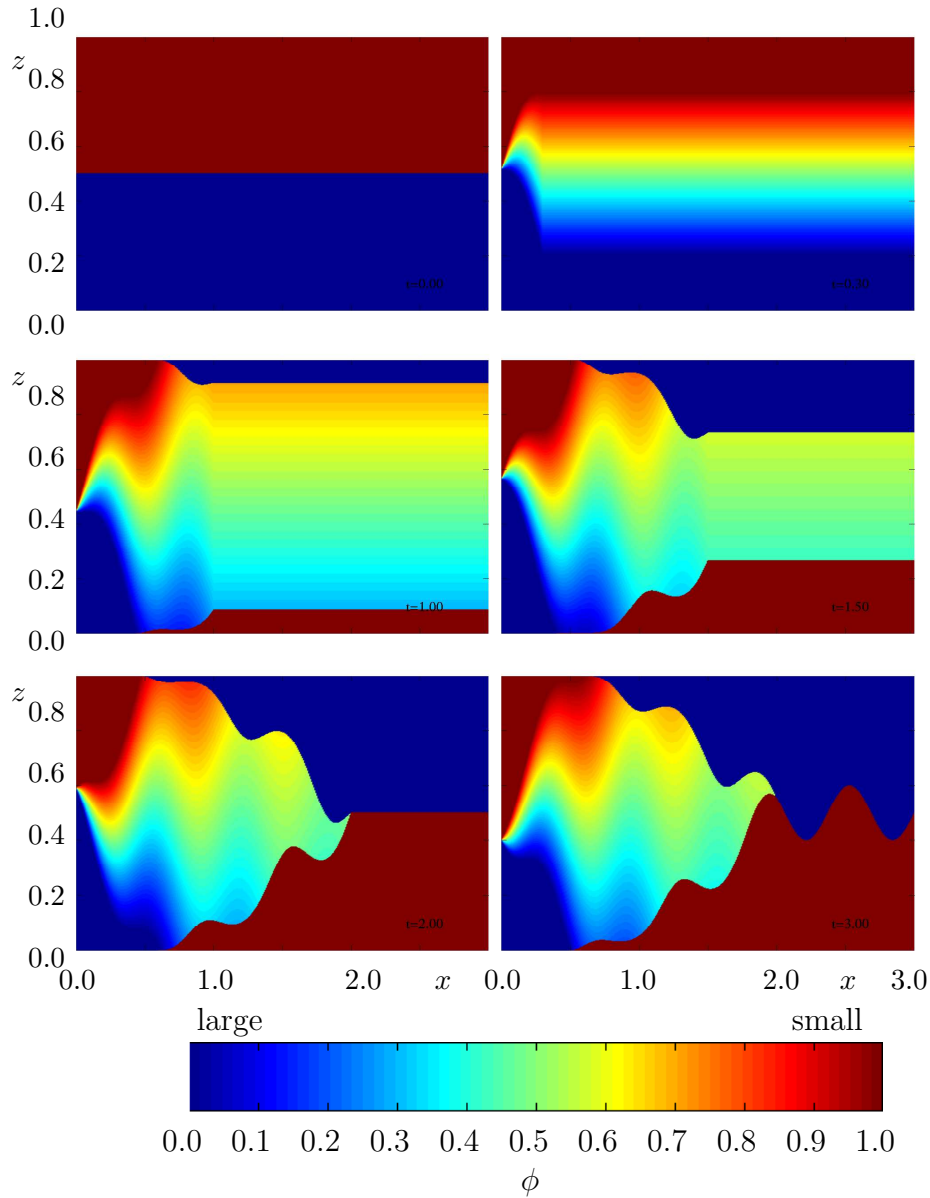


Figure 3.15: The exact plug-flow solution for the concentration of small particles  $\phi$  is illustrated at a sequence of time-steps using the same contour scale as in all other figures. Initially the flow is normally graded with  $z_r = 0.5$  and normally graded material is fed in at  $x = 0$  at a time dependent height given by  $z_r = 0.5 + 0.1 \sin(10t)$ . The flow is from left to right. The solution consists of a time-dependent spatially uniform part that is separated by a transition line moving downstream at speed 1 from a boundary controlled solution behind. The parameter  $S_r = 1$  is used.

$$\left. \begin{aligned}
 z_1 &= 1/2 + 1/10 \sin(10(t-x)) + S_r x \\
 &\quad - 2\sqrt{S_r x (1/2 + 1/10 \sin(10(t-x)))} \quad \text{in } 0 \leq x \leq t_p(t-x), \\
 z_2 &= 1/2 - 1/10 \sin(10(t-x)) - S_r x \\
 &\quad + 2\sqrt{S_r x (1/2 + 1/10 \sin(10(t-x)))} \quad \text{in } 0 \leq x \leq t_p(t-x), \\
 z_3 &= 1/2 - 1/10 \sin(10(t-x)) \quad \text{in } x > t_p(t-x), \\
 \phi_{e_x} &= \frac{1}{2} \left[ 1 + \frac{z - 1/2 - 1/10 \sin(10(t-x))}{S_r x} \right] \quad \text{in } z_1 < z < z_2
 \end{aligned} \right\} \quad (3.91)$$

and  $x < t$ ,

where

$$\begin{aligned}
 t_p(t-x) &= \frac{1}{S_r} \left( \sqrt{1/2 + 1/10 \sin(10(t-x))} \right. \\
 &\quad \left. + \sqrt{1/2 - 1/10 \sin(10(t-x))} \right)^2.
 \end{aligned} \quad (3.92)$$

Figure 3.15 clearly shows the effect of this perturbation, which is advected through the flow and causes all the shocks and the solution within the fan to oscillate about the unperturbed mean with the same frequency. The triple point moves backwards and forwards in a complicated manner but again its mean location is given by  $t_p(0.5)$ . The resulting segregating shock oscillates with the same frequency of the perturbation but 180 degrees out of phase. Once a numerical algorithm has been constructed, the effect of shear on this problem will be investigated.

# Chapter 4

## Numerical solutions

In this section a series of shock-capturing numerical algorithms will be discussed. These will be used to obtain numerical solutions of the segregation equation (2.35). The analytical solutions constructed in §3 will be used as a test bed to determine the accuracy and validity of the methods employed for these types of problems. This method will then be used to look at more interesting and physically realistic problems.

### 4.1 Shock-capturing numerical methods for first order hyperbolic equations

Due to the large numbers of shocks apparent in the analytic solution, the use of *shock-capturing* rather than shock-tracking methods seems to be appropriate. The former have the advantage over *shock-tracking* methods in that they automatically deal with discontinuities, hence, no pre-knowledge of their location is required. In the solutions of the segregation equation, (2.35), lots of shocks are apparent and interact in a complicated way requiring highly sophisticated shock-tracking routines. Therefore, attention will be restricted to shock-capturing methods.

For this analysis finite volume method will be considered. Here, the domain is broken down into grid cells and approximate numerical fluxes of material across the grid boundaries are computed. These have the advantage over more traditional finite difference methods, in that they do not break down when the solution contains

discontinuities. There are many papers on the topic of shock-capturing finite volume methods. These methods have a long history starting with the classic papers of Godunov [32], Van Leer [86], Harten [43] and Yee [90], and there are now a wide range of textbooks on these powerful schemes e.g. [57, 31, 81]. Reference [57] gives a very detailed and invaluable description of all issues that arise with finite volume methods including how to apply different types of boundary conditions and extending one-dimensional methods to multiple dimensions. In this section an effort is made to reference the original papers where the work was first presented.

Initially, the following one-dimensional equation will be considered

$$\frac{\partial \omega}{\partial t} + a(\omega) \frac{\partial \omega}{\partial x} = 0, \quad (4.1)$$

where  $a(\omega)$  is the characteristic speed, which is dependent on the variable  $\omega$ . Writing this equation in flux form gives

$$\frac{\partial \omega}{\partial t} + \frac{\partial f(\omega)}{\partial x} = 0, \quad (4.2)$$

where  $a$  and  $f$  are connected by the relation,

$$a(\omega) = \frac{\partial f(\omega)}{\partial \omega}. \quad (4.3)$$

Physically,  $f$  represents the flux of the variable  $\omega$  in the  $x$  direction. Considering (4.3) integrated over the region  $[x_{j-\frac{1}{2}}, x_{j+\frac{1}{2}}] \times [t^n, t^{n+1}]$  gives

$$\int_{x_{j-\frac{1}{2}}}^{x_{j+\frac{1}{2}}} \int_{t^n}^{t^{n+1}} \left\{ \frac{\partial \omega}{\partial t} + \frac{\partial f}{\partial x} \right\} dt dx = 0. \quad (4.4)$$

The general form of Green's theorem states

$$\iint_R \left( \frac{\partial Q}{\partial y} - \frac{\partial P}{\partial z} \right) dy dz = \int_C (Q dz + P dy), \quad (4.5)$$

where  $C$  is the boundary of the region  $R$ . Applying this to equation (4.4) with the identifications  $Q \rightarrow \omega$ ,  $P \rightarrow -f$ ,  $y \rightarrow t$  and  $z \rightarrow x$  gives the following result

$$\int_C (\omega dx - f dt) = 0, \quad (4.6)$$

where  $C$  is the contour surrounding the region. Equation (4.6) is easily re-arranged to give

$$\int_{x_{j-\frac{1}{2}}}^{x_{j+\frac{1}{2}}} \omega(x, t^{n+1}) dx = \int_{x_{j-\frac{1}{2}}}^{x_{j+\frac{1}{2}}} \omega(x, t^n) dx - \int_{t^n}^{t^{n+1}} \left( f(x_{j+\frac{1}{2}}, t) - f(x_{j-\frac{1}{2}}, t) \right) dt. \quad (4.7)$$

Defining the mean values by

$$U_j^n = \frac{1}{\Delta x} \int_{x_{j-1/2}}^{x_{j+1/2}} \omega(x, t^{n+1}) dx \quad (4.8a)$$

and

$$F(U; j + 1/2) = \frac{1}{\Delta t} \int_{t^n}^{t^{n+1}} f(x_{j+1/2}, t) dt, \quad (4.8b)$$

equation (4.7) becomes

$$U_j^{n+1} = U_j^n - \nu [F(U; j + 1/2) - F(U; j - 1/2)], \quad (4.9)$$

where

$$\nu = \frac{\Delta t}{\Delta x}. \quad (4.10)$$

Considering the solution of equation (4.2) in the region  $0 \leq x \leq L$  and for time  $0 \leq t \leq t_{end}$ , then this problem can be discretised onto a stationary uniform grid with space  $\Delta x$  and time step  $\Delta t$ , such that

$$x_j = j\Delta x, \quad t^n = n\Delta t. \quad (4.11)$$

The boundary of these discrete cells is clearly  $[x_{j-\frac{1}{2}}, x_{j+\frac{1}{2}}] \times [t^n, t^{n+1}]$ , so the solution in each grid cell will be given by (4.9). It is now apparent that the second and third terms on the right hand side of (4.9) represent the flux in from the cell to the left and the flux out to the cell on the right. All that is required to complete the method and solve this equation is to numerically approximate these flux terms.

If the cell averages are computed at time step  $t^n$  then the resulting scheme is explicit, whereas if the averages are computed at step  $t^{n+1}$  the scheme will be implicit. There are various advantages and disadvantages of explicit and implicit schemes. Explicit schemes are simpler, leading to less complex programs that require less computational effort to compute each step. The payoff of this is lower stability and hence

explicit schemes require the use of a small time step ( $\Delta t$ ) to stop the scheme becoming unstable. Implicit methods often lead to an under relaxation of the solution and hence a smoothing between neighbouring cells. For this reason implicit methods are often better when steady-state solutions are desired, but explicit schemes can give better temporal accuracy for lower computational expense. Also, since the equation under consideration is hyperbolic, information propagates at a finite speed. For these reasons attention will be restricted to a selection of explicit schemes.

Here, the exact flux  $F_{j+1/2}^t$  will be approximated by a numerical flux  $\mathcal{F}(U_{j+1}^n, U_j^n)$ . Hence all the methods considered will be explicit schemes with a *three-point stencil*, meaning that the value of  $U_j^{n+1}$  will only depend on  $U_{j-1}^n, U_j^n$  and  $U_{j+1}^n$ .

#### 4.1.1 Total variation diminishing (TVD) schemes

It is well known that first-order (upwind) methods result in smeared solutions and shocks can be lost, while second-order methods often produce spurious oscillations. The aim is to have a method which is second order accurate, but will not give rise to oscillations. Total variation diminishing (TVD) schemes have exactly this property. Several studies have shown the strength of TVD in capturing and following complicated shock structures. For example, [82] compared a variety of TVD methods, for a series of hydrodynamic and magnetohydrodynamics test problems. The methods performed extremely well and captured very intricate structures of the flows. Tai's PhD thesis, [79], demonstrates the power of the methods for numerical solutions of Savage-Hutter avalanche equations for numerous situations including the propagation of a shock wave in inclined chute flows. Due to the strong performance of TVD methods in flows with shocks, they have recently been applied to many complicated physical problems like galaxy formation [65] and gas explosion [22]. Additionally, many hybrid methods have started to be developed to help resolve shocks contained within solutions. For example Cho *et al.* used a hybrid TVD method to look at the flow over different air-foils, [12], whereas Hahn and Drikakis used a hybrid method to perform large eddy simulations [42].

It is useful to define the Total Variation ( $TV$ ) of a numerical solution at a given time step  $t^n$  by

$$TV(U^n) = \sum_{j=0}^{N-1} |U_{j+1}^n - U_j^n|. \quad (4.12)$$

It is clear that any oscillations will be such as to increase the  $TV$  of the function, therefore any scheme where

$$TV(U^{n+1}) \leq TV(U^n), \quad (4.13)$$

cannot have spurious oscillations. Any method satisfying this condition is called a TVD method.

It was shown by Harten, [43], that for the constant coefficients case i.e. when  $a = a_0$ , that the general form

$$U_j^{n+1} = U_j^n - C_{j-\frac{1}{2}}(U_j^n - U_{j-1}^n) + D_{j+\frac{1}{2}}(U_{j+1}^n - U_j^n) \quad (4.14)$$

is a TVD method if all the following conditions hold,

$$0 \leq C_{j-\frac{1}{2}} \quad \forall j, \quad (4.15a)$$

$$0 \leq D_{j+\frac{1}{2}} \quad \forall j, \quad (4.15b)$$

$$0 \leq C_{j+\frac{1}{2}} + D_{j+\frac{1}{2}} \leq 1 \quad \forall j. \quad (4.15c)$$

### 4.1.2 The CFL Condition

The *CFL* condition is a necessary but not sufficient condition for any explicit finite volume or difference method to remain stable. The condition is named after Courant, Friedrichs, and Levy and was first published in [15], then an English translation appeared much later in [16]. This condition states that a numerical method can only be convergent if its domain of dependence contains the physical domain of dependence in the limit of  $\Delta x$  and  $\Delta t$  tending to zero. Stated more physically, information is not allowed to propagate further in one time step than the numerical methods own domain.

When considering the *CFL* condition it is convenient to define the Courant number of the system. For (4.2) this is given by

$$C = a\nu, \quad (4.16)$$

where  $a$  is the wave speed defined by (4.3).

This condition will be used in the following sections when considering algorithms, which lead to stable *TVD* schemes.

### 4.1.3 The Lax-Friedrichs (LF) Method

As discussed above, finite volume methods require the evaluation of the flux through each boundary of the grid cells, which requires an estimate of  $U$  at these boundaries. The simplest method would be to take a piecewise linear construction i.e.

$$U_{j-1/2} = \frac{U_j + U_{j-1}}{2}. \quad (4.17)$$

Here and throughout the next few sections, the superscript  $n$  will be omitted for the flux functions because, as stated at the beginning of this chapter, only explicit methods will be considered, therefore, all the contributions to the numerical flux function,  $\mathcal{F}$ , will be evaluated at a time-step  $n$  not  $n + 1$ . Equation (4.17) implies a numerical flux of the form

$$\mathcal{F}(U_{j-1/2}) = \frac{1}{2}(f(U_{j+1}) + f(U_j)). \quad (4.18)$$

It is clear from the definition in §4.1.2 that the *CFL* for this case is  $\Delta x \geq a\Delta t$  or re-arranging

$$C \leq 1. \quad (4.19)$$

The resulting method is, however, very unstable and cannot be used even with a very small time step that satisfies the condition (4.19). However, stability can be recovered by adding to (4.18) a term to give

$$\mathcal{F}^{LF}(U_{j-1/2}) = \frac{1}{2}(f(U_{j+1}) - f(U_j)) - \frac{1}{2\nu}(U_j - U_{j-1}), \quad (4.20)$$

this is the classical Lax-Friedrichs method. The additional term appears to be modelling a diffusion style term. Since this extra term vanishes in the limit  $\Delta x \rightarrow 0$ , for a fixed value of  $\nu$ , the original equation is recovered as the grid is refined. From this it is clear that this additional term creates *numerical diffusion* that damps out the instabilities inherent in (4.18). This has the downside that the resulting method tends to smear the data unless a fine grid is used, which is computationally expensive, though the method is stable right up to the *CFL* limit of (4.19).

The scheme produced from substituting (4.20) into (4.9) gives

$$U_j^{n+1} = \frac{1}{2} [U_{j-1}^n + U_{j+1}^n] - \frac{\nu}{2} [f(U_{j+1}^n) - f(U_{j-1}^n)]. \quad (4.21)$$

Consider the constant coefficient case i.e.  $f(U_{j+1}) = a_0 U_{j+1}$ , when the method is reduced to

$$U_j^{n+1} = \frac{1}{2} [U_{j-1}^n + U_{j+1}^n] - \frac{\nu}{2} [a_0 U_{j+1}^n - a_0 U_{j-1}^n]. \quad (4.22)$$

In this form it is not possible to tell whether (4.22) is a *TVD* method, but by adding and subtracting  $U_j^n$  and  $(\nu/2)a_0 U_j^n$  (4.22), can be written in the form of (4.14), i.e.

$$U_j^{n+1} = U_j^n - \left[ \frac{1}{2} + \frac{\nu}{2} a_0 \right] (U_j^n - U_{j-1}^n) + \left[ \frac{1}{2} - \frac{\nu}{2} a_0 \right] (U_{j+1}^n - U_j^n), \quad (4.23)$$

which is clearly in the form of (4.14) with the identifications

$$C_{j-1/2} = \frac{1}{2} + \frac{\nu}{2} a_0 \quad \forall j, \quad (4.24a)$$

$$D_{j+1/2} = \frac{1}{2} - \frac{\nu}{2} a_0 \quad \forall j. \quad (4.24b)$$

It is clear that if  $a_0 \rightarrow -a_0$ , then the forms of (4.24a) and (4.24b) are interchanged, hence the case of  $a_0 \geq 0$  can be considered without loss of generality. Condition (4.15a), then, is automatically satisfied and condition (4.15b) can be rearranged to give  $C \leq 1$ , which is equivalent to the *CFL* condition for this problem and hence, must also be satisfied. Since  $C_{j+1/2} + D_{j+1/2} = 1$ , the final condition is also met. Hence, this Lax-Friedrichs method is a *TVD* for all  $a_0$  as long as the *CFL* condition is maintained.

#### 4.1.4 Slope Limiters

The first order  $LF$  scheme has been shown to be  $TVD$ , but being first-order it is highly diffusive. A system to make this method second-order, but remain  $TVD$ , needs to be constructed. A more general version of the cell reconstruction, (4.17), is

$$U_{j-1/2} = U_j + \sigma_j(x - x_j) \quad \text{for } x_{j-1/2} \leq x < x_{j+1/2} \quad (4.25)$$

Clearly, taking  $\sigma_j = (U_{j+1} - U_j)/\Delta x$  the above is reduced back to (4.17). Here, the more general form of

$$\sigma_j = \frac{\epsilon_j(U_{j+1} - U_j)}{\Delta x}, \quad (4.26)$$

is used, where  $\epsilon$  is a slope limiter,  $\epsilon_j = \epsilon_j(\theta)$  and will be a function of data smoothness.

The measure of smoothness,  $\theta$  is defined as

$$\theta = \frac{U_j - U_{j-1}}{U_{j+1} - U_j}, \quad (4.27)$$

i.e. the ratio of consecutive differences. This measure clearly breaks down as the variation becomes small, therefore the additional condition that

$$\theta \geq 0 \quad (4.28)$$

is also imposed. Clearly, (4.27) can only be negative near a turning point of  $U$ . In the locality of this point the function is smooth and definition (4.28) is sensible and consistent. It is now apparent that where the data is smooth,  $\theta$  is small and increases as the data becomes more discontinuous.

#### 4.1.5 Lax-Wendroff (LW) Method and TVD Limiters

In this section attention will again be restricted to the constant coefficient case. The information contained in this chapter closely follows §3 of [78]. The natural second-order extension to the flux in (4.18), presented in §4.1.3 for the constant coefficient case, is

$$U_j^{n+1} = \frac{a_0 \nu}{2} (U_{j+1}^n - U_{j-1}^n) + \frac{a_0^2 \nu^2}{2} (U_{j+1}^n - 2U_j^n + U_{j-1}^n). \quad (4.29)$$

This is called the Lax-Wendroff (LW) scheme and is stable upto its  $CFL$  condition, without the need for an additional numerical diffusion term, as used by the LF scheme.

It can be shown not to be a *TVD* method and its computation produces oscillations when shocks are present in the solution, which lead to large errors and numerical instability. Rewriting in the following form gives

$$U_j^{n+1} = U_j^n - a_0\nu (U_j^n - U_{j-1}^n) - \frac{a_0\nu}{2} (1 - a_0\nu) (U_{j+1}^n - 2U_j^n + U_{j-1}^n), \quad (4.30)$$

where it is clear that the LW method is a combination of a first-order method with the inclusion of an additional flux

$$-\frac{a_0\nu}{2} (1 - \nu a_0) (U_{j+1}^n - 2U_j^n + U_{j-1}^n), \quad (4.31)$$

which will be termed the ‘anti-diffusion flux’. Without this flux term, the method would be *TVD*. Its addition massively reduces the numerical diffusion but creates oscillations.

Sweby [78], proposed considering the method

$$U_j^{n+1} = U_j^n - \nu (U_j^n - U_{j-1}^n) - \delta_j^n \frac{\nu}{2} (1 - \nu) (U_{j+1}^n - 2U_j^n + U_{j-1}^n), \quad (4.32)$$

where  $\delta = \text{fn}(\theta)$ . It can be shown, for example in §6.11 of [57], that this is just a reinterpretation of slope limited methods as flux limiters, hence, the two descriptions are equivalent.

There are an infinite number of ways to write these formulae in the standard Harten form of (4.14). The obvious choice is

$$C_{i-1}^n = a_0\nu - \frac{1}{2}a_0\nu (1 - a_0\nu) \delta_{i-1/2}^n, \quad (4.33a)$$

$$D_i^n = -\frac{1}{2}a_0\nu (1 - a_0\nu) \delta_{i+1/2}^n, \quad (4.33b)$$

where  $\delta_{i+1/2}^n$  is used as short hand for  $\delta(\theta_{i+1/2}^n)$ . Since  $C > 0$ , written in this form the scheme does not seem to be *TVD* as it will always invalidate condition (4.15b).

Sweby, [78], showed that a more useful form of the expression is

$$C_{j-1}^n = a_0\nu + \frac{1}{2}a_0\nu (1 - a_0\nu) \left( \frac{\delta_{i+1/2}^n}{\theta_{j+1/2}^n} - \delta_{j-1/2}^n \right), \quad (4.34a)$$

$$D_j^n = 0. \quad (4.34b)$$

The *TVD* restrictions for this scheme, (4.15) are reduced to

$$0 \leq C_{j-1}^n \leq 1. \quad (4.35)$$

Assuming the *CFL* condition holds, this is true if

$$\left| \frac{\delta_{j+1/2}^n}{\theta_{j+1/2}^n} - \delta_{j-1/2}^n \right| \leq 2. \quad (4.36)$$

Since  $\theta_{j+1/2}^n$  and  $\theta_{j-1/2}^n$  are independent, this holds if both

$$0 \leq \frac{\delta(\theta)}{\theta} \leq 2 \quad \text{and} \quad 0 \leq \delta(\theta) \leq 2 \quad (4.37)$$

for all values of  $\theta$ .

Figure 4.1(A) shows a diagrammatic representation of this region described by (4.37). One of the dotted lines shows the LW method as given by (4.29), the diagram shows that this method is only *TVD* when  $\theta \geq 1/2$ , therefore, if a value of  $\theta$  smaller than this naturally occurs in the numerical solution of the hyperbolic equation, oscillations can be generated. The second dotted line shows another second-order scheme, the Beam-Warming method. This uses a one-sided difference (rather than a centred-difference, as in LW scheme) and for the linear case its flux is given by

$$\mathcal{F}_{j-1/2} = a_0 U_{j-1} + \frac{a_0}{2} (1 - \nu a_0) (U_{j-1} - U_{j-2}). \quad (4.38)$$

Again, figure 4.1(A) shows that this method is *TVD* as long as  $\theta \leq 2$ . Sweby suggested taking a linear combination of these two methods to produce a second-order method that is *TVD* everywhere. The resulting method exists for the region sandwiched between these two dotted lines and is often referred to as the second-order *TVD* region, this is highlighted in grey on plots (B)-(D).

There are clearly a lot of choices for limiters that lie in the *TVD* region, here only three will be considered,

$$\begin{aligned} \text{Minmod} : \quad & \delta(\theta) = \text{minmod}(1, \theta), \\ \text{Superbee} : \quad & \delta(\theta) = \max(0, \min(1, 2\theta), \min(2, \theta)), \\ \text{Woodward} : \quad & \delta(\theta) = \max(0, \min((1 + \theta)/2, 2, 2\theta)). \end{aligned} \quad (4.39)$$

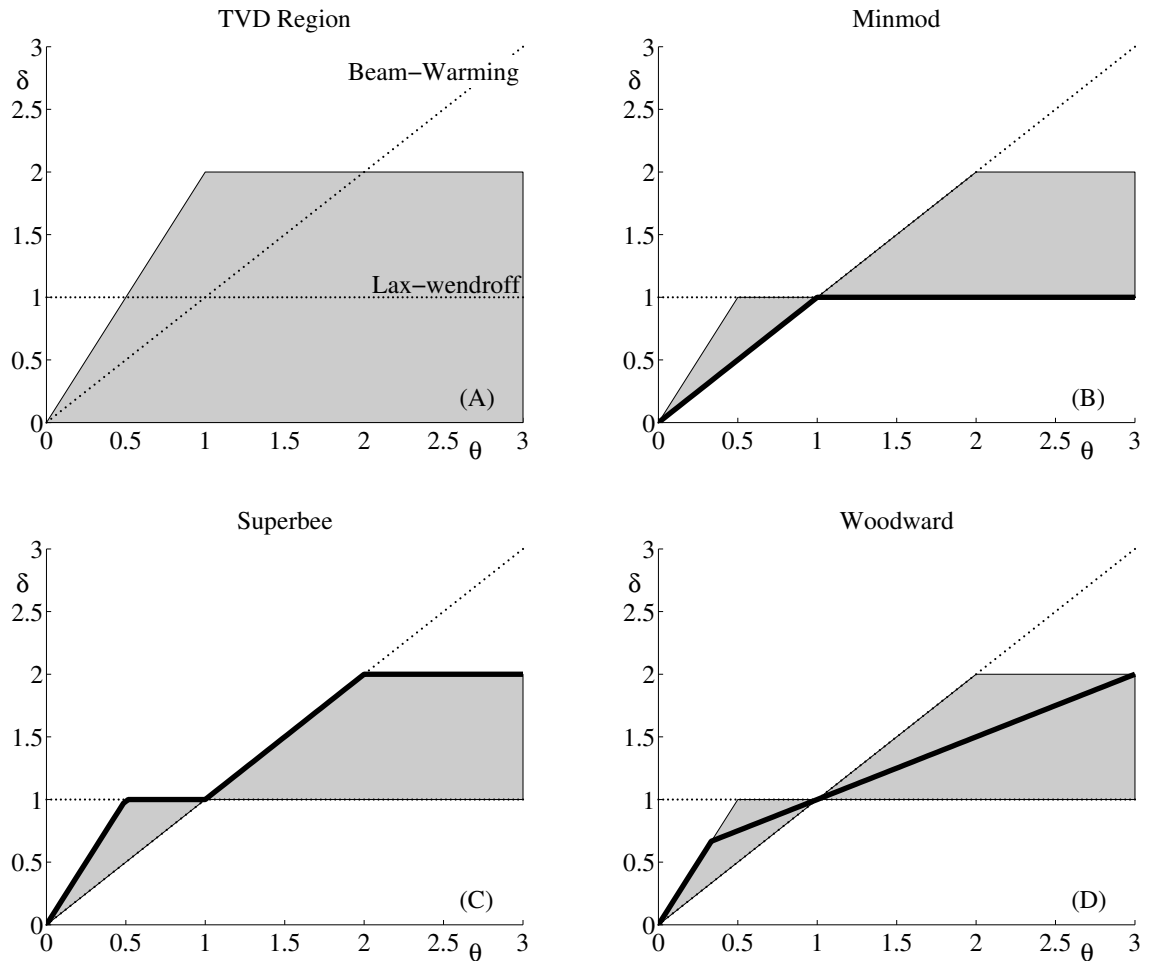


Figure 4.1: This figure graphically illustrates several limiters. Panel (A) shows the general *TVD* region (grey shaded region) and where the second-order Lax-Wendroff and Beam-Warming lie (dotted lines) on this plot. From here, it is clear that neither method is *TVD* for all possible values of  $\theta$ . The shaded region on panels (B)-(D) highlights the second-order *TVD* region. The black line of panel (B),(C) and (D) show the Minmod, Superbee and Woodward limiters respectively. All three produce second-order *TVD* methods. The Minmod limiter follows the lower boundary of the second-order *TVD* region, the Superbee the top boundary and the Woodward limiter lies somewhere between the two.

In figure 4.1 panels (B)-(D) illustrate all these limiters and show that they all lie within the ‘2D *TVD* region’. As the Superbee limiter sits along the upper boundary it leads to the least diffusive scheme, whereas the Minmod limiter gives the most diffusion. The Woodward limiter lies between the other two and has the additional advantage that it is continuous at the point  $(\delta, \theta) = (1, 1)$ . Many other limiters can be found in the literature but these basic three represent the far extremes, hence are a sensible starting point.

#### 4.1.6 TVD Lax-Friedrichs (TVDLF)

Applying slope limiters to one-dimensional methods can increase their order of accuracy and yet keep the method *TVD*. This philosophy is used to construct the Lax-Friedrichs *TVD* scheme, which is obtained by applying the Sweby 2D limiters to the original LF scheme (4.20), this gives

$$\mathcal{F}_{j+1/2} = \frac{1}{2} (f(U_{j+1/2}^R) + f(U_{j+1/2}^L) - \Phi), \quad (4.40)$$

where  $U_{j+1/2}^L = U_j + \frac{1}{2}\Delta x\delta_j$ ,  $U_{j+1/2}^R = U_{j+1} - \frac{1}{2}\Delta x\delta_{j+1}$ ,  $\Delta U_{j+1/2}^{RL} = U_{j+1/2}^R - U_{j+1/2}^L$  and

$$\Phi = \frac{\Delta x}{\Delta t} \Delta U_{j+1/2}^{RL}, \quad (4.41)$$

is the anti-diffusive flux. This method was originally proposed by Yee [91] and has the advantage that it does not require any knowledge about the characteristics and hence a Riemann solver.

It should be noted that it has not been proved (nor has ever) that the resulting scheme is *TVD* for the full non-linear problem. Calling these methods *TVD* is motivated by the analysis in §4.1.5 but is slightly misleading.

#### 4.1.7 Modified TVDLF (MTVDLF)

The original *TVDLF* method of Yee [91] was extended and improved by Toth & Odstrcil [82]. They introduced the Hancock predictor step to increase the temporal accuracy and suggested that Yee’s original  $\Phi$  should be multiplied by a local or global Courant number to obtain a less diffusive scheme.

This method produces the following flux

$$\mathcal{F}_{j+\frac{1}{2}}^{MLF} = \frac{1}{2} \left( f(U_{j+\frac{1}{2}}^R) + f(U_{j+\frac{1}{2}}^L) - c_{j+\frac{1}{2}}^{max} \frac{\Delta x}{\Delta t} \Delta U_{j+\frac{1}{2}}^{RL} \right). \quad (4.42)$$

There are many choices for  $c_{j+1/2}^{max}$ , if the global Courant number is used it is simply given by

$$c_{j+1/2}^{max} = c^{max} = \max_j(c_{j+1/2}). \quad (4.43)$$

Cockburn *et al.* [13] suggested the following *local* wave-speed was better

$$c_{j+1/2} = \nu \max(U_{j+1/2}^R, U_{j+1/2}^L), \quad (4.44)$$

whereas Barmin *et al.* [5] prefer to use

$$c_{j+1/2} = c(\Delta U_{j+1/2}^{LR}). \quad (4.45)$$

The later of the two is less computationally expensive. In this thesis (4.43) is used as it is the simplest and produces good results, see §4.4 for details of the testing.

To make the method second-order accurate in time, as well as space, the following Hancock predictor step is implemented

$$U_j^{n+\frac{1}{2}} = U_j^n - \frac{\nu}{2} \left( f(U_{j+\frac{1}{2}}^n) - f(U_{j-\frac{1}{2}}^n) \right) \quad (4.46)$$

and then a full step, using this predictor half step, as follows

$$U_j^{n+1} = U_j^n - \nu \left( \mathcal{F}(U_{j+\frac{1}{2}}^{n+\frac{1}{2}}) - \mathcal{F}(U_{j-\frac{1}{2}}^{n+\frac{1}{2}}) \right). \quad (4.47)$$

## 4.2 Dimensional splitting

So far, shock-capturing methods for one dimensional, non-linear, hyperbolic equations have been considered, the segregation equation, derived in §2, is a three-dimensional hyperbolic equation. Dimensional splitting, often called fractional stepping, is the easiest way to generalise a one-dimensional scheme to multi-dimensions. This technique is often used (e.g. [82]) and details can now be found in many standard textbooks, including §19.5 of [57]. In this section, the principles will be presented for two dimensions only, but it is clear how this generalises to higher dimensions.

Consider the following PDE

$$\mathbf{U}_t + \mathbf{F}(\mathbf{U})_x + \mathbf{G}(\mathbf{U})_y = \mathbf{0}, \quad (4.48)$$

with the initial condition

$$\mathbf{U}(\mathbf{x}, \mathbf{y}, \mathbf{t}^n) = \mathbf{U}^n. \quad (4.49)$$

In dimensional splitting, the time step is split into two separate sub-steps. In the first step the following PDE is solved,

$$\mathbf{U}_t + \mathbf{F}(\mathbf{U})_x = \mathbf{0} \Rightarrow \mathbf{U}^{(n+\frac{1}{2})}. \quad (4.50)$$

The solution gained is then used as the initial condition for this PDE

$$\mathbf{U}_t + \mathbf{G}(\mathbf{U})_y = \mathbf{0} \Rightarrow \mathbf{U}^{(n+1)}, \quad (4.51)$$

giving the full step solution. It will often be convenient to write this in the more compact operator notation

$$U^{n+1} = L_y^{\Delta t} L_x^{\Delta t} U^n. \quad (4.52)$$

If the original equation is linear, this method will produce an exact solution of the original equation. For a non-linear equation, it will still give a reasonable approximation to the result. Better approximations can be achieved by alternating the order of application for every time-step, thus, giving

$$U^{n+2} = L_x L_y U^{n+1} = L_x L_y L_y L_x U^n. \quad (4.53)$$

Two better truly second-order accurate alternatives are

$$U^{n+1} = \frac{1}{2} [L_x L_y + L_y L_x] U^n, \quad (4.54)$$

$$U^{n+1} = L_x^{\frac{\Delta t}{2}} L_y^{\Delta t} L_x^{\frac{\Delta t}{2}} U^n. \quad (4.55)$$

The second of these having a smaller computational cost.

### 4.3 Boundary conditions

The above method can be used to compute the interior points of the domain, but before the segregation equation (2.33) can be solved, a numerical representation of the

boundary conditions needs to be developed. From the analytic solutions in chapter 3, it is apparent that there are three types of boundary condition in these type of problems; inflow, outflow and solid walls.

### 4.3.1 Inflow conditions

For inflow boundaries, this is extremely straight forward as the boundary condition at these points is always of the form

$$U_i^n = \phi(z, t) \quad \forall i \quad \text{on an inflow boundary.} \quad (4.56)$$

Therefore, all that is required in the numerics is to set the cells on this boundary to a pre-determined function.

### 4.3.2 Outflow conditions

Outflow boundary conditions are a complicated subject, as mathematically there is no condition to be applied, so any condition used is *artificial*. On an outflow boundary, the solution needs to be continued without interference with the interior. Leveque, [57], §7.2.1 gives a good overview of the options available, with reference to the one-dimensional advection equation. The first option is to switch to an upwind method for the final grid cell. Since the method used in the bulk of the domain allows waves to propagate in both direction, this can lead to noise at the interface of this method switch. Alternatively the flux in the cell beyond the boundary can be approximated using a one-sided finite difference extension of the internal solution. Leveque, [57], states this is very effected for the advection equation. Since this is precisely the form the segregation equation takes, in  $x$ -direction, this second approach will be used in this thesis.

Let  $i$  represent the cells on the boundary, then the flux  $\mathcal{F}_{i+1/2}$  will require information about  $U_{i+1}$ . The simplest way of achieving this is to use *zero-order* extrapolation of the solution in the cell beyond the boundary, i.e.

$$U_{i+1}^n = U_i^n \quad \forall i \quad \text{on an outflow boundary.} \quad (4.57)$$

This would imply that  $U_{i+1/2}^R = U_j - 1/2\Delta x\delta$ , when computing the fluxes. This condition was originally used in the computations and was shown to lead to slight reflection from this boundary, therefore, the following higher order one sided extension

$$U_{i+1}^n = 2U_i^n - U_{i-1}^n, \quad (4.58)$$

was implemented instead. No noticeable reflection was observed with this condition.

### 4.3.3 Solid boundaries

For a solid boundary or free-surface, the condition that needs to be imposed is zero flux across this interface. Since the numerical algorithm works with the flux of the quantity under computation, this condition arises very naturally. The boundary should be chosen such that grid cells exist with one side constructing the interface. If the interface lies on the positive side of the grid cells, that make up its construction, then the condition

$$\mathcal{F}_{i+1/2}^n = 0, \quad (4.59a)$$

is imposed. If the boundary is on the negative side of the grid cells then

$$\mathcal{F}_{i-1/2}^n = 0, \quad (4.59b)$$

where  $i$  is the boundary grid cells.

## 4.4 Testing of the numerical method

In this section, a numerical algorithm will be developed for solving (2.33). This will be done by applying dimensional splitting, as outlined in §4.2. Attention will be restricted to the two-dimensional case, hence, it will be assumed that  $\phi$  and  $\mathbf{u}$  are independent of  $y$  and  $v = 0$  everywhere. Initially,  $u$  will only be considered to be a function of  $z$  and  $w = 0$ , this is precisely the situation for which analytical solutions were obtained in chapter 3. Therefore, the governing equation under consideration, in conservative form, is

$$\frac{\partial \phi}{\partial t} + \frac{\partial}{\partial x} (\phi u) + \frac{\partial}{\partial z} (-S_r [\phi (1 - \phi)]) = 0. \quad (4.60)$$

Applying the splitting procedure to this yields two equations

$$\frac{\partial \phi}{\partial t} + \frac{\partial}{\partial x}(\phi u) = 0 \quad \equiv \quad \hat{L}_x, \quad (4.61a)$$

$$\frac{\partial \phi}{\partial t} + \frac{\partial}{\partial z}(-S_r(\phi(1-\phi))) = 0 \quad \equiv \quad \hat{L}_z. \quad (4.61b)$$

A regularly spaced mesh will be constructed and the discretised concentration  $\phi_{ij}^n$  is defined at each grid point  $(i, j)$  and at time-step  $n$ . The grid points will be taken to range from 1 to  $N_x$  in the  $x$ -direction and from 1 to  $N_z$  in the  $z$ -direction. The centre of each grid cell will be located at  $(x_i, z_j)$ , where  $x_i = (i - 1/2)\Delta x$  and  $z_j = (j - 1/2)\Delta z$ . Hence,  $\Delta x = L_x/N_x$  and  $\Delta z = L_z/N_z$ , where  $L_x$  is the length and  $L_z$  is the height of the computational domain. Without any loss of generality,  $L_z$  can be taken to be 1, thus  $L_x$  becomes the aspect ratio of the domain under observation.

The domain will be assumed to have solid boundaries at  $z = 0$  and  $z = 1$ , hence, (4.59) implies

$$\mathcal{F}_{1/2}^n = 0 \quad \text{and} \quad \mathcal{F}_{N_z-1/2}^n = 0, \quad (4.62)$$

for all  $N_x$  one-dimensional problems that solve (4.61b). For the  $\hat{L}_x$  operator, the outflow condition (4.58) is applied at  $i = N_x$  implying

$$\mathcal{F}(\phi_{N_x+1/2}^n) = \mathcal{F}(2\phi_{N_x}^n - \phi_{N_x-1}^n), \quad (4.63)$$

where the long hand notation has been used for emphasis. The inflow condition will be implemented by enforcing that

$$\phi_{0j}^n = \phi_0, \quad (4.64)$$

where  $\phi_0$ , in general, can be a function of both  $z$  and  $t$ . No computation will take place in the first cell on the left, when solving the  $\hat{L}_x$  equation, as here the solution is prescribed. It should be noted that (4.64) is an approximation to the real condition, as the centre of the first grid cell is located at  $\Delta x/2$  not 0. This approximation gets better as the grid is refined and it did not appear to cause any problems with the computations.

To test the accuracy of the results, the use of an appropriate error is required. One sensible definition is the error per grid cell

$$\varpi = \frac{100}{N_x N_z} \sum_{ij} \left| \phi_{ij} - \phi_{\text{exact}|_{ij}} \right|. \quad (4.65)$$

To determine the *CFL* condition, it is necessary to calculate the maximum wave-speed of the problem. In the  $z$ -direction, the wave-speed is  $2\phi - 1$  and hence, the maximum wave-speed is 1. In the  $x$ -direction, the wave-speed is simply  $u$  and hence from the linear profiles under consideration (3.24), the maximum wave speed in this direction is  $2 - \alpha$ , as the domain is always taken to extend from  $z = 0, 1$ . This is always greater than the  $z$ -direction wave-speed, hence, for these problems the *CFL* condition, (4.47), gives

$$\Delta t = C \frac{\Delta x}{2 - \alpha} \quad \text{where} \quad C \leq 1. \quad (4.66)$$

#### 4.4.1 Test case 1 : Steady-state homogeneous inflow

The first problem to be considered, is the steady-state solution from a homogeneous inflow of material. The analytic solution to this problem is described in §3.1. A modified *TVDLF* scheme was used with a Superbee limiter and taking  $c_{j+1/2}^{max}$  to be the global Courant number as this is computationally the least expensive method. The code was run on square grids with between 100 and 1000 points with a Courant number of 1. Steady state was determined by sampling the data every 0.1 dimensionless seconds and requiring that the change in  $\phi$  was less than 0.1% per grid cell. This was done for the cases of  $\alpha = 0, 0.5, 1.0$ . Figure 4.2 shows the error norm,  $\varpi$ , for each of these runs. As can be seen, the error is small even for the case of 100 points, which runs in less than 5 seconds on a desktop computer. The general trend is for the error to decrease as the number of points is increased, but there is a slight oscillation. This is because there was a slight variation, with points, in the exact time the steady state was achieved. For  $\alpha = 0$ , this occurred between  $t = 1.82 - 2.00$ , for  $\alpha = 0.5$  between  $t = 2.12 - 2.17$  and for  $\alpha = 1$  between  $t = 2.13 - 2.28$ . The codes that ran slightly longer appear to have a lower than expected error. Secondly, these methods

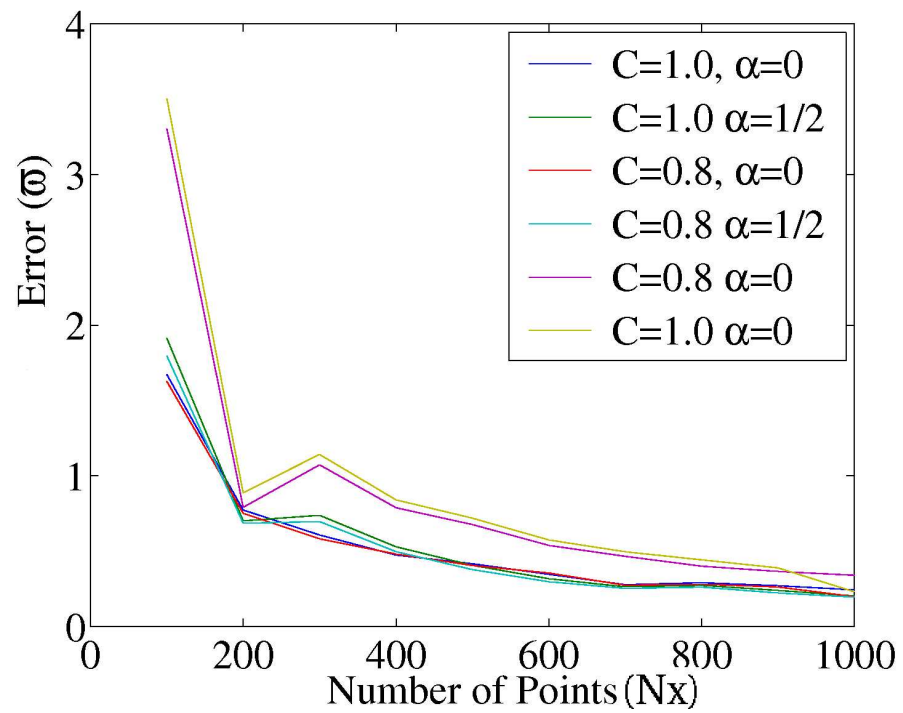


Figure 4.2: Figure showing the percentage error norm  $\varpi$  against number of points used in the the computation for test case 1. The test was preformed with 10 different grids using between 100 and 1000 points ranging in steps of 100 and two different Courant number 0.8 and 1.0

have a tendency to overshoot steady-state and slowly oscillate around, then decay towards the exact solutions. This was checked by measuring the error against time near the steady-state and these oscillations were observed. Therefore, the phase of this oscillation at the time steady-state was chosen to have been achieved would add a random element to the error measurement. These two factors together explain the occasional peak in  $\varpi$  at various grid cell sizes. This problem will not appear when testing the temporal development of the flow, outlined in the next section, hence this should provide a better test of the scheme.

Using the smaller Courant number of 0.8 gave a lower error and reduced the size of this over-shoot. Additionally, it is computationally only 25% more expensive. For these reasons, it seems sensible to use this lower Courant number for the more complicated problems later on.

A similar plot to figure 4.2 was obtained in the the steady-state solution for the normally graded case, see §3.2 for analytical solution. The error was a little higher in all cases by about 1%, but with a grid of 300 by 300 the error was below 3.8% for all values of  $\alpha$ .

#### 4.4.2 Test case 2 : Time-dependent numerical test

Some of the plug-flow analytic solutions obtained in §3.3 and §3.4, will be used to investigate the temporal accuracy of the code. Figure 4.3 shows the error for the situation described in §3.3.3, i.e. the chute is initially filled with homogeneously mixed material, with  $\phi = 0.5$ , and identical material is fed in from the boundary for all time. The error in the solution is seen to oscillate with time, and for the 100 by 100 points case does seem to grow linearly until the steady-state is reached. It should be noted that this growth of error with time was only seen on the 100 by 100 grid and was not observed on a grid with 200 by 200 cells. After  $t = 1$ , the error in the solution quickly drops and becomes constant, then, as the number of points is increased, the error in the final steady-state is reduced. Strangely, for this problem, in the early time solution the error is slightly higher with 1000 points than 500. The

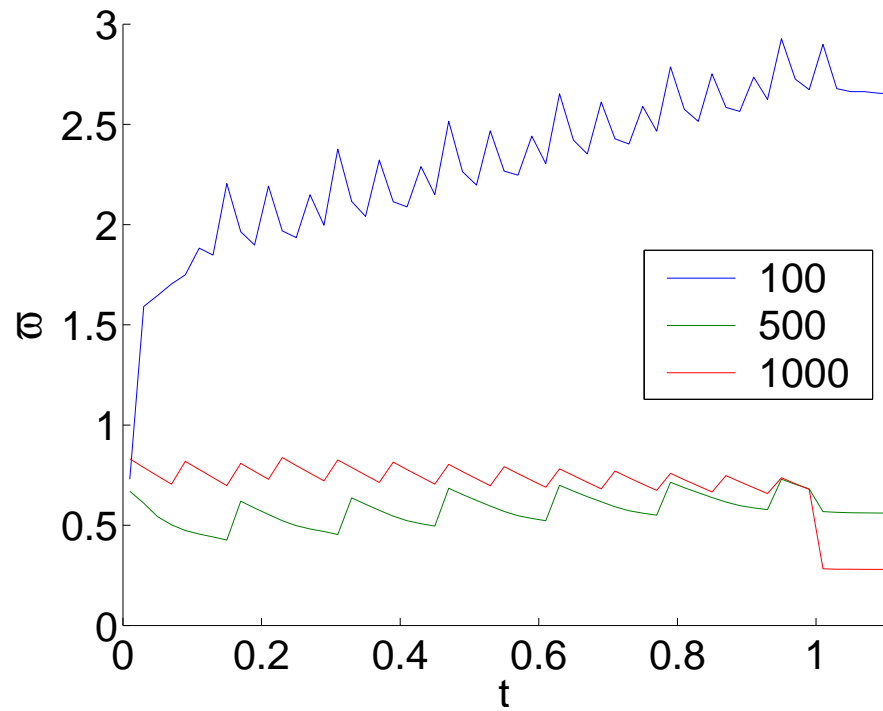


Figure 4.3: Graph showing the numerical error compared to the analytic solution, in using the numerical method. The problem and its analytical solution are described in detail in section 3.3.3. The analytic solution reaches steady-state at  $t = 1$ . The measure of the error  $\varpi$  is given by (4.65) and the error is shown for three different grids 100 by 100, 500 by 500 and 1000 by 1000. The Superbee limiter was used for all cases.

reason for this increase in the temporal error could again be due to the overshoot in the solution when using a large Courant number, this is discussed in more detail for test case 3.

Tests were performed with some of the other solutions and similar results were observed. The error in the steady-state solution always decreased with increasing points and there was an oscillation in the error. In some, but not all, of the problems the time-dependent problem was slightly worse with decreasing cell size. It should be noted that in these situations the error was always small, i.e. below 1.5% for all grid sizes where the effect was apparent.

In the more complicated problems the error was higher, but for all the cases with 300 points it was very hard to tell the difference between the analytical and numerical solution when viewed in the same resolution. The numerical method is also very fast. The run time of this code, for the problem just considered in this section, on a 2010 MHz AMD Athlon using square grids

$$t \approx 1.6 \times 10^{-6} n^3 \tilde{t}, \quad (4.67)$$

where  $n$  is the number of points in any one direction and  $\tilde{t}$  is the non-dimensional time the code is run for. This was calculated by timing the code (the actual user time was used, not the physical time elapsed) for different length  $\tilde{t}$  and plotting it against  $n^3$ . The formula is accurate to 1d.p. for  $n > 300$  and  $\tilde{t} > 1$ , but closer analysis showed that there should also be a constant term and a term proportion to  $n$ . This should be expected as there is an overhead in initialising the code (constant term) and in the dimensional splitting process (proportional to  $n$  term). One implication of this formula is that the code will run in real time on a grid with 85 points.

### 4.4.3 Test case 3 : Shear and time-dependence

So far, it has been shown that the numerical method is robust (as it can handle very complicated problems without crashing), fast and stable. There is a minor outstanding issue of the error in the time-dependent case, but this only seems to occur in the high points limit, where the error is quite low. What remains to be done

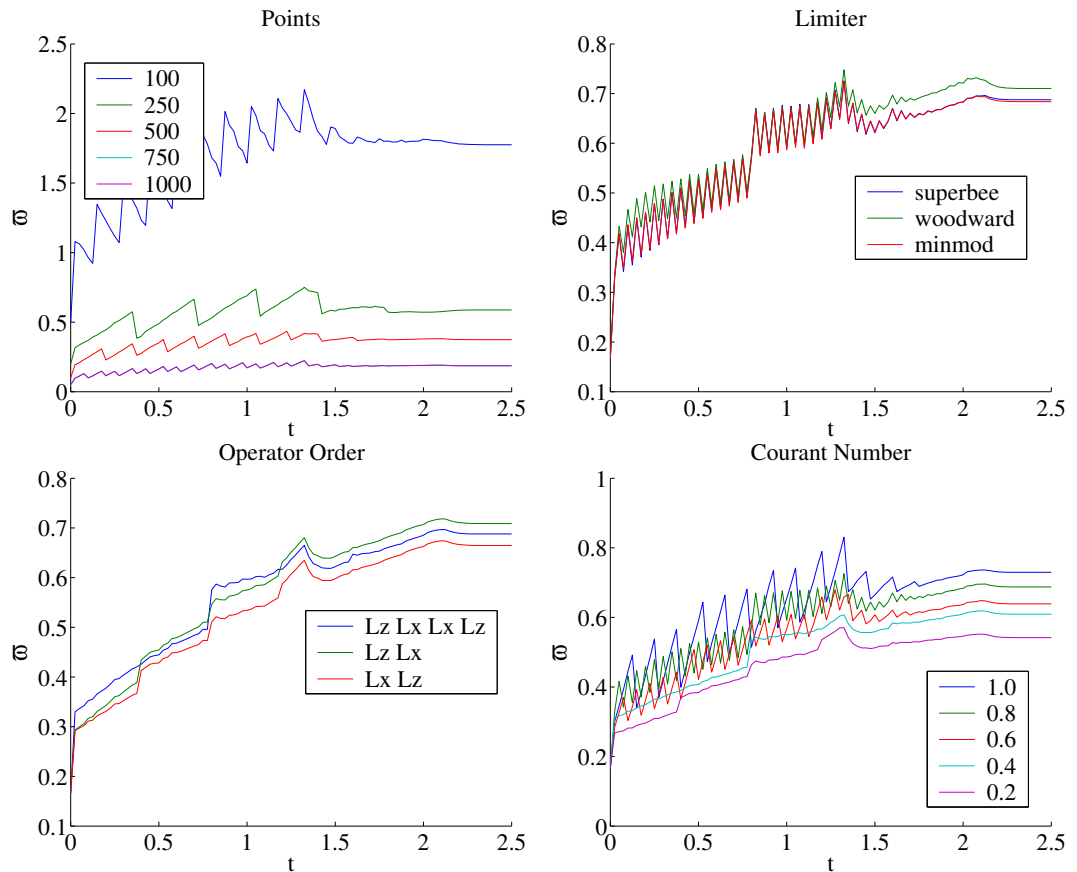


Figure 4.4: Above are plots of the percentage error ( $\varpi$ ) against time. These are for the case of the inflow of homogeneous mixed material with equal volume of each type into a chute initially filled with small particles. The separate plots show the effect of changing the number of grid points, the limiter, the Courant number and the order of application of the split operators, respectively. If not stated on the plot, the runs are on a grid of 300 by 300 cells, with a Courant number of 0.8, the Superbee limiter and changing the order of application of the operators after each step.

is to investigate the effect of changing the limiter and operator order.

To investigate this problem, the analytical solution, outlined in appendix C, will be used. This is taken from [35], this paper and its sister paper [73] extend the analytic work presented in §3 to time-dependent problems with shear. The exact problem to be considered is the homogeneous inflow of material, with volume fraction  $\phi = 0.5$ , into a chute initially filled with small particles, with  $\alpha = 0.5$ . This problem was considered in §3.3.3 for the  $\alpha = 1$  case.

Figure 4.4 shows several plots of the error. It is interesting that there is sharp change in the error as certain shocks in the solutions are created and destroyed, which is not surprising. This problem is well behaved in the sense that, for all time, the error is lower with an increasing number of grid cells (see top left panel). The same increase in accuracy is also seen as the Courant number is decreased, where the size of the oscillations in the error drops sharply. For  $C \leq 0.4$ , these have disappeared all together. These oscillations could be due the solution being overshoot when a large time step is taken and may easily be the cause of the increase in error with grid refinement in the previous problem. The top right panel shows that changing the limiter has very little effect and that the Superbee and Minmod limiters are slightly better than the Woodward limiter. Again, changing the order of application of the operators has very little effect, surprisingly alternating the order is not the best method and for  $t < 0.5$  is actually the worst method.

From this point on, unless otherwise stated, all numerical work will take place on grids of 300 by 300 using the Superbee limiter. The order of application of the operators will be continued to be changed every time-step, even though there is some evidence that always applying the  $x$  operator first leads to a lower error. Finally if high temporal accuracy is required, a Courant number of 0.4 should be used. However for computing the steady-state solution, a Courant number of 0.8 is more sensible as it leads to a lower computation time. Therefore, from this point onwards, unless stated otherwise, a Courant number of 0.8 will be used.

## 4.5 Effect of weak shear

In this section, some of the time dependent analytic solutions derived in §3.3 are numerically investigated with a weak shear velocity profile i.e.  $\alpha = 0.8$ . This profile is more realistic for many observed flows and some shear is required for the ‘kinetic sieving’ mechanism to be active. The effect of weak shear on the problems outlined in §3.3.3 and §3.3.4 will be investigated, using the numerical method outlined above on grids with 300 by 300 points. Figure 4.5 shows the results for the case when the initial and inflow concentrations are 50%, which are comparable to those in figure 3.10. The solution in the uniform region determined by the initial conditions is identical to the plug-flow solution in section §3.3.3. The most important effect of shear is that the transition from initial to boundary condition controlled solutions occurs at different times at different levels in the flow. This can clearly be seen from the position of the kinks in the shocks at  $t = 0.7$ , in the lower left panel. The top transition therefore, intersects with the lower horizontal shock at  $z = 1/2$  at  $t = 1$ . However, due to the shear, it does not link up with the bottom transition, which intersects with the top shock a short time later. This creates a third shock which has three, clearly defined regions; a straight portion at the steady-state height of the no shear case, a transition zone and another straight section at  $z = 1/2$ , which can be seen at  $t = 1.5$ . The mismatch in height is swept downstream and out of the domain, so that locally, the solution is close to steady-state at  $t = 2$ . The shear causes the mismatch interface to steepen very slowly and it eventually breaks in finite time far downstream.

Figure 4.6 shows the results when the inflow concentration is periodic and is given by (3.72), i.e. it varies sinusoidally about a background concentration of 50%. The results are similar to those in figure 3.11, but the concentration contours in the inflow region tip over with downstream distance, in response to the shear. When the two shocks meet a triple-point is formed, which move from side to side, as well as up and down. This introduces oscillations into the boundary controlled section of the third shock, which are advected downstream and slowly steepen and break. Additionally the amplitude of the oscillation in the segregation shock is noticeably lower than

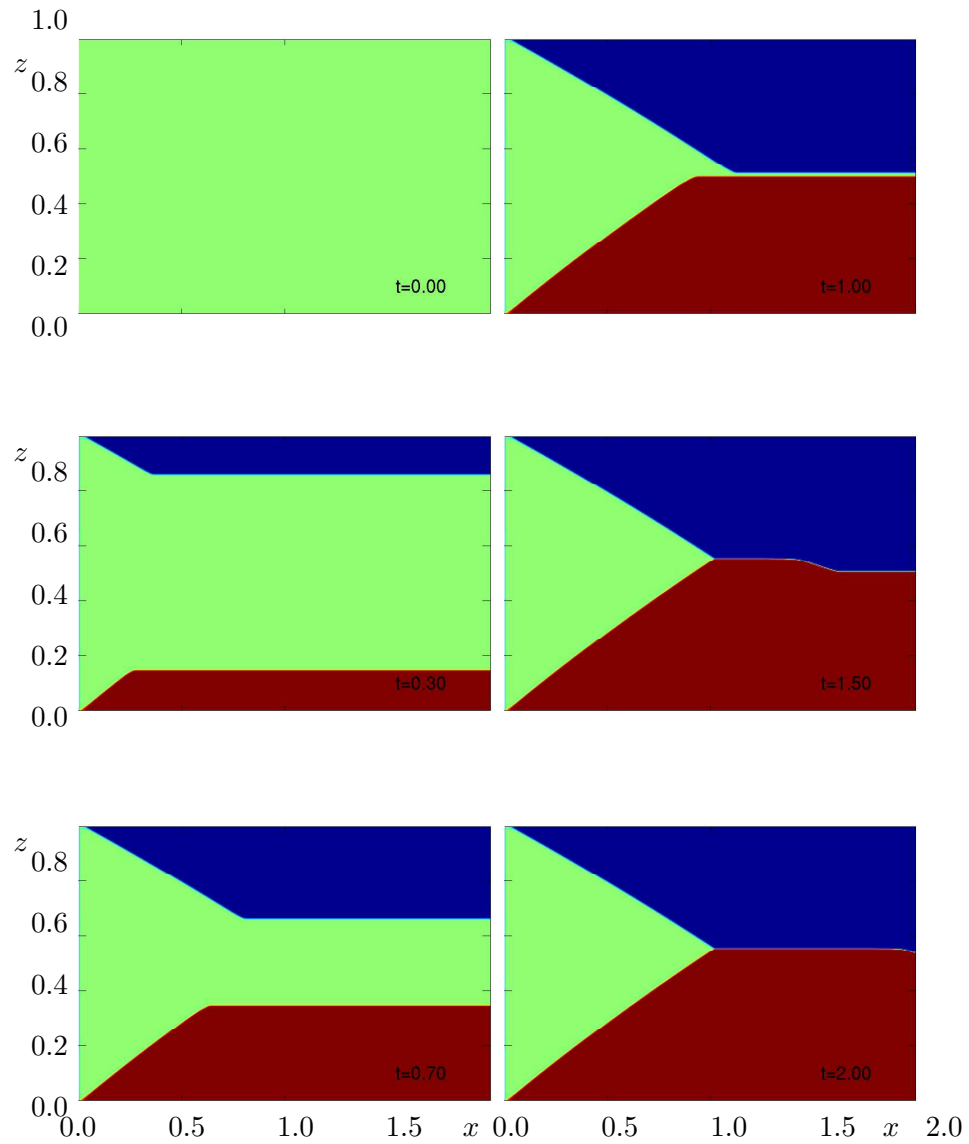


Figure 4.5: The evolution of the volume fraction of small particles,  $\phi$ , as a function of the downslope coordinate,  $x$ , and avalanche depth,  $z$ . The bulk flow is from left to right and the normal contour scale is used. The chute is initially filled with 50% small particles by volume and the same mixture flows in from the left. This case corresponds to a segregation number  $S_r = 1$  and a shearing/translating flow with  $\alpha = 0.8$ .

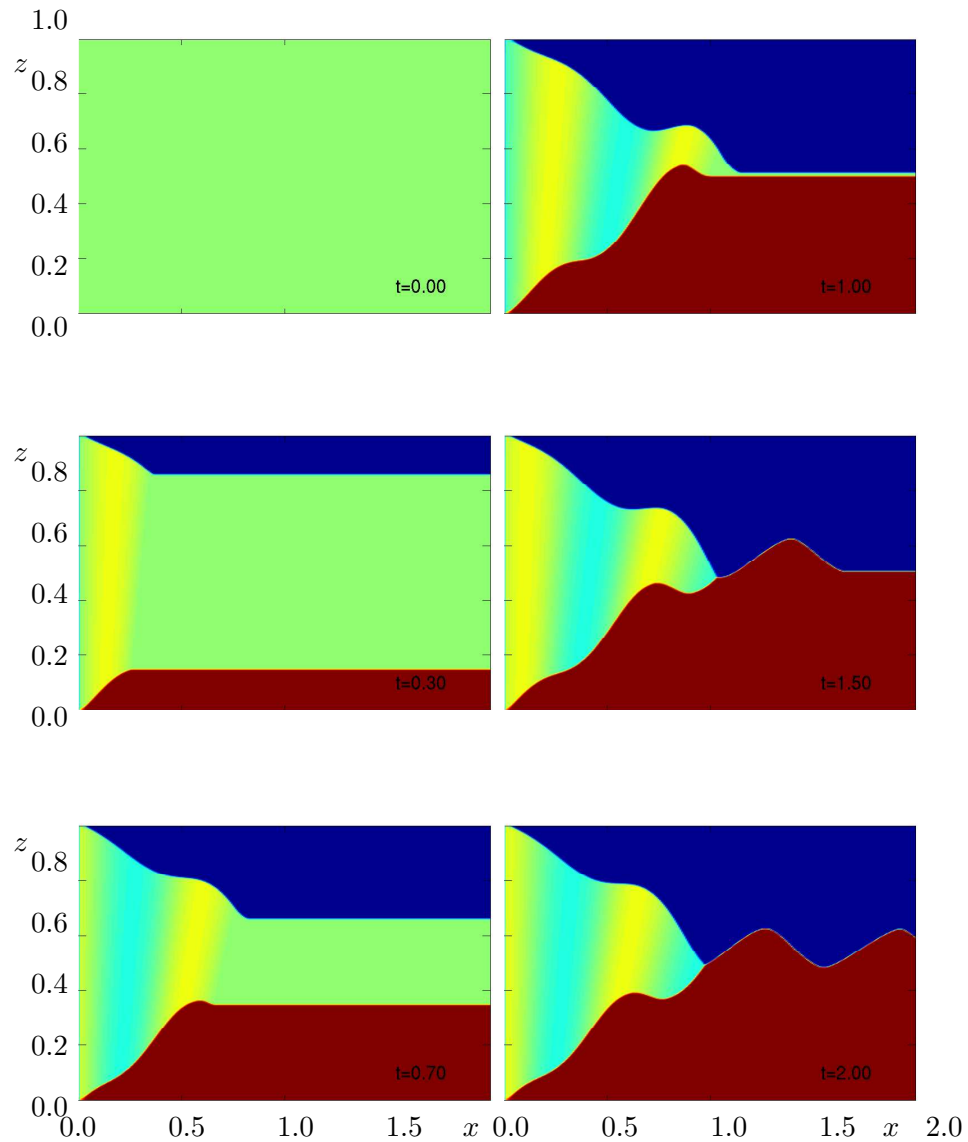


Figure 4.6: The evolution of the volume fraction of small particles,  $\phi$ , as a function of the downslope coordinate,  $x$ , and avalanche depth,  $z$ . The bulk flow is from left to right and the normal contour scale is used. The chute is initially filled with 50% small particles. At  $x = 0$ , a mixture of particles whose concentration varies sinusoidally in time, with amplitude 10% about a mean background concentration of 50%, enters the chute. This case corresponds to a segregation number  $S_r = 1$  and a shearing/translating flow with  $\alpha = 0.8$ .

the amplitude by which the boundary conditions are changed. This tendency to smooth out imperfections in the segregation shock seems to be a generic feature of shear. Further tests showed that this effect increased with greater shear and a higher frequency of oscillation.

## 4.6 Shear and normally graded inflow

In this section, the effect of slightly stronger shear is investigated on the normally graded inflow solutions. Analytical solutions for this configuration can be found in both §3.2 and §3.4.

### 4.6.1 A chute initially filled with normally graded material

The problem that will be considered is the chute initially being filled with material separated at a height of 0.5 and the same normally graded material being fed in at the inflow. This is precisely the problem considered in §3.4.1 and a detailed mathematical statement of the problem can be found there.

The solution for a velocity field given by  $\alpha = 1/2$ , which has both linear shear and basal slip, is shown in figure 4.7. The numerical solution has many similarities with both, the two-dimensional time-dependent plug-flow solution, of §3.4.1, and the steady-state solutions of §3.2. As the initial distribution is independent of the downslope coordinate,  $x$ , the time-dependent part of the solution, which evolves from the initial conditions, is in fact identical to plug-flow. The material that flows onto the chute creates a steady-state region, which is identical to the solution in the upper middle left panel of figure 3.6. Between the two regions there is a complex transition. For  $t < 1/2$ , as the fan propagates towards the boundaries, the transition starts parallel to the  $z$  axis and slowly tips over to the right in response to the shear. Once the upper and lower shocks are generated the transition widens into a relaxation zone as the solution matches up the time-dependent and steady-state shocks, which, as opposed to plug-flow, now lie at different heights. At  $t = 2$ , the upper and lower shocks meet and a third shock is produced, which lies at height  $z_3 = 1/2$  in the

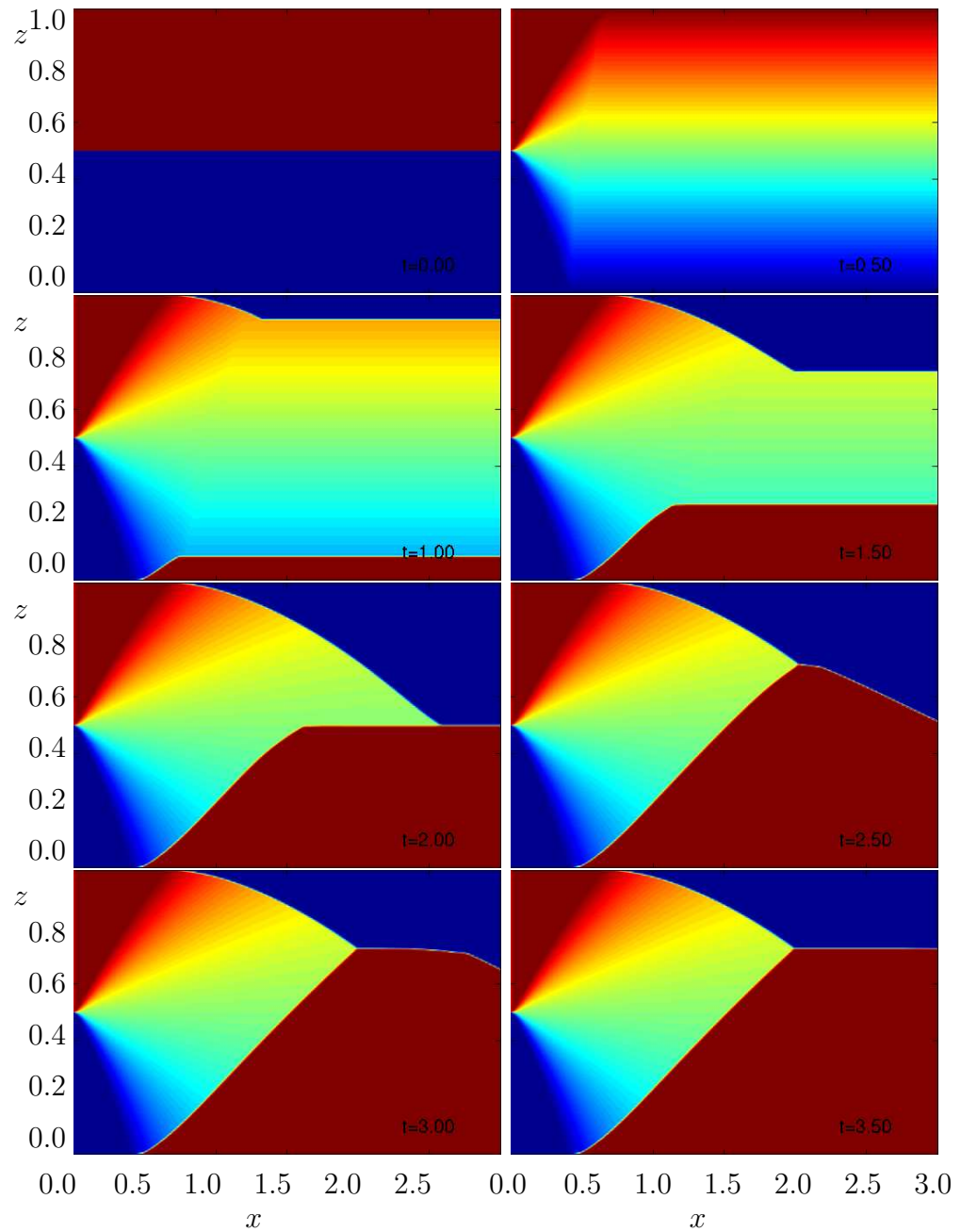


Figure 4.7: The numerical solution for the concentration of small particles,  $\phi$ , is shown using the normal contour scale at a series of time-steps for a chute, which was initially filled with normally graded material separated by the line  $z_r = 1/2$ . A linear velocity profile with basal slip ( $\alpha = 1/2$ ) transports the material downslope from left to right and normally graded material is fed onto the chute at  $x = 0$  to replenish the avalanche. The discontinuity height is  $z_r = 1/2$  and the segregation number is  $S_r = 1$ .

initially uniform region. As the transition propagates further downslope, the two steady-state shocks meet just before  $t = 2.5$  to produce a steady-state shock that lies at  $z_3 = (\sqrt{6} - 1)/2$ . The third shock has a fairly linear transition region between these two regions, which is advected downstream and out of the domain by  $t = 3.5$ . The solution therefore reaches a local steady-state, but the mismatch persists and eventually breaks far downstream.

### 4.6.2 A chute initially filled with large particles

The evolution towards the local steady-state can be markedly different. Consider now, the alternative case in which the chute is initially filled with large particles

$$\phi(0, x, z) = 0, \quad 0 < z < 1, \quad x \geq 0, \quad (4.68)$$

subject to the same boundary conditions as before. For plug-flow, the solution would look similar to figure 3.13, except that the time-dependent region would be replaced by a constant uniform state of large particles. When there is a velocity gradient, the small particles are progressively sheared across the top of a region of large grains beneath and immediately start to percolate down through the matrix as shown in figure 4.8. By  $t = 0.5$ , a complex transition region develops, between the steady-state solution to the left and the constant uniform state of large particles to the right, which appears to consist of an additional unsteady shock and an expansion fan. Once the lower characteristic reaches the base a pure region of small (blue) particles separates out at the bottom ( $t = 1$ ) and a lower finite length unsteady shock develops. This grows in size and eventually cuts off the unsteady transition expansion between  $t = 2.5$  and  $t = 2.6$ , leaving the steady-state fan behind. The unsteady expansion is eroded and disappears by  $t = 3$ , to leave a concentration jump between the large particles above and the fines beneath. This jump is swept downstream and eventually breaks far downslope, but a local steady-state is attained by  $t = 3.5$ .

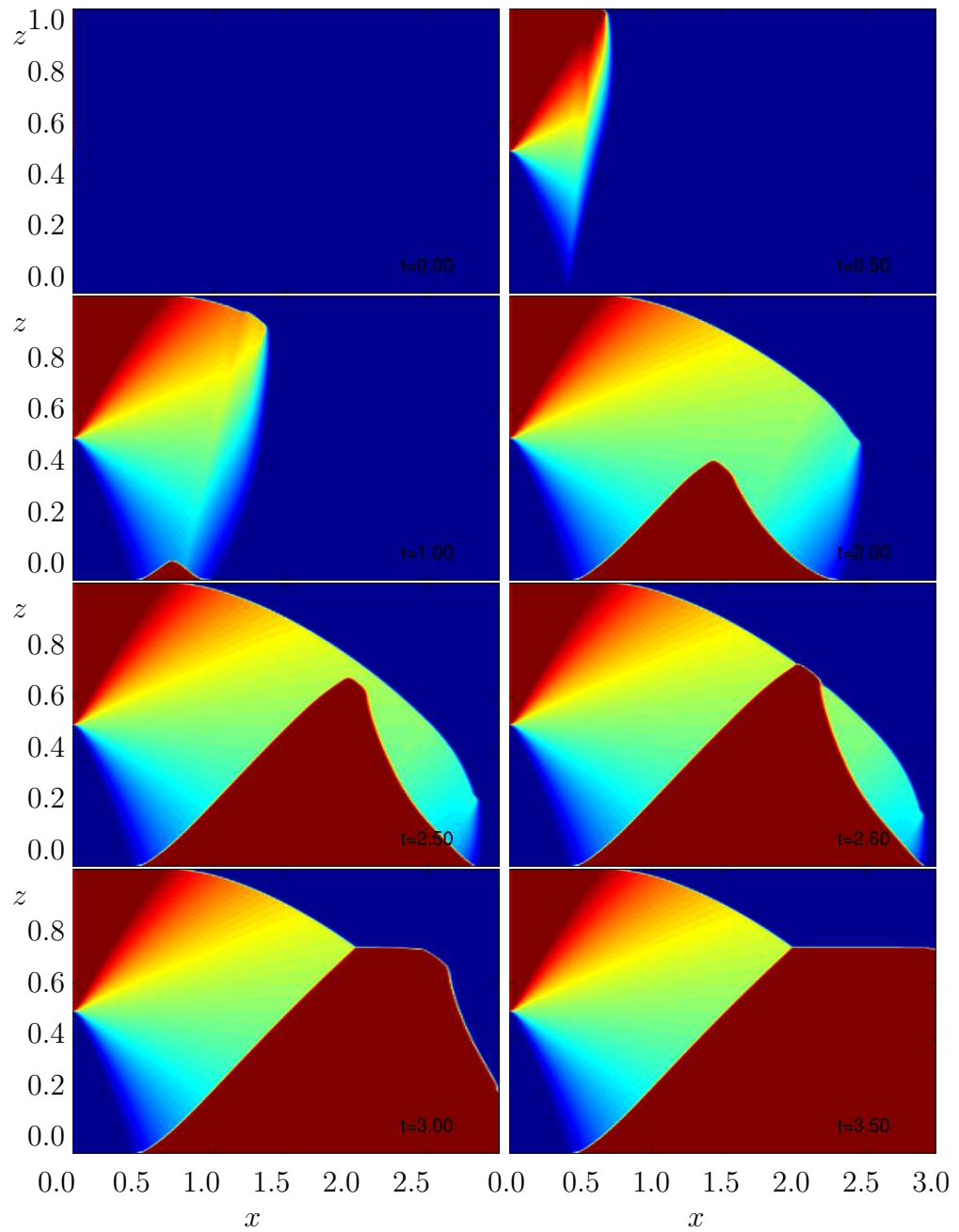


Figure 4.8: The numerical solution for the concentration of small particles,  $\phi$ , is shown using a contour scale at a series of time-steps for a chute. which was initially filled with large particles. A linear velocity profile with basal slip ( $\alpha = 1/2$ ) transports the material downslope from left to right and normally graded material is fed onto the chute at  $x = 0$  to replenish the avalanche. The discontinuity height is  $z_r = 1/2$  and the segregation number is  $S_r = 1$

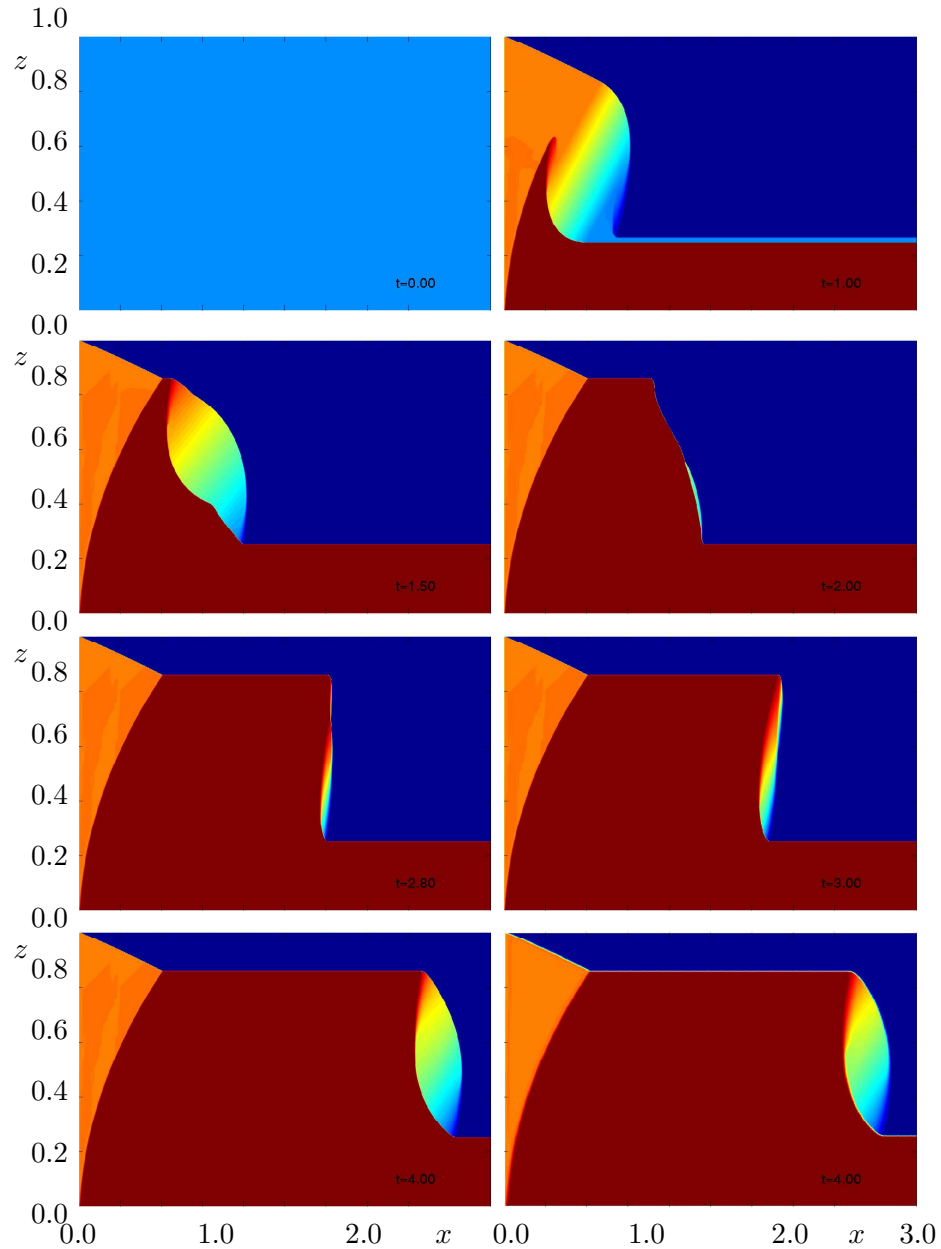


Figure 4.9: The figure shows the time-development of segregation from a chute initially filled with a homogeneous mixture with concentration 0.25. At the inflow boundary, a homogeneous mixture of higher concentration (0.75) is fed into the domain. All plots (except bottom right) are constructed with 1000 by 1000 points. The bottom two panels both show the solution at  $t = 4$ , the left panel was constructed with 1000 by 1000 points and the right panel with 300 by 300 points. There is very little difference between the two plots. The normal contour scale has again been used.

## 4.7 Strong shear and wave breaking

As has been alluded to in the previous two sections, shear in the flow leads to the steepening and eventually breaking, of any kinks in the segregation shock. In this section, this problem is looked at in more detail and will be investigated using a version of the problem discussed in §3.3.5. The chute will be initially filled with a homogeneous mixture, with  $\phi = 0.25$ . From the inflow, located at  $x = 0$ , homogeneous mixed material with  $\phi_0 = 0.75$  will be fed in.

Figure 4.9 shows the evolution of this problem. In the top right panel, a complicated time dependent ‘lens’ type structure can be seen to develop, due to the fact that the material in the chute segregates to a different height than the material being fed in from the boundary. At  $t = 1.5$ , this ‘lens’ has become completely cut off and the steady-state solution, as given by §3.1, exists for all  $x \leq 1$ . This complicated structure is destroyed producing a very elaborate segregation shock at  $t = 2.05$ . The second from top right panel shows the end of this ‘lens’ structure and the production of a highly curved segregation shock. Due to the shear in the flow, this shock begins to steepen and eventually, breaks at two different points to produce two new propagating ‘lens’ structures ( $t = 2.8$ ). At  $t = 3$ , these two lenses intersect creating a single, large lens. This grows in size and then propagates at a constant speed.

The bottom two panels both show the structure of the solution at  $t = 4$ , the left hand panel was computed using 1000 grid cells in each direction and right hand panel using 300 grid cells. From this, it is clear that there is very little difference between the two, revealing no evidence of grid dependence.

# Chapter 5

## Breaking zones and recirculation

In chapter 4, the formation of a travelling ‘lens’ structure has been observed in problems where waves have broken. In this chapter, this structure will be investigated further. It is clear from the numerical work that this is formed when small particles are sheared over large grains. This is often the case in nature, for example, within the material flowing in an avalanche. Within the flow, initially vertical segregation will take place, which will then be followed by lateral transport. Due to the shear it would be expected that after a long time, the large particles are transported to the front of the flow and all the small particles towards the back, setting up horizontal segregation. The shear profile will try to advance the small particles along the top, towards the front, and the small particles towards the back, along the base. This phenomena is more generic than finite mass problems (i.e. the avalanching material occupies a finite amount of space, in contrast to the infinite chute flow problems considered in chapter 3) and occurs in any situation where a non horizontal segregation shock and shear are both present. The question is; what happens in a steady-state uniform flow of this kind?

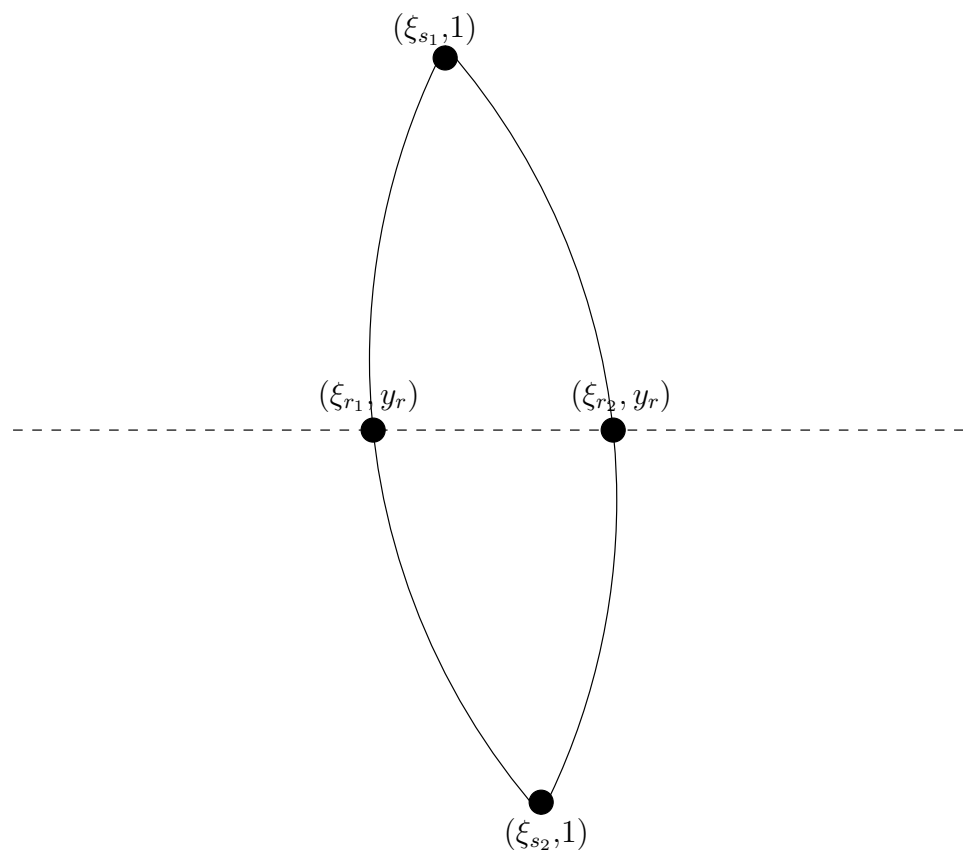


Figure 5.1: Schematic diagram of analytic solution, showing the four key points which define the solution. Fans are generated from the two points on the centre line, which fill the domain contained by the solid lines. The top/bottom solid dots shows the generation location of the two shocks present in the ‘lens’.

## 5.1 Analytical solution

To begin, we transform to a frame of reference moving with the mean velocity  $\bar{u}$ . The transformation is

$$\xi = x - \bar{u}t, \quad \tau = t. \quad (5.1)$$

The segregation equation (2.35) becomes

$$\frac{\partial \phi}{\partial t} + \hat{u} \frac{\partial \phi}{\partial \xi} - S_r \frac{\partial}{\partial z} (\phi(1 - \phi)) = 0, \quad (5.2)$$

where  $\hat{u} = u - \bar{u}$ . For a steady-state to develop, the large particles which move back relative to the mean flow must balance the particles moving forward. Therefore, there must be a level,  $z = z_r$ , where this balance occurs. This level corresponds to the point where  $\hat{u} = 0$ . The equation governing this quasi steady-state (quasi steady because it is steady in a moving frame) is

$$\hat{u} \frac{\partial \phi}{\partial \xi} - S_r \frac{\partial}{\partial z} (\phi(1 - \phi)) = 0. \quad (5.3)$$

The similarity of (5.3) with the equation under investigation in chapter 3, i.e. (3.2), means that it is clear that the Method of Characteristics (see §3.1.1 for details), for this situation, leads to

$$\phi = \phi_\lambda, \quad \text{on} \quad \hat{u} \frac{dz}{d\xi} = S_r(2\phi_\lambda - 1). \quad (5.4)$$

As in the steady flow cases, flux-coordinates may be defined

$$\hat{y} = \int_0^z \hat{u}(z) dz. \quad (5.5)$$

These have the property that  $\hat{y} = 0$  at the free surface and at base of the avalanche, and  $\hat{y} = \hat{y}_r < 0$  at  $z = z_r$ . For the linear velocity field,  $u = 2z$ ,  $\hat{u} = 2z - 1$ , implying  $\hat{u} = 0$  at  $z = 1/2$ , and so  $y_r = -1/4$ . For a parabolic profile given by  $u = 3\sqrt{z}/2$ ,  $\hat{u} = 3\sqrt{z}/2 - 1$ , for which the latter has a zero at  $z_r = 4/9$ , and, hence,  $y_r = -4/27$ . With these coordinates, the characteristic equation reduces to

$$\frac{\partial \hat{y}}{\partial \xi} = S_r(2\phi_0 - 1). \quad (5.6)$$

Suppose that at steady-state the small particles occupy the region  $\xi < \xi_{r1}$ , then it would be expected that a rarefaction wave would develop at this interface i.e.  $(\xi_{r1}, \hat{y}_r)$ . In the expansion region, the volume fraction of small particles is given by

$$\phi = \frac{1}{2} \left[ 1 + \frac{1}{S_r} \frac{\hat{y} - \hat{y}_r}{\xi - \xi_{r1}} \right]. \quad (5.7)$$

As before, this solution is valid until the  $\phi = 1$  characteristic

$$\hat{y} = S_r(\xi - \xi_{r1}) + \hat{y}_r, \quad (5.8)$$

reaches the free surface ( $y = 0$ ) at

$$\xi_{s1} = \xi_{r1} - \hat{y}_r/S_r. \quad (5.9)$$

When this occurs, a shock wave develops and propagates downwards. In these flux coordinates the shock condition is

$$\frac{\partial \hat{y}}{\partial \xi} = S_r(\phi^+ + \phi^- - 1), \quad (5.10)$$

whose form is obvious from considering the original shock condition (3.20). On the forward side of the shock are large particles,  $\phi^+ = 0$ , and on the rearward side, the expansion solution (5.7) defines  $\phi^-$ . Substituting these conditions into (5.10), yields the linear ordinary differential equation

$$\frac{\partial}{\partial \xi}(\hat{y} - \hat{y}_r) - \frac{1}{2} \frac{\hat{y} - \hat{y}_r}{\xi - \xi_{r1}} = -S_r/2. \quad (5.11)$$

Solving (5.11) subject to the condition that the shock starts from  $(\xi_{s1}, 0)$ , implies that the shock is given by

$$\hat{y} - \hat{y}_r = -S_r(\xi - \xi_{r1}) + 2\sqrt{-\hat{y}_r} \sqrt{S_r(\xi - \xi_{r1})}. \quad (5.12)$$

The shock, therefore, reaches the  $\hat{y} = \hat{y}_r$  line at

$$\xi_{r2} = \xi_{r1} - 4\hat{y}_r/S_r, \quad (5.13)$$

where another expansion develops in the return flow. This expansion is centred at  $(\xi_{r2}, \hat{y}_r)$ , with

$$\phi = \frac{1}{2} \left[ 1 + \frac{1}{S_r} \frac{\hat{y} - \hat{y}_r}{\xi - \xi_{r2}} \right]. \quad (5.14)$$

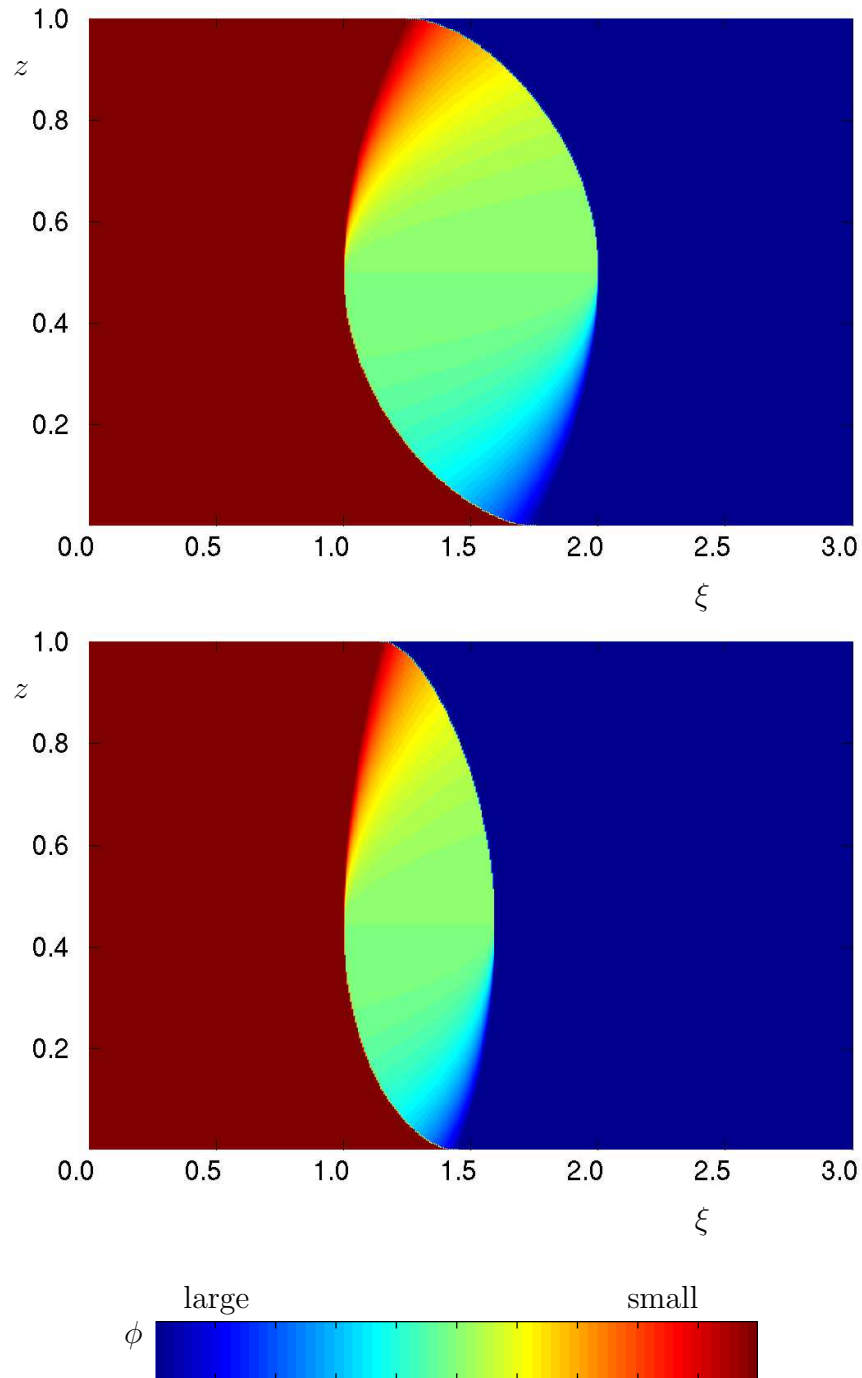


Figure 5.2: Steady-state spatial  $(\xi, z)$  solutions for the concentration of small particles  $\phi$  are shown for a linear (top) and square root (bottom) velocity profiles. In this moving frame of reference the large particles enter from the bottom right and exit through the top right side. Whilst the small particles enter through the top left side and exit through the bottom left side. There are two shocks and two expansion waves which redistribute the particles.

The  $\phi = 0$  propagates downwards along the line

$$\hat{y} = -S_r(\xi - \xi_{r2}) + \hat{y}_r, \quad (5.15)$$

and reaches the basal boundary,  $y = 0$ , at

$$\xi_{s2} = \xi_{r2} + \hat{y}_r/S_r. \quad (5.16)$$

An upward propagating shock is generated from the boundary. Using the shock conditions, with  $\phi^+ = 1$  and  $\phi^-$  given by (5.14), yields the ODE

$$\frac{d}{d\xi}(\hat{y} - \hat{y}_r) + \frac{1}{2} \frac{\hat{y} - \hat{y}_r}{\xi_{r2} - \xi} = S_r/2. \quad (5.17)$$

Solving this linear equation, subject to the condition that it passes through  $(\xi_{s2}, 0)$  implies

$$\hat{y} - \hat{y}_r = -S_r(\xi_{r2} - \xi) + 2\sqrt{-\hat{y}_r}\sqrt{S_r(\xi_{r2} - \xi)}. \quad (5.18)$$

This reaches the  $y = y_r$  line again at

$$\xi = \xi_{r2} + 4y_r/S_r = \xi_{r1}, \quad (5.19)$$

i.e. it meets back at the point where the interface was assumed to start, and a closed solution is obtained. A schematic diagram showing the key points of this solution is illustrated in figure 5.1.

The solution, for both; the linear shear, and the square-root shear profiles, is illustrated in figure 5.2. The structure is the same for both velocity profiles being considered. In both cases  $\xi_{r1}$  has been taken to be 1. The lens is a lot wider in the linear shear case, and in section 5.3, the temporal development to this solution will be numerically investigated.

## 5.2 Particle paths

Differentiating (5.1) gives,

$$\frac{dx^\mu}{dt} = \frac{d\xi^\mu}{dt} + \bar{u}, \quad (5.20)$$

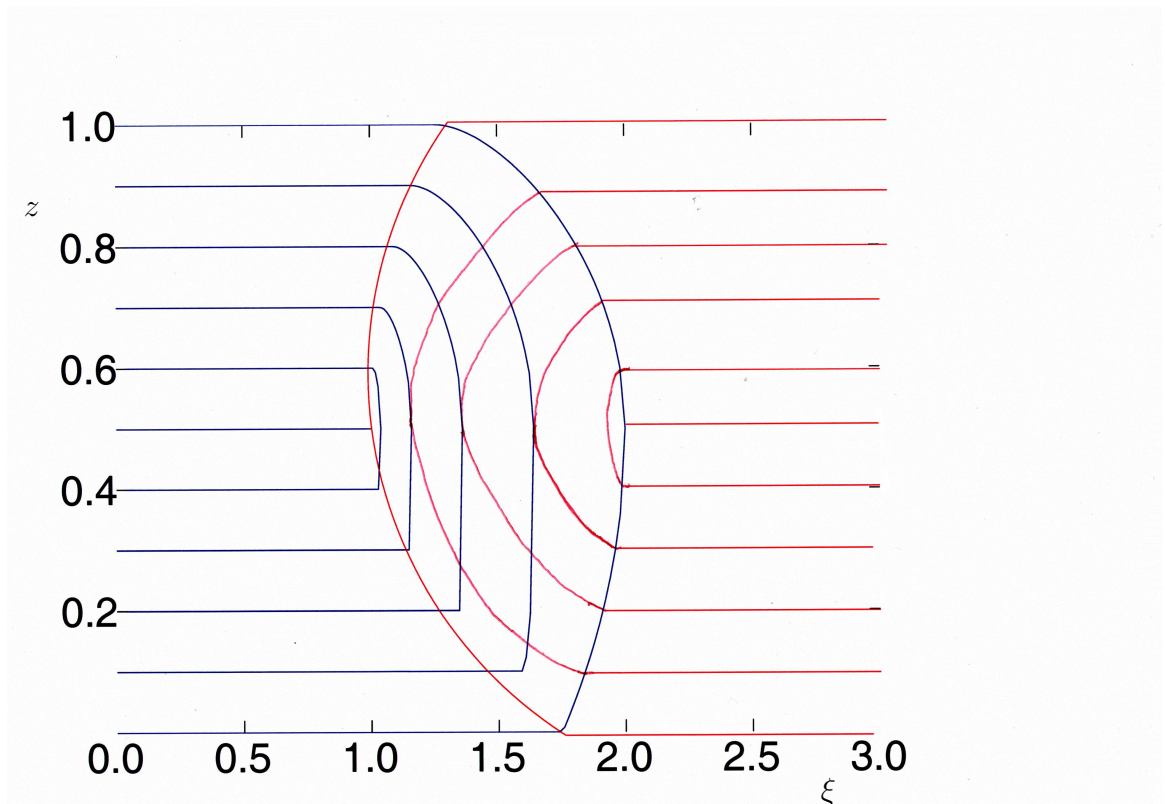


Figure 5.3: Figure showing the particle paths of both the large and small particles for the case of linear shear. As before, the blue lines represent paths of the small particles and the red lines are the large particles. The paths are illustrated for five of each type of particle. The small particles are taken to enter at heights  $z = 0.5, 0.6, 0.7, 0.8, 0.9$  and  $1.0$ , and the large particles enter at heights  $z = 0.0, 0.1, 0.2, 0.3, 0.4$  and  $0.5$ . This highlights the ‘lens’ structure, shown in the top panel of 5.2 and shows how particles filter past each other in the lens, and exit at the same side they enter.

hence, the following results are obtained

$$\frac{d\xi^s}{dt} = \hat{u}, \quad \frac{dz^s}{dt} = S_r(1 - \phi), \quad \frac{d\xi^l}{dt} = \hat{u}, \quad \frac{dz^l}{dt} = -S_r\phi. \quad (5.21)$$

This is analogous to the expression (3.34) from §3.1.7. Eliminating  $t$  in the same manner and expressing in terms of the depth-integrated coordinates, (5.5), reveals

$$\frac{d\hat{y}^s}{d\xi} = -S_r(1 - \phi), \quad \frac{d\hat{y}^l}{d\xi} = S_r\phi. \quad (5.22)$$

Initially, consider a small particle entering the chute from the left hand side at height  $z_0 \geq z_r$ . In transformed coordinates, this will correspond to a height  $y_0$ , which is simply given by applying the transform (5.5) to  $z_0$ . From (5.22) it is clear that the particle will continue to move along at this height, until it enters the upper expansion fan by crossing the line (5.8). This occurs at

$$\xi_e^s = \xi_{r1} + \frac{\hat{y}_0 - \hat{y}_r}{S_r}, \quad (5.23)$$

where  $\hat{y}_r$  is, again, the location of  $z_r$  in depth integrated coordinates. From (5.22) and (5.7), inside the fan, the trajectory is controlled by

$$\frac{d\hat{y}}{d\xi} = -\frac{S_r}{2} \left[ 1 - \frac{1}{S_r} \left( \frac{\hat{y} - \hat{y}_r}{\xi - \xi_{r1}} \right) \right]. \quad (5.24)$$

This is easily solved to give

$$\hat{y} = \hat{y}_r - S_r(\xi - \xi_{r1}) + C\sqrt{\xi - \xi_{r1}} \quad (5.25)$$

and when subject to the entrance condition  $(\hat{y}, \xi) = (\hat{y}_0, \xi_e^s)$  (5.25) gives

$$\hat{y} = \hat{y}_r - S_r(\xi - \xi_{r1}) + 2\sqrt{y_0 - y_r}\sqrt{S_r(\xi - \xi_{r1})}, \quad (5.26)$$

where (5.23) has been used to simplify the expression.

This trajectory will remain valid until the small particles cross the zero bulk velocity line i.e.  $\hat{y} = \hat{y}_r$ . This happens at the point

$$\xi_c^s = \xi_{r1} + \frac{4}{S_r}(\hat{y}_0 - \hat{y}_r). \quad (5.27)$$

Here, the particles leave the top fan (described by (5.7)), and enters the lower fan, whose equation is given by (5.14). This has exactly the same structure as the top fan

with the initiation point moved to  $\xi_{r2}$ , hence, the equation of the trajectories is still given by (5.25) with the identification  $\xi_{r1} \rightarrow \xi_{r2}$ . Applying the boundary condition  $y = y_0$ , when  $\xi = \xi_c^s$ , gives the particle path below the mid-plane as

$$\hat{y} = \hat{y}_r - S_r (\xi - \xi_{r2}) + \sqrt{S_r (\xi - \xi_{r2})} \sqrt{S_r (\xi_c - \xi_{r2})}. \quad (5.28)$$

The small particles remain on this trajectory until they exit the lower fan by crossing the lower shock (given by (5.18)), occurring at

$$\xi_{ex} = \xi_{r2} - \frac{1}{S_r} (\sqrt{-y_r} - \sqrt{-y_0})^2, \quad y = y_0. \quad (5.29)$$

After this they enter a pure phase of their own type, and continue at a constant height until leaving the domain. A similar expression can be obtained for the large particles.

Similar arguments can be used to construct the particle paths for the large particles. The solution for the linear shear is drawn in figure 5.3. As can be seen from this figure, the particles travel along at a constant height until they meet a particle of the opposite type coming the other way. At this point they are forced up/down, depending on whether they are large/small, into the main body of the fan. On passing the zero velocity line their horizontal direction is reversed. Eventually, they filter past all the particles of the opposite type and after this their height again becomes constant. Hence, they flow back out the across the boundary they entered across.

### 5.3 Temporal development

The numerical methods developed in chapter 4 were used to investigate the temporal development of this ‘lens’ solution. The problem of a chute, initially filled with a homogeneous mixture of equal volume fractions will be considered. Again a Courant number of 0.8 will be used with the Superbee limiter. The chute was initially taken to be filled with small particles upto the line  $\xi = 1.5$ , then the rest of the chute was filled with large particles. The mean velocity was taken to be  $\bar{u} = 2z - 1$ , which means that the flow is stationary on the line  $z_r = 0.5$ . At the end of the chute, the material

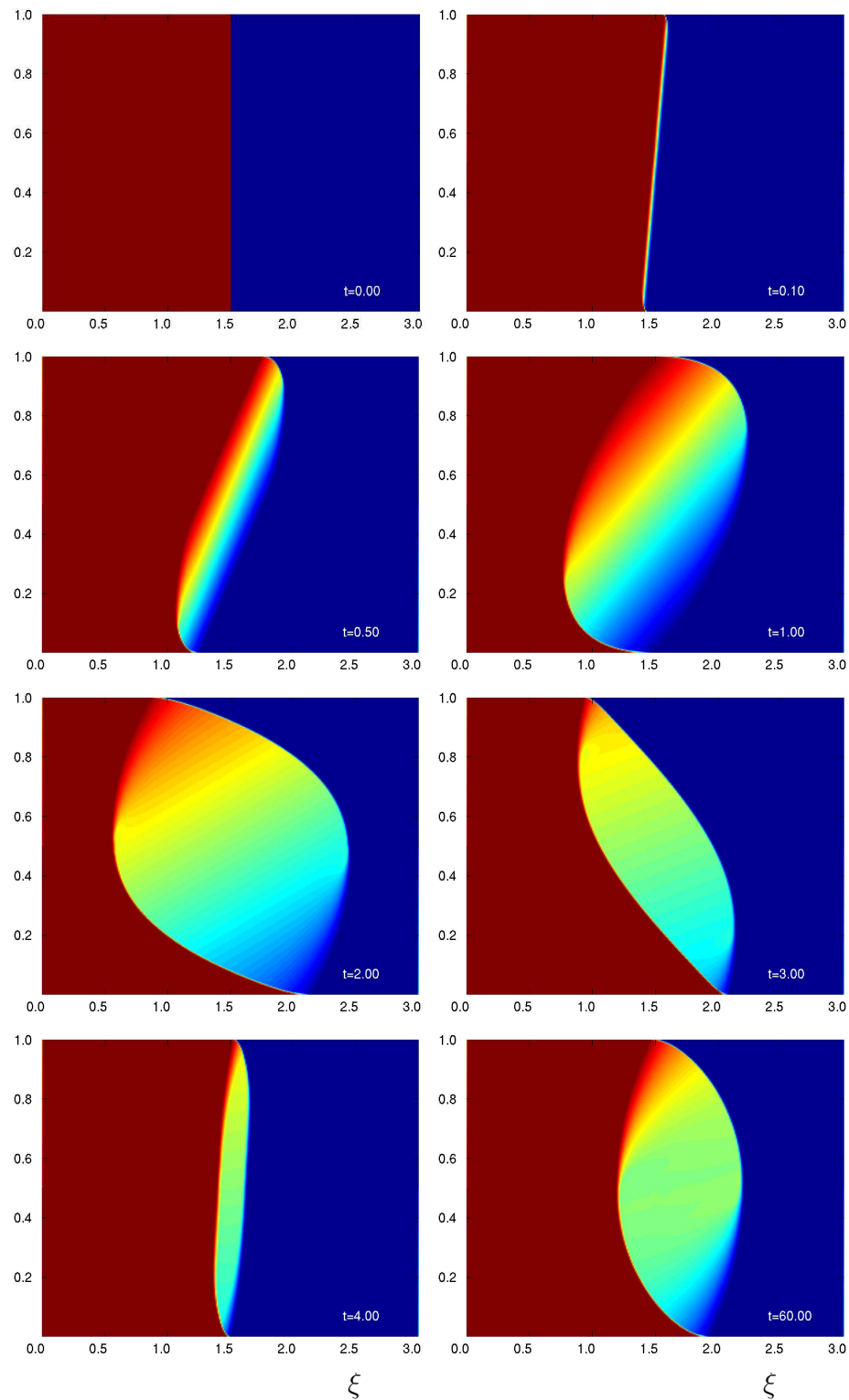


Figure 5.4: Graphs showing the development of the ‘lens solution’ starting from an initially horizontally segregated mixture.  $S_r$  was taken to be 1. The plots are drawn in the centre of mass coordinates and the velocity field was taken to be the linear shearing case, i.e.  $\hat{u} = 2z - 1$ . The chute was initially taken to contain a horizontally segregated solution with the small particles starting behind the large particles. The code was run using a grid of 300 by 300 points and Courant number of 0.8. This solution is seen to develop to the analytical solution discussed in the previous section.

was recirculated back into the chute, i.e. on the left hand edge, material flowing out below the mid-plane was fed back as the inflow condition above the mid-plane, after being reflected about  $z = 0.5$  (and vice versa of the right-hand boundary). This is a very simple model of the recirculation that would occur at each end of a finite mass of flowing material, as it is simply turned over and fed back into the flow.

Figure 5.4 shows the development of this solution. The initially vertical interface deflects due to the shear in the flow, highlighted in the top right panel. This, then, leads to an unstable, stratified (normally graded) solution, hence, segregation starts to take place under this line. The shear in the flow continues to push the interface towards the horizontal and segregation continues to take place. This, then, quickly develops into a ‘lens’ structure ( $t = 1.0$ ), which oscillates wildly around. At times it almost returns to a horizontally segregated state, for example,  $t = 4.0$ . After a long period, (around 50) the oscillations die down, and the solution settles down to precisely the steady-state analytical solution obtained earlier, and shown in the top panel of figure 5.2.

The code was run from numerous different starting conditions, including initially vertical segregated and homogeneously mixed conditions. The same steady-state was achieved in all cases, the only change was the time taken for this to occur. This indicates that this ‘lens’ structure is fundamental to any problem where both shear and particle size variations are apparent. As discussed in the introduction to this chapter, this is almost always the case in real life flows. Therefore, the understanding of this structure, and its development, is the first step in determining the internal structure of many segregating industrial and geophysical flows.

# Chapter 6

## Three Phase Model

### 6.1 Three constituent segregation model

#### 6.1.1 Mixture framework

In this chapter the two constituent theory presented in chapter 2 will be extended to include the effect of allowing the pore space between the grains to be filled with a non-viscous, dense fluid and an additional constant atmospheric pressure that is applied at the free-surface. Hence, the flow will be assumed to be composed of a bi-disperse mixture of large and small particles, but this time the interstitial pore space is filled with a passive fluid. The large particles will be denoted by the superscript ‘ $l$ ’, the small particles by ‘ $s$ ’ and the passive fluid by ‘ $a$ ’. All three constituents must satisfy individual conservation laws for mass,

$$\frac{\partial \rho^\nu}{\partial t} + \nabla \cdot (\rho^\nu \mathbf{u}^\nu) = 0, \quad \nu = (s, l, a), \quad (6.1)$$

and momentum

$$\frac{\partial}{\partial t}(\rho^\nu \mathbf{u}^\nu) + \nabla \cdot (\rho^\nu \mathbf{u}^\nu \otimes \mathbf{u}^\nu) = -\nabla p^\nu + \rho^\nu \mathbf{g} + \boldsymbol{\beta}^\nu, \quad \nu = (s, l, a), \quad (6.2)$$

where it has been anticipated that the stress tensor will also be a hydrostatic pressure field for the fluid phase. The convention that will be adopted means that  $\nu$  represents a quantity defined for all three constituents, i.e.  $\nu = (s, l, a)$  and the constituent letter

$\mu$  will be used for granular only properties i.e.  $\mu = s, l$ . Since, there are three different constituents, the sum of the internal drags, (1.37), takes the more complicated form

$$\beta^l + \beta^s + \beta^a = \mathbf{0}. \quad (6.3)$$

The bulk density,  $\rho$ , and bulk pressure,  $p$ , are defined by the sum of the partial quantities over *all* constituents

$$\rho = \rho^l + \rho^s + \rho^a, \quad p = p^l + p^s + p^a. \quad (6.4)$$

Each constituent occupies a volume fraction  $\Phi^\nu$  per unit mixture volume, and by definition these sum to unity

$$\Phi^l + \Phi^s + \Phi^a = 1. \quad (6.5)$$

It is useful to work with the volume fraction of large and small particles per unit granular volume rather than per unit mixture volume. Since, the volume fraction of grains per unit mixture is

$$\Phi^g = \Phi^l + \Phi^s, \quad (6.6)$$

the volume fractions of large and small particles per unit granular volume are

$$\phi^\mu = \Phi^\mu / \Phi^g, \quad \mu = l, s, \quad (6.7)$$

which also sum to unity

$$\phi^l + \phi^s = 1. \quad (6.8)$$

The relationship between intrinsic and partial pressure can theoretically take any general form, the exact form will be discussed later, where the same idea as in chapter 2, will be exploited.

### 6.1.2 The particle-size segregation model

As the particles avalanche downslope and rearrange themselves during the segregation process, there are small changes in the local volume fraction of the interstitial fluid. For simplicity, the theory presented here assumes that these variations are small

enough to be neglected and that the volume fraction of granular material, and, hence, the volume fraction of the background fluid, is constant

$$\Phi^g = \text{const} \quad \Rightarrow \quad \Phi^a = \text{const}. \quad (6.9)$$

The large and small particles are assumed to have the same constant intrinsic density,  $\rho^{g*}$ , whilst the passive fluid is assumed to have a constant density,  $\rho^{a*}$ , whose value is, in general, different to that of the particles

$$\rho^{l*} = \rho^{s*} = \rho^{g*} = \text{const}, \quad \rho^{a*} = \text{const}. \quad (6.10)$$

These assumptions imply that the bulk density is constant

$$\rho = \Phi^g \rho^{g*} + \Phi^a \rho^{a*} = \text{const}, \quad (6.11)$$

which is a reasonable first approximation in many granular free-surface flows [70]. Equation (6.1) now implies that the fluid velocity field is incompressible  $\nabla \cdot \mathbf{u}^a = 0$ .

The same coordinate system, as used in chapter 2, will also be adopted here, and is illustrated in figure 2.1. Following the same development as before, firstly it is assumed that the normal acceleration terms are negligible, the bulk momentum balance, obtained by summing (6.2) over all constituents, reduces to

$$\frac{dp}{dz} = -\rho g \cos \zeta, \quad (6.12)$$

in the normal direction. Since the right-hand side of (6.12) is constant, the bulk momentum balance may be integrated through the avalanche depth  $h$ , subject to the boundary condition that the pressure is atmospheric at the free-surface,  $p(h) = p_{\text{atm}}$ , to show that the bulk pressure is isostatic

$$p = p_{\text{atm}} + \rho g(h - z) \cos \zeta. \quad (6.13)$$

As demonstrated at the end of chapter 2, the model is crucially dependent on the interaction forces between the constituents and the way in which the bulk pressure is shared out between them. The interstitial fluid is assumed to play a passive role in the theory, interacting only by the surface buoyancy forces that they exert upon the

particles. In standard mixture theory, the overlapping of constituents implies that explicit surface forces are lost. They can, however, be reintroduced by assuming an interaction drag of the form

$$\beta^a = p^{a*} \nabla \Phi^a, \quad (6.14)$$

which combines with the pressure gradient in the momentum balance to yield a buoyancy force  $\Phi^a \nabla p^{a*}$ . It should be pointed out that if the fluid was allowed to flow, it would apply a drag to the granular phase (i.e. the small and large particles combined) proportional to the difference in velocities and the viscosity of the fluid, but in this flow regime these terms will be negligible. A detailed treatment of the problem of a slow fluid moving through a porous matrix can be found in §1.5.1 and the drag for this situation is given by (1.45). Since it has been assumed that the fluid has zero viscosity, the velocity dependent term has been neglected. The partial and intrinsic pressures are related by a linear volume fraction scaling

$$p^a = \Phi^a p^{a*}. \quad (6.15)$$

Substituting (6.14) and (6.15) into the normal component of (6.2) and assuming that the normal acceleration is negligible implies

$$\frac{\partial p^{a*}}{\partial z} = -\rho^{a*} g \cos \zeta. \quad (6.16)$$

This may also be integrated through the avalanche depth  $h$ , subject to the boundary condition that the pressure is atmospheric at the free-surface, to show that the intrinsic fluid pressure is hydrostatic

$$p^{a*} = p_{\text{atm}} + \rho^{a*} g (h - z) \cos \zeta. \quad (6.17)$$

The fluid pressure is transmitted through the entire matrix by surface pressure interaction forces. It follows that the remaining overburden pressure due to particle-particle contacts is

$$p^{g*} = p - p^{a*}, \quad (6.18)$$

or using (6.13) and (6.17)

$$p^{g*} = (\rho - \rho^{a*}) g (h - z) \cos \zeta. \quad (6.19)$$

The partial pressure in the grains, therefore, consists of a pressure due to the surrounding fluid, plus a share of the overburden pressure, which will be taken in the same form as before,

$$p^\mu = \Phi^\mu p^{a*} + f^\mu p^{g*}, \quad \mu = l, s \quad (6.20)$$

where the factor  $f^\mu$  determines the relative proportion of the overburden pressure carried by constituents  $\mu = l, s$ , (see chapter 2). Note, the linear volume fraction scaling  $\Phi^\nu$  for the fluid pressure ensures that the particles obey Archimedes' principle.

The drag due to the inter-particle friction, as the particles rub past one another, will take the same form as before, but will now have an additional term, due to the fluid, which can be thought of as the reaction to (6.14). Hence, the drag of the granular constituents will be of the form

$$\boldsymbol{\beta}^\mu = p^{a*} \nabla \Phi^\mu + p^{g*} \nabla f^\mu - \rho^\mu c (\mathbf{u}^\mu - \mathbf{u}), \quad \mu = l, s, \quad (6.21)$$

and this time  $\mathbf{u}$  is the barycentric granular velocity

$$\mathbf{u} = \phi^l \mathbf{u}^l + \phi^s \mathbf{u}^s. \quad (6.22)$$

The first two terms on the right-hand-side of (6.22) combine with the partial pressure gradient term in the momentum balance (6.2) to yield intrinsic rather than partial pressure gradients, in the same way as Darcy's law for fluid flow through porous materials. The third term provides the resistance to relative motion. Note, that the internal interaction forces (6.14) and (6.22) and the pressure relations (6.17) and (6.19) have been constructed in such a way that they automatically satisfy the summation conditions (1.37) and (1.40).

The large and small velocities in the cross- and down-slope direction are assumed to be the same as the bulk component, i.e. as in (2.18). An equation for the percolation velocities in the normal direction is obtained by substituting the partial/intrinsic pressure law (6.21), the interaction drag (6.21) and the pressure relations (6.13) and (6.17), into the normal component of (6.2) to give

$$\phi^\mu w^\mu = \phi^\mu w + (f^\mu - \phi^\mu) (\hat{\rho} g / c) \cos \zeta, \quad \mu = l, s, \quad (6.23)$$

where the relative density difference is given by

$$\hat{\rho} = \frac{\rho^{g*} - \rho^{a*}}{\rho^{g*}}. \quad (6.24)$$

A comparison with the binary mixture theory of chapter 2 shows that the percolation equation (6.24) contains an additional factor  $\hat{\rho}$  to account for the presence of the interstitial fluid. The simple two-constituent theory of chapter 2 can be recovered by assuming that the density of the interstitial fluid,  $\rho^{a*}$ , equals zero, so that  $\hat{\rho} = 1$ . Physically, the addition of the passive fluid creates a buoyancy force on all the grains, which reduces the contact forces between them. In particular, if the density of the fluid is matched to the density of the particles to create a neutrally buoyant suspension with  $\hat{\rho} = 0$ , then (6.23) predicts that there will be no segregation due to kinetic sieving. This is in agreement with experimental observations of [85], which will be discussed in §6.2.

The final elements of the segregation model are the non-linear pressure scalings,  $f^\mu$ , which determine how the overburden pressure,  $p^{g*}$ , is shared between the large and small particles. The same forms as in chapter 2 will be assumed, i.e. those given by equation (2.23). Substitution of these results into (6.23) gives

$$\begin{aligned} w^l - w &= +q\phi^s, \\ w^s - w &= -q\phi^l, \end{aligned} \quad (6.25)$$

where the mean segregation velocity is

$$q = (B/c)\hat{\rho}g \cos \zeta. \quad (6.26)$$

An equation for the volume fraction of small particles is obtained by substituting (6.25) into the mass balance (6.1) to give

$$\frac{\partial \phi^s}{\partial t} + \frac{\partial}{\partial x}(\phi^s u) + \frac{\partial}{\partial y}(\phi^s v) + \frac{\partial}{\partial z}(\phi^s w) - \frac{\partial}{\partial z}(q\phi^s \phi^l) = 0. \quad (6.27)$$

These are similar to the expressions derived in chapter 2, except the relative density difference,  $\hat{\rho}$ , now enters the segregation velocity (6.26). If  $\hat{\rho} > 0$ , the small particles percolate down at a rate proportional to the volume fraction of large particles, until 100% concentration of small particles is reached. Meanwhile, the large particles move

up until they also reach 100% concentration. The particles, therefore, segregate into inversely graded layers as anticipated. A key prediction of this extended theory is that if the particles are neutrally buoyant, i.e.  $\hat{\rho} = 0$ , then no kinetic sieving will occur. Furthermore, if the relative density difference is negative,  $\hat{\rho} < 0$ , the particles are buoyant and the direction of segregation is reversed. The small particles will, therefore, percolate upwards, and the large grains downwards, to form *normally graded* layers.

### 6.1.3 The non-dimensional segregation equation

The equation will be non-dimensionalised using the scalings in (2.32). Substituting these scalings into (6.27), and dropping the tildes on the avalanche variables and the superscript  $s$ , for simplicity, the non-dimensional segregation equation for the small particles becomes

$$\frac{\partial \phi}{\partial t} + \frac{\partial}{\partial x}(\phi u) + \frac{\partial}{\partial y}(\phi v) + \frac{\partial}{\partial z}(\phi w) - S_r \frac{\partial}{\partial z}(\phi(1 - \phi)) = 0, \quad (6.28)$$

where the non-dimensional segregation number is given by

$$S_r = \frac{LB\hat{\rho}g \cos \zeta}{cHU}. \quad (6.29)$$

It clear that this is exactly the same equation as (2.33) with a slightly modified definition of the non-dimensional segregation number (6.29), compared to (2.34). This implies that, all the analytical and numerical solutions obtained in the previous two chapters are still valid for the three phase case.

## 6.2 Comparison with experiments

In §3.1.5 it was shown that the exact solutions were in good agreement with the dry granular segregation experiments of [72] and [85]. Experiments with liquid particle mixtures were also performed by Vallance and Savage [85]. They used a bi-disperse mixture of 1.44 mm large and 0.99 mm small glass particles of density  $\rho^{g*} = 2.49 \text{ g/cm}^3$ , which were mixed in a water and a water-ethanol mixture, whose

	Liquid	Viscosity (centipoise)	Fluid density $\rho^{a*}$ (g/cm <sup>3</sup> )	Relative density difference $\hat{\rho}$
1)	Water	1.0	1.00	0.59
2)	Water-ethanol mixture	3.7	0.94	0.62

Table 6.1: Summary of the properties of the different interstitial fluids used in the liquid-particle segregation experiments of [85].

properties are summarised in table 6.1. The mass flux was regulated to generate a steady uniform flow of depth 0.9cm to 1.5 cm on slopes ranging from 22° to 12.3°, which developed a uniform solids fraction once the initial flow front had propagated through the system. Splits were taken at three different levels in the flows to determine the degree of segregation at four downstream stations. They found that segregation took place, but that it was not as “dramatic as in the dry granular flows” and they summarized that the presence of a viscous fluid inhibited kinetic sieving. Curiously, they found that the segregation was slightly weaker in water than in the water-ethanol mixture, which was 3.7 times more viscous. This contradicted their initial hypothesis that it was due to viscosity and they suggested that this might instead be due to the density contrast between the particles and the fluid. In their experimental setup the fluid moves with the same velocity as the barycentric granular velocity, therefore, from the argument used to justify the form of (6.14), the viscosity of the fluid should play no role in the segregation distance. Hence, the theory presented in this thesis confirms the latter hypothesis. From chapter 2, the segregation distance is  $x_p = 1/S_r$ . It follows that the ratio of the segregation distances is

$$\frac{x_{p1}}{x_{p2}} = \frac{S_{r2}}{S_{r1}} = \frac{\hat{\rho}_2}{\hat{\rho}_1} \simeq 1.04, \quad (6.30)$$

where the subscript 1 is used for water and the subscript 2 for the water-ethanol mixture. Hence, the segregation distance in water is 4% longer than in the slightly less dense water ethanol mixture, as observed. The buoyancy induced by the interstitial fluid is, therefore, more important than the effects of viscosity in these high solids fraction experiments. Vallance & Savage [85] also investigated segregation in neutrally buoyant fluids. However, they concluded that “there is very little evidence of size

segregation in flows where the fluid and the particles have exactly the same density”, as the downstream concentrations of small particles stayed at the inflow concentration to within the level of accuracy of the experiments. This is also consistent with the model derived here. When the particles and the fluid have the same density, the relative density difference,  $\hat{\rho} = 0$ , and the segregation length therefore tend to infinity. As far as the author is aware, no experiments have been performed with buoyant particles to date, but the theory predicts that the direction of segregation will reverse to create normally graded layers.

# Chapter 7

## Experimental Work

The main thrust of the thesis has been to develop a theoretical model of particle size segregation in shallow granular free-surface flows. A numerical method was then developed to compute solutions to this model. Towards the end of this thesis some simple preliminary experiments were performed with the aim of verifying the theory. These experiment and their results are briefly reviewed in this chapter.

### 7.1 Measuring the Densities of Granular Material

In the experiments contained in this section four different materials will be used: sand, glass of two different sizes and 100's and 1000's (sugar particles). The properties of these materials need to be determined. The density was calculated by filling a measuring cylinder with 100 ml of water, to which a known mass of material was added and the increase in the fluid volume was then recorded. This process was continued until the granular material was no longer saturated. This experiment was repeated several times for each material. For each data set a graph of increase in volume against mass added was plotted and the gradient used to determine the density.

As the cylinder began to fill it was shaken to repack the material so that more could be added. This was not possible with the sugar as it started to dissolve due to the agitation. This was apparent due to the change in the colour of the water and

Material	Density (in grams/milli litre)	Diameter (in mm)
Sugar	$1.2401 \pm 0.0022$	$1.5165 \pm 0.1093$
Sand	$2.6187 \pm 0.0433$	
Glass (Coarse)	$2.4913 \pm 0.0069$	$0.7180 \pm 0.0861$
Glass (fine)	$2.4697 \pm 0.0061$	

Table 7.1: Table showing the measured densities and sizes of the materials used in laboratory experiments

a slight curve in the density verses added mass graphs, indicating that some of the mass was not contributing to a volume increase.

The results of the measurements are summarised in table 7.1. The two different types of glass vary slightly in density with the coarse glass being 0.8% denser. The small variation of the glass densities do not lie within one standard deviation of each other and is likely to be due to production differences between the two different batches of glass. The sand was found to be 5.1%/6.0% denser than the coarse/fine glass respectively. Whereas the sugar particles are only 49.8%/50.2% the density of the coarse/fine glass respectively.

## 7.2 Measuring the Particle Size Distribution

For the larger materials (i.e. the sugar particles and the coarse glass) the size was measured using a micrometer. This has a range of 0-25 mm in gradations of 0.01 mm. For both sets of particles a sample of material was removed and from this sample 40 particles were selected at random. The experimentally determined mean and standard deviation are summarised in table 7.1. From this it is clear that the ratio of the mean diameters of these two particles is 2.11, which corresponds to a volume ratio of 9.42.

Figure 7.1 shows the distribution in sizes of both the sugar and the coarse glass particles. From here it is evident that there is very little variation in particle sizes and the distributions do not overlap. The interquartile range for the glass/sugar particles are 0.132 mm/0.07 mm respectively, illustrating a higher variation in size is present

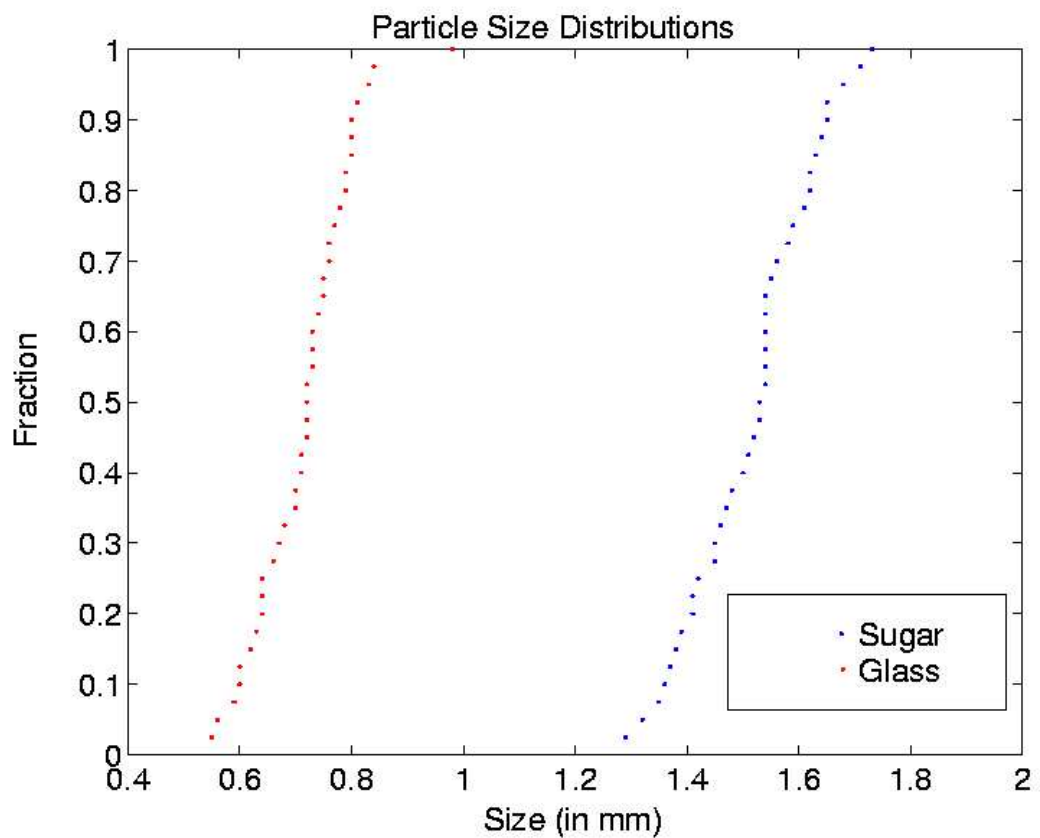


Figure 7.1: Graph showing the measured size distribution for both the coarse glass (blue dots) and the sugar particles (red dots). The sugar particles were found to have a mean of 1.52 mm with a standard deviation of 0.11 mm, whereas the glass has a mean of 0.72 mm with a standard deviation of 0.09 mm

in the glass particles. This larger variation in size is also highlighted by the fact that the glass standard deviation is a higher percentage of its mean value than the sugar.

### 7.3 Segregation in Chute Flows

The sugar and coarse glass were used to reproduce the experimental results of Savage & Lun [72]. As indicated by the results in §7.1 the glass is twice the density of the sugar particles, which will obviously aid the segregation process. This sugar was used because it is cheap and easy to obtain in many different colours. The idea was to film the flow through the side-walls and use image processing techniques to obtain more detailed information about the segregation. Granular chute flows slip at the sidewall and, consequently, show very weak variation across the chute, provided that the flow velocity does not exceed  $5 \text{ ms}^{-1}$  (a speed that is, in fact, very hard to achieve in small scale experiments). This has been confirmed by a series of Particle Image Velocimetry measurements at the surface, base and sidewalls of a mono-disperse chute flow, [25]. In addition, by making surface and sidewall particle tracking measurements and considering the global mass flux, Courrech du Pont *et al.*, [24], have shown that the velocity profile with depth at the centre of the flow is self-similar to the wall profile.

A perspex chute that was 5.1 cm wide and 148 cm long was used. Segregation was easy to observe without any need to roughen the base of the flow. The aim was to use a combination of splitter plates and this new method of filming through the side wall to check the methods are consistent and the results match. If this was the case, then it was intended to use the new method with two different types of glass. This was not possible in the time available, but it is hoped this will be able to be done in the near future as this would give great insight into the problem. The code was developed and a series of videos of strongly segregating flows were produced.

In figure 7.2, a selection of stills from a slightly different set of experiments are shown. Rather than connecting splitter plates at the end of the chute, a fixed end was inserted. When the material reaches the end it collides with this and generates a shock

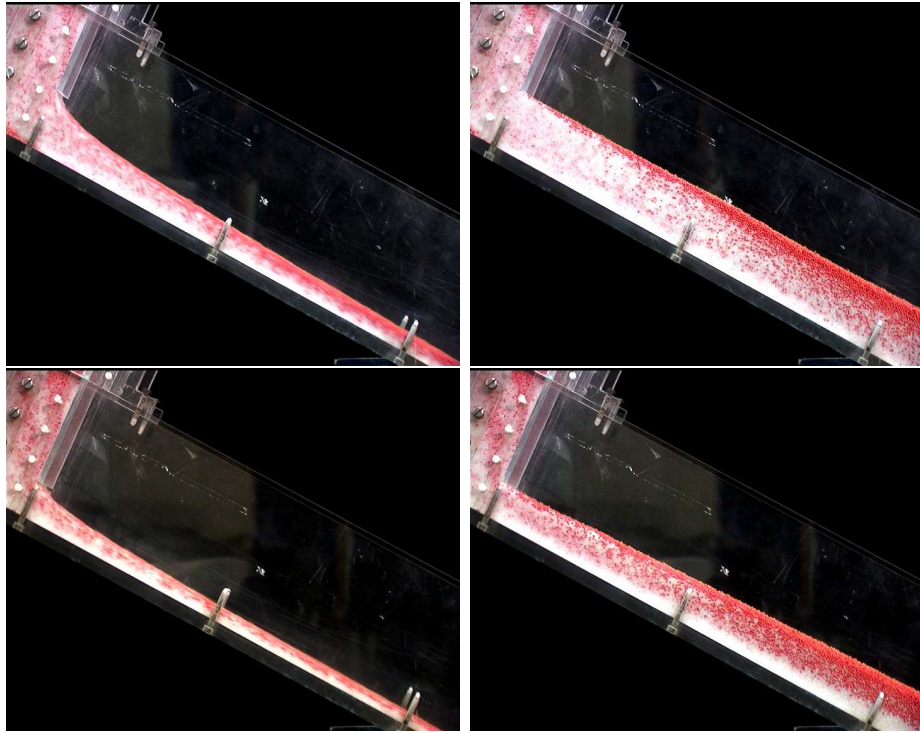


Figure 7.2: A series of shots from experiments of a mixture of sugar and coarse glass down an inclined plane. The chute is made of perspex and it is 5.1 cm wide and 148 cm long with an incline of 26 degrees to the horizontal. The end of the chute was closed and hence a shock wave is generated when the material reaches the bottom. This shock propagates up the chute until reaching the hopper. As the shock passes, the depth of the flow is seen to increase in thickness. The images on the left hand-side show the material flowing before the bottom has been reached and generated a shock wave. The images on the right are for the final deposit once the flow has come to rest. The top panels are for a gate height (initial depth) of 5 cm and the bottom panels 3 cm. The material used is a 50 % by volume fraction of sugar (red) and coarse glass (white), the properties of this material are summarized in table 7.1. The screws from the base of the chute into the side walls are 18 cm apart.

wave that propagates back up the chute until reaching the hopper. In both the final deposit and flowing shots, it is possible to determine three regions, one of purely sugar (red) particles, another of glass (white) particles and a mixed region between. In the lower panel (3 cm case) it is clear that full segregation has taken place immediately after the first screw and from this point onwards the red particles are found to lie on top of the white particles. For the 5cm case (top panels), full segregation occurs just after end of the picture. This is in line with the linear increase in segregation length, with depth, predicted by the dimensionless parameter  $S_r$  i.e. (2.34). This is by no means conclusive and considerably more experimental work needs to be performed to test this and other aspects of the model. Additionally by watching the movies in full, the boundaries of the different domains are seen to move slightly with time. This is due to small a variation  $\phi$  at the inflow point, and was the main motivation for considering the effect of time dependent inflow in both chapters 3 and 4.

This freezing of the deposit, after the shock wave has passed, is what leads to the stratified deposits often observed in geophysical flows [62, 28, 11]. These occur when periodic avalanching of material takes place, each burst of material adds an extra set of stripes to the surface and the deposit is built-up. Far from the initialisation point, the deposit consists of consecutive stripes of different size material, as observed in geological flows. A theory for the build-up of these stratification patterns can be found in [33, 34], where it is assumed that the material segregates immediately on entering the avalanching layer. By coupling this with the model of segregation presented in chapter 2 the full problem, including the prediction of the pattern near the source, could now be accomplished.

A close inspection of the images in figure 7.2 show that the flow does strain (thin) slightly as it leaves the hopper. This occurs when the angle of inclination of the chute is different to the angle of friction of the material under consideration. Numerical simulations were performed that took account of this straining effect and it was shown that it did not alter the segregation length.

It is hoped that at sometime in the near future this technique will be fully developed and applied to these flows. Additionally, it would be interesting to investigate

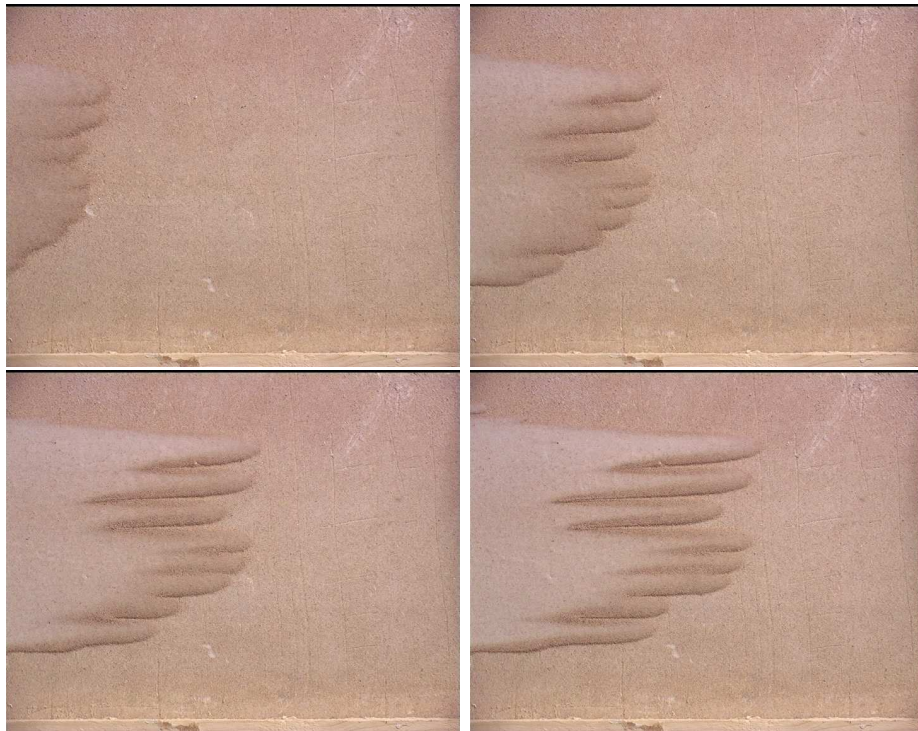


Figure 7.3: Above are a sequence of stills from a video of a mixture of sand and fine glass flowing down a rough incline, whose properties are summarised in table 7.1. The sand accounts for 14% of the material by volume. The flow is from left to right. The chute is 1.2 metres long and 0.6 metres wide and was roughened by glueing the sand to its surface. It was inclined at an angle of 30 degrees to the horizontal.

the case of normally graded inflow condition and see if these results match with the predictions contained in this thesis.

## 7.4 Fingering Instability

Additional to the chute flow experiments discussed in the previous section, provisional experiments were performed on a wider chute (1.2 metres) with a mixture of sand and the fine glass. The aim of this was to gain an understanding of the key ingredients in the phenomenon of fingering (see [67, 68]). Providing insight into how the theory presented in this thesis could be coupled with the avalanche models (see section §1.2), to fully describe this problem. The coupled problem would allow the study of feedback from the segregation process to the bulk flow, which would be done by allowing

the friction coefficient to depend of the volume fraction of the individual constituents.

It has been found that only a very small percentage of the rougher large grained sand was required to produce strong fingering effects. It was not possible to develop these experiments further, but in figure 7.3 a series of images with 14% sand mixture can be seen. Here, structures very similar to ones observed in many different types of geophysical deposits are observed [62, 28, 11]. In figure 7.3 a uniform front is seen to break down into several fingers, which continue to subdivide further. In the final image (bottom right) it is very clear that there is segregation occurring within each individual finger. The orange sand is seen to have moved to the outer edge, and hence, forms a channel for the finer white glass. The glass pushes the slower moving sand from behind, helping to construct and extend the channels. These channels have the feedback effect of confining the glass and reducing lateral spreading, hence creating vastly increased run-out distances.

This experiment was repeated a number of times and the phenomenon was found to be very robust and easy to reproduce. The exact pattern was highly dependent on the initial conditions and method of triggering, but the general features were always the same. To form the pattern, a small amount of sand was required and the maximum number of fingers were produced with glass rich flows.

# Chapter 8

## Conclusions

This thesis begins by using a binary mixture theory to derive a simple kinetic sieving model for the segregation of small and large particles in shallow granular avalanches. The model reduces to a single first-order quasi-linear conservation equation (2.25) for the volume fraction of small particles. In order to solve it, the bulk velocity field in a shallow three-dimensional, incompressible, granular free-surface flow, must either be prescribed, or computed using existing avalanche models (e.g. [41, 55, 26, 70, 71, 40, 38]). A significant advantage of this theory is that the segregation velocity is explicitly dependent on gravity. This sets an orientation for the direction of segregation, and ensures that there is no segregation in the absence of gravity.

Exact steady-state concentration solutions have been derived for general steady uniform velocity fields, by using a concentration jump condition (3.18), and a coordinate mapping (3.10). For homogeneous inflow, all solutions consist of three shocks that separate the inflowing mixture from pure phases of the large and small particles. Sufficiently far downstream complete segregation occurs, and an inversely-graded layer is obtained, with the large particles separated from the small ones beneath by a concentration jump. These solutions are in close agreement with Savage & Lun's [72] original laboratory experiments, as well as those of Vallance & Savage [85]. Exact steady-state solutions have been constructed for a discontinuous, normally graded inflow condition with general steady uniform velocity fields. These show the formation of expansion fans, concentration shocks, and inversely-graded, completely segregated

layers, sufficiently far downstream. The distance for complete segregation to occur is inversely proportional to the segregation number,  $S_r$ , and is dependent on the inflow discontinuity height,  $z_r$ . This is in marked contrast to the homogeneous inflow solutions, which were only dependent on  $S_r$ .

The model developed in chapter 2 was then extended to include the effect of a non-viscous pore fluid, again, using the framework of mixture theory. This allows buoyancy effects to be incorporated into the final segregation equation (6.27), and represents a significant extension of the simple two-phase theory of chapter 2. As the density of the interstitial fluid is increased, the relative density difference,  $\hat{\rho}$ , decreases, therefore,  $S_r$  decreases and complete segregation occurs further downstream. If the density of the fluid and the grains match, then segregation by kinetic sieving is inhibited altogether. This is in agreement with the experiments of Vallance & Savage [85], but it should be noted that segregation in other, more energetic, systems may occur in the absence of gravity, due to spatial gradients in the energy of the granular velocity fluctuations (e.g. [59, 52]). If the relative density difference,  $\hat{\rho}$ , changes sign, such that, the particles are buoyant, the direction of segregation is reversed and normally graded layers will be formed, sufficiently far downstream.

Fully time-dependent solutions have also been constructed for the plug-flow regime, by exploiting the decoupling of material columns as they are advected downstream. These solutions yield considerable insight into segregation in geophysical flows, where there is strong slip at the base.

The shock-capturing modified-TVDF method can be used to compute solutions to the dimensionless segregation equation (2.33) with any incompressible three-dimensional velocity field, and for general initial and boundary conditions. This has been used to compute the evolution of the small particle concentration, with strong shear, in two space dimensions. Many of the flow features can be explained with the insight gained from some simple exact solutions for plug-flow, which exploit the decoupling of material columns, in the absence of downslope velocity gradients through the avalanche depth. Essentially, the solutions consist of a downstream region, where the uniformity of the initial conditions implies that the solution is exactly that predicted

by plug flow, and a steady-state upstream region. The two of which are separated by an evolving transition zone that propagates downslope with increasing time. The dynamics of the transition regions are extremely complex, with the development of unsteady propagating shocks and expansion fans. It will, therefore, be of great use in calculating numerical solutions to more general problems in the future. However, the system is suitably robust to suggest that the segregation equation (2.33) may be coupled to existing models for dry granular free-surface flows, to compute the development of the particle size distribution, and allow feedback onto the flow. In particular, the inclusion of a passive fluid now allows the model to be incorporated into water saturated, debris-flow models, such as those of Iverson [48] and Iverson & Denlinger [46].

A small number of experiments was carried out on both the coupling with the bulk flow, and testing the simple analytic solutions for homogeneous inflow. The experiments were qualitative in their nature and can be used as the ground-work to produce more sophisticated quantitative experiments in the near future. The results that were obtained are consistent both with the original experiments of Savage & Lun [72], and the analytical results.

Finally, the wave breaking problem was investigated by considering a finite mass of material flowing down a chute, with a very simple velocity profile. This investigation led to a discovery of an analytic, stable ‘lens’ solution, which appears in many of the numerical results of chapter 4. This solution consists of both, two expansion fans, and two curved shocks, and gives some insight into the structure of geological debris flows, where a similar concentration profile is often observed.

The original model with homogeneous solutions has been published in [39] and the extended model and normal-graded inflow solutions can be found in [80]. Extended time-dependent analytic solutions can be found in [73] and [35].

# Bibliography

- [1] *PM 2004 World Congress*, 2004. *Published in* Powder Metallurgy, Volume 47, Number 4, pages 309-312, 2004.
- [2] Micheal B. Abbott. *An Introduction to The Method of Characteristics*. Thames and Hudson, London, 1966.
- [3] M Abramowitz and I Stegun. *Handbook of mathematical functions*. Dover Publishing Inc. New York, 9th edition, 1970.
- [4] R.A. Bagnold. Experiments on a gravity-free dispersion of large spheres in a newtonian fluid under shear. *Proc. Roy. Soc. A*, 255:49–63, 1954.
- [5] A.A. Barmin, A.G. Kulilovskiy, and N.V. Pogorelov. Shock-capturing approach and nonevolutionary solutions in magnetohydrodynamics. *JCP*, 126:77–90, 1996.
- [6] Jacob Bear. *Dynamics of Fluids in Porous Media*. 1972.
- [7] Alberto Bressan. *Hyperbolic Systems of Conservation Laws : The One-Dimensional Cauchy Problem*. Oxford University Press, 2000.
- [8] J Bridgewater. Fundamental powder mixing mechanisms. *Power Tech.*, 15:215–236, 1976.
- [9] J Bridgewater, H.H Cooke, and A.M. Scott. Segregation induced instabilities of granular fronts. *Trans. Instn. Chem. Engrs.*, pages 157–167, 1978.
- [10] C.B. Brown. The use of maximum entropy in the characterization of granular media. In S.C. Cowin and M. Satake, editors, *Proc. US-Japan Seminar on*

*Continuum Mechanics and Statistical Approaches in the Mechanics of Granular Media*, pages 98–108, 1978.

- [11] Calder, Sparks, and Gardweg. Erosion, transport and segregation of pumice and lithic clasts in pyroclastic flows inferred from ignimbrite at Lascar volcano, Chile. *J. Volcan. and Geotherm. Res.*, 104:553–566, 2000.
- [12] Y.H. Cao, K Chen, and J Wang. Analyses on duct tail rotor and airfoil aerodynamics characteristics with cfd. *Aircraft engineering and aerospace technology*, 77(1):62–67.
- [13] Bernardo Cockburn, San-Yih Lin, and Chi-Wang Shu. Tvb runge-kutta local projection discontinuous galerkin finite element method for conservation laws iii: one-dimensional systems. *JCP*, 84:90–113, 1988.
- [14] M.H. Cooke, D.J. Stephens, and J. Bridgewater. Powder mixing - a literature survey. *Powder Tech.*, 15(1):1–20, 1976.
- [15] R. Courant, K.O. Friedrichs, and H. Lewy. Über die partiellen differenzgleichungen der mathematischen physik. *Math. Ann.*, 100(32-74), 1928.
- [16] R. Courant, K.O. Friedrichs, and H. Lewy. On the partial difference equation of mathematical physics. *IBM J.*, 11(215-234), 1967.
- [17] H Darcy. The public fountains of the city of bijon experience and application principles to follow and formulas to be used on the question of the distribution of water. Technical report, Inspector general of bridges and highways, 1856.
- [18] Roger P Denlinger and Richard M. Iverson. Granular avalanches across irregular three-dimensional terrain : 1. theory and computation. *Journal of Geophysical Research*, 109, 2004.
- [19] R.P Denlinger and R.M. Iverson. Flow of variably fluidized granular masses across three-dimensional terrain 2. numerical predictions and experimental tests. *Journal Geo. Res.*, 106(B1):533–566, 2001.

- [20] J.D. Dent, K.J. Burrell, D.S. Schmidt, E.E. Louge, M.Y. and Adams, and T.G. Jazbutis. Density, velocity and friction measurements in a dry-snow avalanche. *Annal. Glac.*, 26:247–252, 1988.
- [21] V.N. Dolgunin and A.A. Ukolov. Segregation modelling of particle rapid gravity flow. *Oiwder Tech.*, 26:95–103, 1995.
- [22] G Dong, B.C. Fan, B Xie, and J.F. Ye. Experimental investigation and numerical validation of explosion suppression by inert particles in large-scale duct. *Proc. of teh Combustion Institute*, 30:2361–2368, 2005.
- [23] J.A Drahun and J. Bridgwater. The mechanisms of free surface segregation. *Powder Technology*, 36:39–53, 1983.
- [24] S.C. du Pont, R Fischer, P Gondret, B Perrin, and M Rabaud. Instantaneous velocity profiles during granular avalanches. *P.R.L.*, 94(4), 2005.
- [25] Eckart, Gray, and Hutter. Particle image velocimetry (piv) for granular avalanches on inclined planes. In *Lecture Notes in Applied & Computational Mechanics*.
- [26] M. E. Eglit. Some mathematical models of snow avalanches. In M. Shahinpoor, editor, *Advances in mechanics and the flow of granular materials*, number 2, pages 577–588. Clausthal-Zellerfeld and Gulf Publishing Company, 1983.
- [27] Ehrichs, Jaeger, Karczmar, Knight, Kuperman, and Nagel. Granular convection observed by magnetic-resonance-imaging. *Science*, 267(5204):1632–1634, 1995.
- [28] Fineberg. From cinderella’s dilemma to rock slides. *Nature*, 386:323–324, 1997.
- [29] A Gajo and B Loret. Transient analysis of ionic replacement in elastic-plastic expansive clays. *International Journal of Solids and Structures*, 41(26):7493–7531, 2004.
- [30] P.R Garabedian. *PDE’s*. Ams Chelsea publishing, 1998.

- [31] E Godlevski and P.A. Raviart. *Numerical approximation of hyperbolic systems of conservation laws*. series on Applied Mathematical Sciences 118. Springer, 1996.
- [32] S Godunov. A finite difference scheme for numerical computation of the discontinuous wave solutions of equations of fluid dynamics. *Math. Sb.*, 47:271–306, 1959.
- [33] Gray and Tai. Particle size segregation, granular shocks and stratification patterns. In Herrmann et al, editor, *Physics of dry granular media*, NATO ASI, pages 697–702. Kluwer Academic, 1998.
- [34] Gray, Tai, and Hutter. Shock waves and particle size segregation in shallow granular flows. In Rosato et al, editor, *IUTAM Symposium on segregation in granular materials*, pages 269–276. Kluwer, 2000.
- [35] J. M. N. T. Gray, M. Shearer, and A. R. Thornton. Time-dependent solution for particle-size segregation in shallow granular avalanches. Submitted to Proc Royal Soc.
- [36] J.M.N.T. Gray. Granular flow in partially filled slowly rotating drums. *JFM*, 44:1–29, 2001.
- [37] J.M.N.T Gray and L.W. Morland. A two-dimensional model for the dynamics of sea ice. *Philosophical transactions of the Royal Society of London series A - Mathematical physical and engineering sciences*, 347(1682):219–290, 1994.
- [38] J.M.N.T. Gray, Y.-C. Tai, and S. Noelle. Shock waves, dead-zones and particle-free regions in rapid granular free surface flows. *JFM*, 491:161–181, 2003.
- [39] J.M.N.T. Gray and A.R. Thornton. A theory for particle size segregation in shallow granular free-surface flows. *Proc. Royal Soc. A*, 461:1447–1473, 2005.
- [40] J.M.N.T. Gray, M. Wieland, and Hutter K. Free surface flow of cohesionless granular avalanches over complex basal topography. *Proc. Roy. Soc. A*, 455:1841–1874, 1999.

- [41] Grigorian, Eglit, and Iakimov. New statement and solution of the problem of the motion of snow avalanches. In *Snow, avalanches and Glaciers Tr Vysokogornogo Geofizich Inst.*, volume 12. 1967.
- [42] D Hahn and D Drikakis. Large eddy simulation of compressible turbulence using high-resolution methods. *Internation journal for numerical methods in fluids*, 47(971-977), 2005.
- [43] Ami Harten. High resolution schemes for hyperbolic conservation laws. *Journal of Computational Physics*, 49:357–393, 1983.
- [44] K.M. Hill and J Kakalios. Reversible axial segregation of binary mixtures of granular materials. *Phys. Rev. E*, 49(5), 1994.
- [45] R. Iverson. The debris-flow rheology myth. In Debris-flow hazards havards mitigation: Mechanics, prediction and assessment *Rickenmann and Chen, editors*, pages 303–314. Millpress, 2003.
- [46] R. Iverson and R. Denlinger. Journal of geo. res. *Flow of variably fluidized granular masses across three-dimensional terrain 1. Coulomb mixture theory*, 106(B1):553–566, 2001.
- [47] R. Iverson and J. Vallance. New views of granular mass flow. *Geology*, 29(2):115–119, 2001.
- [48] R.M. Iverson. The physics of debris flows. *Reviews of Geophysics*, pages 245–296, 1997.
- [49] E.T. Jaynes. Information theory and statistical mechanics. *Statistical Physics III*, pages 181–218, 1963.
- [50] J.T. Jenkins. Particle segregation in collisional flows of inelastic spheres. In Herrmann, Hovi, and Luding, editors, *Physics of dry granular media*, NATO ASI series, pages 645–658. 1998.

- [51] J.T. Jenkins and S.B. Savage. A theory for the rapid flow of indential, smooth, nearly elastic, spherical particles. *JFM*, 130:187–202, 1983.
- [52] J.T. Jenkins and D.K. Yoon. Segregation in binary mixtures under gravity. *Phys. Rev. Lett.*, 88(19):1, 2002.
- [53] J.R. Johanson. Particle segregation... and what to do about it. *Chem. Eng.*, pages 183–188, 1978.
- [54] S. Keller, Y. Ito, and Nishimura K. Measurements of the vertical velocity distribution in ping pong ball avalanches. *Annal. Glac.*, 26:259–264, 1998.
- [55] A.G. Kulikovskii and M.E. Eglit. Two-dimensional problem of the motion of a snow avalanche along a slope with smoothly changing properties. *Prikladnaya Matematika i Mekhanika*, 37(5):837–848, 1973.
- [56] Silbert L.E., Ertas D., Grest G.S. and Haley T.C. Levine D., and Plimpton S.J. Granular flow down an inclined plane: Bagnold scaling and rheology. *Phys. Rev. E.*, 64(051302), 2001.
- [57] R.J. Leveque. *Finite Volume Methods for Hyperbolic Problems*. Cambridge texts in Applied Mathematics. Cambridge University Press, 2002.
- [58] M.Y. Louge. Model for dense granular flows down bumpy inclines. *Phys. Rev E*, 67(061303), 2003.
- [59] M.Y. Louge, J.T. Jenkins, A Reeves, and S. Keast. Microgravity segregation in collisional granular shearing flows. In A.D. Rosato and D.L. Blackmore, editors, *IUTAM Symposium on segregation in granular material*, pages 103–112. Kluwer.
- [60] F Mandl. *Statistical Physics*, volume A of *Manchester Physics Series*. Wiley, 1988.
- [61] G. Metcalfe, T. Shinbrot, J.J McCarthy, and J.M. Ottino. Avalanche mixing of granular solids. *Nature*, 374(2):39–41, 1995.

- [62] Middleton and Hampton. Subaqueous sediment transport and deposition by sediment gravity waves. In D.J. Stanley and D.J.P. Swift, editors, *Marine sediment transport and environmental management*, pages 197–218. Wiley, 1976.
- [63] L.W. Morland. Flow of viscous fluid through a porous deformable matrix. *Survey in Geophysics*, 1992.
- [64] T.Mullin. Coarsening of self-organised clusters in binary particle mixtures. *PRL*, 84:4741, 2000.
- [65] K Nagamine, R Cen, L Hernquist, J.P. Ostriker, and V Springel. Massive galaxies and extremely red objects at  $z = 1, 3$  in cosmological hydrodynamic simulations: Near-infrared properties. *Astrophysical journal*, 627(2):608–620, 2005.
- [66] Pouliquen. Scaling laws in granular flows down rough inclined planes. *Phys. Fluids*, 11(3):542–548, 1999.
- [67] O Pouliquen, J Delour, and S.B. Savage. Fingering in granular flows. *Letter to Nature*, 1997.
- [68] O Pouliquen and J.W. Vallance. Segregation induced instabilities of granular fronts. *Chaos*, pages 621–630, Sept 1999.
- [69] Brown R.L., Eden N.Q., and Barber M. Mixture theory of mass transfer based upon microstructure. *Defence Science Journal*, 49(5):393–409, Oct 1999.
- [70] S.B. Savage and K. Hutter. The motion of a finite mass of material down a rough incline. *JFM*, 199:177–215, 1989.
- [71] S.B. Savage and K Hutter. The dynamics of avalanches of antigranulocytees materials from initiation to runout .1. analysis. *Acta Mechanica*, 86:201–223, 1991.
- [72] S.B. Savage and C.K.K. Lun. Particle size segregation in inclined chute flow of dry cohesionless granular material. *JFM.*, 189:311–335, 1988.

- [73] M Shearer, J.M.N.T. Gray, and A.R. Thornton. Particle-size segregation and inverse-grading in granular avalanches. *to be Submitted*.
- [74] T. Shinbro, A. Alexander, and F.J. Muzzio. Spontaneous chaotic granular mixing. *Nature*, 397(6721):675–678, 1999.
- [75] H. Sigurdsson, S. Cashdollar, and S.R.J. Sparks. The eruption of vesuvius in a.d. 79: Reconstruction from historical and volcanological evidence. *American Journal of Archaeology*, 86(1):39–51, 1982.
- [76] John N. Staniforth. Determination and handling of total mixes in pharmaceutical systems. *Powder Technology*, 33(2):147–159, 1982.
- [77] J.J. Stoker. Water Waves : The Mathematical Theory with Applications, volume IV of Pure and Applied Mathematics : A series of texts and monographs. *Interscience Publishers, Inc., New York*, 1957.
- [78] P.K. Sweby. High resolution schemes using flux limiters for hyperbolic conservation laws. *SIAM Journal on Numerical Analysis*, 1984.
- [79] Y. Tai. Dynamics of Granular Avalanches and their Simulations with Shock-Capturing and Front-Tracking Numerical Schemes. *PhD thesis, Darmstadt*, 2000.
- [80] A. R. Thornton, J. M. N. T. Gray, and A Hogg. A three phase model of segregation in shallow granular free-surface flows. *JFM*. *Submitted*.
- [81] E.F. Toro. Riemann solvers and numerical methods for fluid dynamics. *Springer*, 1997.
- [82] G Toth and D Odstreil. Comparison of some flux corrected transport and total variation diminishing numerical schemes for hydrodynamic and magnetohydrodynamics problems. *Jour.of Comp. Phys.*, 1996.
- [83] J. Vallance. Lahars. *Encyclopedia of Volcanoes*, pages 601–616. *Academic press*, 2000.

- [84] *J. Vallance*. Experimental and Field Studies Related to the Behavior of Granular Mass Flows and the Characteristics of their Deposits. *PhD thesis, Michigan Technological University, 1994*.
- [85] *J. Vallance and S. B. Savage*. Particle segregation in granular flows down chutes. In *A.D. Rosato and D.L. Blackmore, editors, IUTAM Symposium on Segregation in Granular Flows. 2000*.
- [86] *B Van Leer*. Towards the ultimate conservative difference scheme v. J. Comput. Phys.
- [87] *L.B. Wang, X. Wang, L. Mohammad, and Wang Y.P.* Application of mixture theory in the evaluation of mechanical properties of asphalt concrete. *Journal of Materials in Civil Engineering, 16(2):167–174, April 2004*.
- [88] *Z.U.A. Warsi*. Fluid dynamics : theoretical and computational approaches. *CRC Press, 1993*.
- [89] *Watts and Masson*. New sonar evidence for recent catastrophic collapses of the north flank of tenerife, canary island. *Bull. Volcanol., 63:8–19, 2001*.
- [90] *H.C. Yee*. Construction of explicit and implicit symmetric tvd schemes and their applications. *J. Comp. Phys., 68:151–179, 1987*.
- [91] *H.C. Yee*. A class of high-resolution explicit and implicit shock-capturing methods. *Technical Report TM-101088, NASA, 1989*.
- [92] *O. Zik, Dov. Levine, S.G. Lipson, S Shtrikman, and J Stavans*. Rotationally induced segregation of granular materials. *Physical Review Letters, 73(5):644–647, 1994*.

# Appendix A

## Derivations and comment on Mohr-Coulomb type avalanche models

In this appendix, the two dimensional Savage-Hutter equations will be derived. These and the shallow water models, were discussed in §1.2. In §A.1, the Mohr-Coulomb analysis, which leads to the definition of the Earth-pressure coefficient, can be found. This Earth-pressure coefficient represents the only major difference between the two sets of avalanche models. In the shallow-water type models, the coefficient is taken to be unity, and in the Savage-Hutter models, it takes the values given by (A.3).

### A.1 Mohr-Coulomb yield criterion

It will be assumed that the granular material acts like an ideal Coulomb material, which means the rate of shear stress is proportional to the normal stress. This leads to the Coulomb yield criteria

$$S = N \tan \Phi, \tag{A.1}$$

where  $S$  is the shear stress,  $N$  is the normal stress, and  $\Phi$  is the angle of friction. Here  $\mu = \tan \Phi$ , where  $\mu$  is the coefficient of friction of the material. Defining  $\delta$  to be the basal angle of friction, it is clear straight away, that this is the angle at which

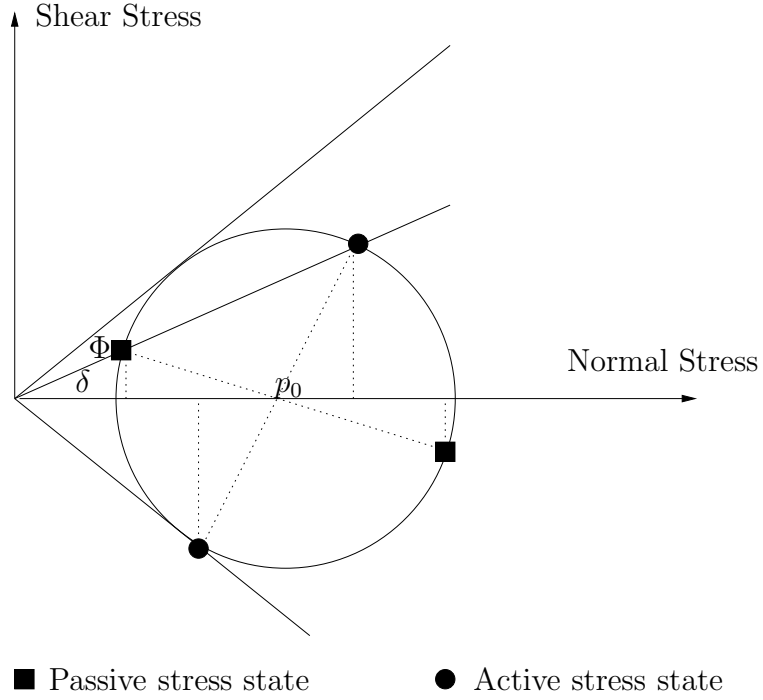


Figure A.1: Mohr diagram showing Coulomb yield criterion, bed friction angle, and active and passive stress conditions

a straight line would intersect the Mohr-Coulomb circle.

In a granular material, the top surface need not be horizontal. The angle of repose of the material is the maximum angle between the slope of the material and the horizontal. For a non-slipping material the angle of repose is equal to the internal angle of friction. From this, it is possible to relate the stresses normal and parallel to the chute, in the following way

$$p_{xx} = k_{act/pass} p_{zz}. \quad (\text{A.2})$$

These quantities are shown on a Mohr-Circler in figure A.1, from this diagram using geometrical arguments it can be shown that

$$k = \left. \begin{array}{l} k_{act} \quad \frac{\partial u}{\partial x} > 0 \\ k_{pass} \quad \frac{\partial u}{\partial x} \leq 0 \end{array} \right\} = 2 \sec^2 \Phi \left[ \mu \left( 1 \mp \cos^2 \Phi \sec^2 \delta \right)^{1/2} \right] - 1. \quad (\text{A.3})$$

The active stress state exists if the granular material is being accelerated (elongated), i.e.  $\partial u / \partial x \geq 0$ , and the passive state if  $\partial u / \partial x < 0$ .

## A.2 The two dimensional Savage-Hutter theory

In this section, the two-dimensional Savage-Hutter equations for granular flow will be derived. All the problems presented in this thesis will be two-dimensional. A full three-dimensional version of the theory can be found in [71]. It will be assumed that the continuum hypothesis holds. Balancing mass and momentum, the following is obtained

$$\nabla \cdot \mathbf{u} = \mathbf{0}, \quad (\text{A.4a})$$

$$\rho \frac{\partial \mathbf{u}}{\partial t} = -\nabla \cdot \mathbf{p} + \rho \mathbf{g}, \quad (\text{A.4b})$$

in which,  $\rho$  is the constant density,  $\mathbf{u}$  is the velocity,  $\mathbf{p}$  is the pressure tensor and  $\mathbf{g}$  is the gravitational acceleration of the material. The boundary condition at the free surface,  $F_s = z - h(x, t) \equiv 0$ , is

$$\left. \begin{aligned} \frac{\partial F_s}{\partial t} + \nabla F_s \cdot \mathbf{u} &= 0, \\ \mathbf{p} \cdot \mathbf{n} &= 0, \end{aligned} \right\} \text{ at } F_s(x, t) = 0. \quad (\text{A.5})$$

In (A.5),  $\mathbf{n}$  is a unit normal vector from the surface. The first of these conditions is a statement that  $F_s$  is a material surface, i.e. any material on the surface remains on the surface, and the second condition states that there is no stress normal to the free surface. At the base of the material  $F_b = z \equiv 0$ , hence,

$$\mathbf{u} \cdot \mathbf{n} = 0, \quad (\text{A.6})$$

applies. Here, it has been assumed that there is a solid flat boundary, located at  $z = 0$ , which will hold for all problems considered in this thesis. (A.6) is the statement of impermeability of the solid boundary.

Postulating a Coulomb-type friction law, the following relation applies for the shear stress

$$\mathbf{S} = -[\mathbf{n} \cdot \mathbf{p} - \mathbf{n} (\mathbf{n} \cdot \mathbf{p} \cdot \mathbf{n})]. \quad (\text{A.7})$$

The normal stress,  $\mathbf{N}$ , is related to  $\mathbf{S}$  as follows,

$$\mathbf{S} = -\text{sgn}(\mathbf{u}) \mathbf{N} \tan \Phi, \quad (\text{A.8})$$

where  $\text{sgn}(\mathbf{u}) = \mathbf{u}/|\mathbf{u}|$  and  $\Phi$  is the angle of friction. Clearly, at the base of the material  $\Phi = \delta$ , where  $\delta$  is the dynamic angle of friction of the granular material. Using (3.5), (3.4) and (3.3) together, the following boundary condition is produced

$$\mathbf{n} \cdot \mathbf{p} - \mathbf{n} (\mathbf{n} \cdot \mathbf{p} \cdot \mathbf{n}) = -\text{sgn}(\mathbf{u}) (\mathbf{n} \cdot \mathbf{p} \cdot \mathbf{n}) \tan \delta \quad \text{at } z = 0. \quad (\text{A.9})$$

Imposing the discussed coordinate system, see figure 2.1, on (A.4) yields

$$\frac{\partial u}{\partial x} + \frac{\partial w}{\partial z} = 0, \quad (\text{A.10a})$$

$$\rho \left\{ \frac{\partial u}{\partial t} + u \frac{\partial u}{\partial x} + w \frac{\partial u}{\partial z} \right\} = \rho g \sin \xi - \frac{\partial p_{xx}}{\partial x} - \frac{\partial p_{xz}}{\partial z}, \quad (\text{A.10b})$$

$$\rho \left\{ \frac{\partial w}{\partial t} + u \frac{\partial w}{\partial x} + w \frac{\partial w}{\partial z} \right\} = -\rho g \cos \xi - \frac{\partial p_{xx}}{\partial x} - \frac{\partial p_{zz}}{\partial z}. \quad (\text{A.10c})$$

Before proceeding it is helpful to non-dimensionalise the equations, to this end introduce the normal avalanche scaling

$$\begin{aligned} x &= L\tilde{x}, & z &= H\tilde{z}, \\ (u, v) &= \sqrt{gL}(\tilde{u}, \tilde{v}), & w &= (H\sqrt{gL}/L)\tilde{w}, & t &= (L/\sqrt{gL})\tilde{t}, \\ p_{xx} &= (\rho g \cos \xi H)\tilde{p}_{xx}, & p_{zz} &= (\rho g \cos \xi H)\tilde{p}_{zz}, & p_{xz} &= (\rho g \sin \xi H)\tilde{p}_{xz} \end{aligned} \quad (\text{A.11})$$

Here  $\tilde{\cdot}$  indicates a dimensionless variable, and inserting this into (A.10) gives the following non-dimensional version

$$\frac{\partial u}{\partial x} + \frac{\partial w}{\partial z} = 0, \quad (\text{A.12a})$$

$$\frac{\partial u}{\partial t} + u \frac{\partial u}{\partial x} + w \frac{\partial u}{\partial z} = \sin \xi \left( 1 - \frac{\partial p_{xz}}{\partial z} \right) - \epsilon \cos \xi \frac{\partial p_{xx}}{\partial x}, \quad (\text{A.12b})$$

$$\epsilon \left\{ \frac{\partial w}{\partial t} + u \frac{\partial w}{\partial x} + w \frac{\partial w}{\partial z} \right\} = -\cos \xi \left( 1 - \frac{\partial p_{xx}}{\partial z} \right) - \epsilon \sin \xi \frac{\partial p_{xz}}{\partial x}, \quad (\text{A.12c})$$

with  $\epsilon = H/L$ . In the shallow depth limit, (A.12c) reduces to

$$1 = \frac{\partial p_{zz}}{\partial z}, \quad (\text{A.13})$$

which is easily integrated to give

$$p_{zz} = h - z. \quad (\text{A.14})$$

Here, use of the boundary condition (A.5) has been made. This same simplification cannot be made to the x-momentum equation, since the resulting equations are too simple to model avalanche motions correctly. This pressure field is compatible with the pressure in the segregation model (see (2.11)), which means it will be possible, at a later date, to couple the two models together.

Adding  $u$ , multiplying (A.12a) by (A.12b), and then integrating w.r.t to  $z$  from 0 to  $h$ , produces

$$\int_{z=0}^h \left\{ \frac{\partial u}{\partial t} + 2u \frac{\partial u}{\partial x} + u \frac{\partial w}{\partial z} + w \frac{\partial u}{\partial z} \right\} dz = \epsilon \cos \xi \int_{z=0}^h \frac{\partial p_{xx}}{\partial x} dz - \sin \xi \left\{ [p_{xz}]_{z=0}^h + h \right\}. \quad (\text{A.15})$$

Clearly, the left hand side can be simplified to give the following form of (A.15),

$$\int_{z=0}^h \left\{ \frac{\partial u}{\partial t} + \frac{\partial u^2}{\partial x} \right\} dz + [uw]_{z=0}^h = \epsilon \cos \xi \int_{z=0}^h \frac{\partial p_{xx}}{\partial x} dz - \sin \xi \left\{ [p_{xz}]_{z=0}^h + h \right\}. \quad (\text{A.16})$$

Using Leibniz's rule to move the derivatives out of the integrands and remembering  $h = h(x, t)$ , reveals

$$\left\{ \frac{\partial}{\partial t} \int_{z=0}^h u \, dy + \frac{\partial}{\partial x} \int_{z=0}^h u^2 \, dy - \left[ u \left( \frac{\partial h}{\partial t} + u \frac{\partial h}{\partial x} - w \right) \right]_{z=h} - [uw]_{z=0} \right\} = \sin \xi \left( h - [p_{xz}]_{z=0}^h \right) - \epsilon \cos \xi \left\{ \frac{\partial}{\partial x} \int_{z=0}^h p_{xx} \, dy - \left[ p_{xx} \frac{\partial h}{\partial x} \right]_{z=h} \right\}. \quad (\text{A.17})$$

Writing the boundary conditions, (A.5) and (A.6), in terms of the coordinate system being used here, and non-dimensionalising, subject to the scaling (A.11), gives

$$\frac{\partial h}{\partial t} + u \frac{\partial h}{\partial x} - w = 0 \quad \text{at} \quad z = h(x, t), \quad (\text{A.18a})$$

$$w = 0 \quad \text{at} \quad z = 0. \quad (\text{A.18b})$$

Substituting this result into (A.17) produces

$$\left\{ \frac{\partial}{\partial t} \int_{z=0}^h u \, dz + \frac{\partial}{\partial x} \int_{z=0}^h u^2 \, dz \right\} = \sin \xi \left( h - [p_{xz}]_{z=0}^h \right) - \epsilon \cos \xi \left\{ \frac{\partial}{\partial x} \int_{z=0}^h p_{xx} \, dz - \left[ p_{xx} \frac{\partial h}{\partial x} \right]_{z=h} \right\}. \quad (\text{A.19})$$

Writing the stress condition, (A.5), in terms of the non-dimensional coordinates gives

$$\left. \begin{aligned} -\epsilon \cos \xi p_{xx} \frac{\partial h}{\partial x} + \sin \xi p_{xz} &= 0, \\ -\epsilon \sin \xi p_{xz} \frac{\partial h}{\partial x} + \cos \xi p_{xz} &= 0. \end{aligned} \right\} \quad \text{at} \quad z = h(x, t). \quad (\text{A.20})$$

Equating terms of order 1 implies  $p_{xz} = p_{zz} = 0$ , hence now (A.2) implies  $p_{xx} = 0$ .

So now (A.19) becomes

$$\left\{ \frac{\partial}{\partial t} \int_{z=0}^h u \, dz + \frac{\partial}{\partial x} \int_{z=0}^h u^2 \, dz \right\} = \sin \xi \left( h - [p_{xz}]_{z=0}^h \right) - \epsilon \cos \xi \left\{ \frac{\partial}{\partial x} \int_{z=0}^h p_{xx} \, dz \right\}. \quad (\text{A.21})$$

Now define the transverse averages in the following way

$$\bar{u}h = \int_{z=0}^h u \, dz \quad , \quad hp_{xx}^- = \int_{z=0}^h p_{xx} \, dz \quad , \quad \bar{u}^2h = \int_{z=0}^h u^2 \, dz = \alpha_1 \bar{u}h. \quad (\text{A.22})$$

Obviously,  $\alpha_1$  would be 1 if the velocity profile was uniform, therefore, it can be considered as a measure of the deviation of the profile from a linear state. It is worth noting that, for a parabolic velocity profile (with zero basal velocity),  $\alpha_1$  turns out to be  $6/5$ , therefore,  $\alpha = 1$  may be a significant approximation. Under this assumption, and using the transverse averages, (A.21) becomes

$$\frac{\partial}{\partial t} (h\bar{u}) + \frac{\partial}{\partial x} (h\bar{u}^2) + \epsilon \cos \xi \frac{\partial}{\partial x} (hp_{xx}^-) = \sin \xi h + \sin \xi [p_{xz}^-]_{z=0}. \quad (\text{A.23})$$

Using the shallowness assumption, (A.9) can be written as

$$p_{xz}|_{z=0} = -\text{sgn}(\mathbf{u})p_{zz} \tan \delta \cot \xi + O(\epsilon) \quad (\text{A.24})$$

and using (A.2) again gives

$$\frac{\partial}{\partial t} (h\bar{u}) + \frac{\partial}{\partial x} (h\bar{u}^2) + \epsilon k \cos \xi \frac{\partial}{\partial x} (hp_{xx}^-) = \sin \xi h - \text{sgn}(\mathbf{u}) \cos \xi \tan \delta p_{zz}^-|_{z=0}. \quad (\text{A.25})$$

Integrating (A.12a) from 0 to  $h$ , and using the kinematics boundary condition, gives

$$\frac{\partial h}{\partial t} + \frac{\partial}{\partial x} (hu) = 0. \quad (\text{A.26})$$

Writing back in terms of the dimensional variables gives

$$\frac{\partial h}{\partial t} + \frac{\partial}{\partial x} (hu) = 0, \quad (\text{A.27a})$$

$$\frac{\partial}{\partial t} (hu) + \frac{\partial}{\partial x} (hu^2) + \frac{\partial}{\partial x} \left( \frac{kg \cos \xi h^2}{2} \right) = hgD, \quad (\text{A.27b})$$

where  $D$  is the driving force and is given by

$$D = \cos \xi (\tan \xi - \text{sgn}(\mathbf{u}) \tan \delta). \quad (\text{A.28})$$

# Appendix B

## Exact Form of the function $K_s(\eta)$

In this section, the full form of the function  $K_s$  is discussed, when it is expressed in physical variables.  $K_s$  is the function which in the Savage & Lun theory relates the small particles percolation velocities to their volume fraction and other physical quantities. From the method of characteristics, it follows that

$$K_s = \frac{\gamma \frac{\partial}{\partial \eta} (-\rho_s q_{N_s})}{\left(\frac{\partial \rho_s}{\partial \eta}\right)}. \quad (\text{B.1})$$

The full expression is obtained simply by substituting expressions for  $q_{N_s}$  and  $\rho_s$  into this formula, (B.1). The algebra is lengthy and tedious, as most of the terms depend on  $\eta$  in some way. The final form will be expressed in terms of physical quantities. With this in mind, it is convenient to make the following definitions; let  $\sigma = D_s/D_l$ , as before, be the ratio of the diameters of the small to large particles,  $M$  be the total number of voids,  $N$  be the total number of particles,  $k_{AV}$ , be the ratio of the largest sphere that will fit into a void to the actual area of the void and,  $k_{LT}$ , a dimensionless measure of the average particle diameter to average layer thickness. After some work, the following result is obtained

$$K_s(\eta) = \frac{4}{\pi} \frac{M}{N} \gamma k_{LT}^2 \frac{\partial II}{\partial \eta} / \frac{\partial I}{\partial \eta}, \quad (\text{B.2})$$

where

$$I = \frac{A_7}{A_6}, \quad (\text{B.3a})$$

$$II = \frac{[A_2 \exp(A_3) - A_4 \exp(A_5)]}{A_1 A_6^2}. \quad (\text{B.3b})$$

and

$$A_1 = \frac{(1 + \eta\sigma)^2 (1 + \eta\sigma^3)}{(1 + \eta)\eta}, \quad (\text{B.4a})$$

$$A_2 = \bar{E} - E_m + 1 \frac{(1 + \eta)\sigma}{1 + \eta\sigma}, \quad (\text{B.4b})$$

$$A_3 = -\frac{[(1 + \eta)\sigma / (1 + \eta\sigma)] - E_m}{\bar{E} - E_m}, \quad (\text{B.4c})$$

$$A_4 = \bar{E} - E_m + 1 + \frac{1 + \eta}{1 + \eta\sigma}, \quad (\text{B.4d})$$

$$A_5 = -\frac{[(1 + \eta) / (1 + \eta\sigma)] - E_m}{\bar{E} - E_m}, \quad (\text{B.4e})$$

$$A_6 = \frac{(1 + \eta)(1 + \eta\sigma^2)}{(1 + \eta\sigma)^2} + \frac{\bar{E}}{k_{AV}} + \frac{M}{N}, \quad (\text{B.4f})$$

$$A_7 = \frac{(1 + \eta)^2 \eta}{(1 + \eta\sigma)^3}. \quad (\text{B.4g})$$

## B.1 Limit as $\eta \rightarrow 0$

In the dilute limit of  $\eta \rightarrow 0$ , it can be shown that the function  $K_s$  takes the simplified form of

$$K_s = -\frac{-q_{N_s}}{D_l (du/dz)}, \quad (\text{B.5})$$

which is just a dimensionless net percolation of small particles. Expanding this in terms of physical variables gives

$$K_s = -\frac{4M}{\pi N} \frac{k_{LT}^2}{1 + (\bar{E}^2/k_{AV}) (M/N)} \left( (2 + \bar{E} - E_m) \exp \left[ -\frac{1 - E_m}{E - E_m} \right] - (\sigma \bar{E} - E_m + 1) \exp \left[ -\frac{\sigma - E_m}{E - E_m} \right] \right). \quad (\text{B.6})$$

From this form, it is clear this is a constant and only depends on the physical properties of the particles and the flow.

# Appendix C

## A time dependent analytic solution with shear

In this section, the problem of the flow of homogeneous material, with volume fraction  $\phi_0$ , into a chute filled with small particles, will be considered. The steady-state version of this problem can be found in §3, and a time-dependent analytical solution for the  $\alpha = 1$  case is derived in §3.3.3. This material can be found in [35], along with a selection of other time-dependent solution with  $\alpha \neq 1$ .

### C.1 Review of the non-time-dependent case

Before getting involved in the details of the time-dependent problem, it is instructive to review the steady-state case for this setup. As derived a few times before, the generalised shock relation can be written as

$$u \frac{ds}{dx} = S_r (\phi^+ + \phi^- - 1), \quad (\text{C.1})$$

where  $s = s(z)$  is the height of the shock. It will be Assumed the velocity field has the following form

$$u = \alpha + 2(1 - \alpha)z. \quad (\text{C.2})$$

This form is chosen because it will give the same volume flux for all values of  $\alpha$ , therefore,  $\alpha$  is just a non-dimensional measure of the shearing rate.  $\alpha = 1$  corresponds

to plug flow and  $\alpha = 0$  corresponds to pure linear shear.

Integrating (C.1) gives

$$\alpha z + (1 - \alpha) z^2 = S_r (\phi^+ + \phi^- - 1) x + C. \quad (\text{C.3})$$

The inflow condition, which will be applied at  $x = 0$ , is  $\phi = \phi_0$  for all  $z$ .

### C.1.1 Top Shock Propagation

For the top shock the conditions  $\phi^+ = 0$  and  $\phi^- = \phi_0$ , must hold, and it is generated from the point  $x = 0$  and  $z = 1$ . This implies the constant is  $C = 1$ , and this shock is given by the equation,

$$z = \begin{cases} \frac{-\alpha + \sqrt{\alpha^2 + 4(1 - S_r(1 - \phi_0)x)(1 - \alpha)}}{2(1 - \alpha)} & : \alpha \neq 1 \\ 1 - S_r(1 - \phi_0)x & : \alpha = 1 \end{cases} \quad (\text{C.4})$$

The positive branch is taken as it exists within the domain under consideration.

### C.1.2 Bottom Shock Propagation

Whereas, for the bottom shock  $\phi^+ = \phi_0$  and  $\phi^- = 1$ . This shock originates from the point  $x = 0$  and  $z = 0$ , which implies that  $C = 0$  and the second shock is given by

$$z = \begin{cases} \frac{-\alpha + \sqrt{\alpha^2 + 4S_r\phi_0x(1 - \alpha)}}{2(1 - \alpha)} & \alpha \neq 1 \\ z = S_r\phi_0x & \alpha = 1 \end{cases} \quad (\text{C.5})$$

### C.1.3 Full Segregation Point

When these two shocks intersect, a third (segregation) shock will be formed. Its location is given by

$$x = \frac{1}{S_r}, \quad (\text{C.6a})$$

$$z = \begin{cases} \frac{-\alpha + \sqrt{\alpha^2 + 4\phi_0(1 - \alpha)}}{2(1 - \alpha)} & \alpha \neq 1 \\ \phi_0 & \alpha = 1 \end{cases}. \quad (\text{C.6b})$$

## C.2 Time Dependent Case

The fully time-dependent version of this problem will now be considered. Hence, the solution to the following equation

$$\phi_t + (\phi u)_x - S_r (\phi (1 - \phi))_z = 0, \quad (\text{C.7})$$

will be sought. The same steps as the time-independent case will be taken, hence, firstly, a shock relation needs to be obtained. The same structure, as the steady-state case is anticipated; this is predicted to be one shock generated from the top and one from the bottom and a final third segregation shock.

### C.2.1 Deriving the Shock Relation

In this case, it will be convenient to integrate (C.7) w.r.t.  $x$ , and to assume that  $u = u(z)$  only, giving

$$\frac{\partial}{\partial t} \int_{L_2}^{L_1} \phi \, dx + [\phi u]_{L_1}^{L_2} - \frac{\partial}{\partial z} \int_{L_1}^{L_2} S_r \phi (1 - \phi) \, dx = 0. \quad (\text{C.8})$$

Assuming there is a jump (shock) located at  $x = \hat{X}(z, t)$ , from  $\phi^+$  to  $\phi^-$ , (C.8) becomes

$$\begin{aligned} & \frac{\partial}{\partial t} \left[ \int_{L_1}^{\hat{X}} \phi \, dx + \int_{\hat{X}}^{L_2} \phi \, dx \right] + [\phi u]_{L_1}^{L_2}, \\ & - \frac{\partial}{\partial z} \left[ \int_{L_1}^{\hat{X}} (\phi (1 - \phi)) \, dx + \int_{\hat{X}}^{L_2} (\phi (1 - \phi)) \, dx \right] = 0. \end{aligned} \quad (\text{C.9})$$

Applying Leibniz's rule to this problem, reveals

$$\int_{L_1}^{L_2} \frac{\partial \phi}{\partial t} \, dx - [\phi]_-^+ \hat{X}_t + [\phi u]_{L_1}^{L_2} - \int_{L_1}^{L_2} \frac{\partial}{\partial z} (\phi (1 - \phi)) \, dx + [S_r \phi (1 - \phi)]_-^+ \hat{X}_z \quad (\text{C.10})$$

Letting  $L_1 \rightarrow L_2$  produces the following result, for the shock development

$$[\phi]_-^+ (u - \hat{X}_t) + S_r [\phi (1 - \phi)]_-^+ \hat{X}_z = 0, \quad (\text{C.11})$$

which when rearranged, in a more useful form, states

$$u(z) = \hat{X}_t - \frac{S_r [\phi (1 - \phi)]_-^+ \hat{X}_z}{[\phi]_-^+}. \quad (\text{C.12})$$

This, clearly, reduces back to the steady-state condition (C.1) if it is assumed  $\hat{X}$  is independent of time. The solution to (C.12) represents planes in  $x$  and  $t$ , which describes the full temporal and spatial development of shocks. Now that the shock relation has been determined, attention will be given to establishing the development of the shock generated at the top boundary.

### C.2.2 Top Boundary

To generate characteristics that propagate into the domain, it has to be assumed that the shock generated from the top boundary is independent of time. Additionally, this is clearly the case in the numerical simulations that have been performed. So, the conditions to be applied on the top boundary are

$$\phi^+ = 0, \quad \phi^- = \phi_0, \quad \hat{X} \neq \text{fn}(x), \quad (\text{C.13})$$

with the obvious boundary condition  $x = 0$  when  $z = 0$ .

From now on, for notation convenience, in the following analysis  $x$  will be used as a short-hand for  $\hat{X}$ . Substituting these results into (C.12), and recalling (C.2), then

$$-S_r(1 - \phi_0) \frac{dx}{dz} = \alpha + 2(1 - \alpha)z, \quad (\text{C.14})$$

is obtained. Integrating up this expression and applying the boundary condition gives

$$x = \frac{1 - \alpha z - (1 - \alpha)z^2}{S_r(1 - \phi_0)}, \quad (\text{C.15})$$

which is exactly the same expression as the steady-state top shock.

### C.2.3 Bottom Boundary

The bottom boundary shock is considerably more complicated, as it is fully time-dependent. On the bottom boundary  $\phi^+ = \phi_0$ ,  $\phi^- = 1$ , with the boundary/initial conditions

$$x(0, t) = 0, \quad x(z, 0) = 0. \quad (\text{C.16})$$

Under conditions (C.16), equation (C.12) reduces down to

$$x_t + S_r \phi_0 x_z = U(z). \quad (\text{C.17})$$

This equation will be solved via the method of characteristics, see §3.1.1 for details.

### Solution Via Method of Characteristics

Since the shock location  $x$  is a function of both  $z, t$  from §3.1.1 the following equation must hold

$$\frac{dx}{dr} = \frac{dt}{dr} \frac{\partial x}{\partial t} + \frac{dz}{dr} \frac{\partial x}{\partial z}, \quad (\text{C.18})$$

where  $r$  is a characteristic coordinate. From direct comparison with (C.17), the following is quite clear

$$\frac{dt}{dr} = 1 \quad , \quad \frac{dz}{dr} = S_r \phi_0. \quad (\text{C.19})$$

Hence, it follows that  $t = r + A$ , where  $A$  is a constant, and

$$\lambda = S_r \phi_0 t - z. \quad (\text{C.20})$$

Substituting these results into the shock relation, (C.17), reveals the expression

$$\frac{dx}{dt} = u(z) = u(S_r \phi_0 t - \lambda). \quad (\text{C.21})$$

Recalling (C.2), this equation can be expressed in the more useful form of

$$\frac{dx}{dt} = \alpha + 2(1 - \alpha) [S_r \phi_0 t - \lambda] \quad (\text{C.22})$$

Integrating up, and substituting back in for  $\lambda$ , reveals the result

$$x = \alpha t - S_r \phi_0 (1 - \alpha) t^2 + 2(1 - \alpha) t z + h(\lambda). \quad (\text{C.23})$$

This is the general form of the bottom shock but to determine  $h(\lambda)$  the initial and boundary conditions must be applied.

### Initial Conditions on the Shock

The initial condition states that  $x(z, 0) = 0$ , which implies  $h = 0$ . Now, this is true when  $\lambda = -z$ . Since  $z$  runs from 0 to 1, then,

$$h = 0 \quad -1 \leq \lambda < 0. \quad (\text{C.24})$$

One interpretation of this result is that when  $-1 \leq \lambda < 0$ , the bottom shock is controlled by the initial conditions.

### Boundary Condition on the Shock

The boundary condition states that  $x(0, t) = 0$ , implying  $\lambda = S_r \phi_0 t$ , then since the problem is defined for  $t \geq 0$ , this means this condition applies for all positive  $\lambda$ . This defines the values of  $\lambda$  for which the lower shock is controlled by the boundary conditions.

Substituting these results into (C.23), gives

$$h(S_r \phi_0 t) = -\alpha t + S_r \phi_0 (1 - \alpha) t^2, \quad (\text{C.25})$$

and it will be convenient to define  $\zeta = S_r \phi_0 t$ . After some simple rearrangement, the following can be shown

$$h(\xi) = \frac{1}{S_r \phi_0} [-\alpha \xi + (1 - \alpha) \xi^2] \quad (\text{C.26})$$

A note on this section. Here  $h$  is an unknown function, therefore, it is convenient, and it may be necessary, to write the definition and description in terms of the same variables, e.g. you would not write  $f(x) = u^2$  and then note the relationship between  $u$  and  $x$  somewhere else.

Once this function has been found for this ‘boundary condition’, it will be known for all values of  $\lambda$ . So far, the value  $h$ , for the case when  $\lambda = \xi$ , has been found, but this function is now fixed for all values of  $\lambda$ . So this function can be substituted back into (C.23), with the use of the definition of  $\lambda$  gives

$$x = \alpha t - S_r \phi_0 (1 - \alpha t^2) + 2(1 - \alpha) t z + \frac{1}{S_r \phi_0} [-\alpha [S_r \phi_0 t - z] + (1 - \alpha) [S_r \phi_0 t - z]^2], \quad (\text{C.27})$$

which can be simplified down to

$$x = \frac{\alpha z + (1 - \alpha) z^2}{S_r \phi_0}. \quad (\text{C.28})$$

This is exactly the steady-state form of the bottom shock, which was derived previously, but it is additionally known to only be valid for  $\lambda \geq 0$  or in terms of physical variables

$$t \geq \frac{z}{S_r \phi_0} \quad (\text{C.29})$$

It is a simple matter to confirm that the solutions agree at the point  $\lambda = 1$ . Recall that, the initial condition controlling time-dependent part of the shock had a lower limit. It can be shown that, this condition is weaker than  $t \geq 0$ , therefore, it is always satisfied, since this whole problem is only defined for positive time.

### Summary

In summary, the bottom shock is given by

$$x = \begin{cases} \alpha t - S_r \phi_0 (1 - \alpha) t^2 + 2(1 - \alpha) t z & 0 \leq t \leq \frac{z}{S_r \phi_0}, \quad (\text{a}) \\ \frac{\alpha z + (1 - \alpha) z^2}{S_r \phi_0} & t \geq \frac{z}{S_r \phi_0}. \quad (\text{b}) \end{cases} \quad (\text{C.30})$$

The point, where the steady state part of the shock meets the time-dependent part, is controlled by

$$x_t = \alpha t + S_r \phi_0 (1 - \alpha) t^2, \quad (\text{C.31a})$$

$$z = S_r \phi_0 t. \quad (\text{C.31b})$$

This point will be referred to as the transition point of the lower shock, as it represents the location behind which the shock has achieved its steady-state configuration.

### C.2.4 Triple Point

In general, the top and bottom shocks will meet at a point. Here, they will form a third segregation shock, hence, this is a triple point of the flow. Initially, the triple point will be a function of time and will be defined by the intersection of (C.30)(a) with (C.15). Hence, the solution is given by the root of the following quadratic,

$$(1 - \alpha) z^2 + [\alpha + 2S_r t(1 - \phi_0)(1 - \alpha)] z + S_r(1 - \phi_0) [\alpha t - S_r \phi_0 (1 - \alpha) t^2] - 1 = 0. \quad (\text{C.32})$$

This shock becomes steady at the point where the steady bottom shock, (C.30)(b), intersects the top shock, (C.15). This could be viewed in an alternative way, i.e. where the transition point of the bottom shock and the triple point are one and the same. It is left to show that this steady triple point solution is given by

$$z = \frac{-\alpha + \sqrt{\alpha^2 + 4\phi_0(1 - \alpha)}}{2(1 - \alpha)}, \quad (\text{C.33a})$$

$$x = \frac{1}{S_r}. \quad (\text{C.33b})$$

The easiest way to calculate the time at which the triple point becomes steady is to equate (C.31b) with the  $z$  location of the steady triple point, this implies

$$t = \frac{-\alpha + \sqrt{\alpha^2 + 4(1-\alpha)\phi_0}}{2(1-\alpha)S_r\phi_0}. \quad (\text{C.34})$$

This can be simplified to the following result

$$t = \frac{2\sqrt{\phi_0}}{2S_r\phi_0} 2S_r\phi_0 = \frac{1}{S_r\sqrt{\phi_0}}. \quad (\text{C.35})$$

### C.2.5 The Final Shock

All that remains to do, to complete the solution, is to calculate what happens to the third shock which emanates from this triple point. Hence this shock is subject to the boundary condition that it starts from the point  $(x_{\text{trip}}, z_{\text{trip}})$ . The chute is considered to be filled initially with small particles, which imposes the condition that  $x = 0, z = 1$  at  $t = 0$ .

Before the triple point becomes steady, the starting point will be time-dependent. This, final shock, is a segregation shock separating large from small material, hence, for the third shock  $\phi^+ = 0$  and  $\phi^- = 1$ . Inserting this information into (C.12), reveals that this shock's development is governed by the following o.d.e.

$$x_t = u(z), \quad (\text{C.36})$$

which is easily integrated up to give

$$x = u(z)t + f(z). \quad (\text{C.37})$$

The initial condition leads to the result  $f(1) = 0$ . Applying the boundary condition gives,

$$x_{\text{trip}} = u(z_{\text{trip}})t + f(z_{\text{trip}}). \quad (\text{C.38})$$

By numerically solving the quadratic, (C.33), it is possible to express  $x_{\text{trip}}$  and  $z_{\text{trip}}$  in terms of  $z$  and  $t$  and, hence, plot the solution. It should be noted that, this would give the time-dependent part of the final shock, after the transition point has reached

the triple point a steady section of this shock is produced. The expression for this section of solution is simply obtained from (C.33) and (C.35), hence completing the full structure of the solution.